AN EXPERIMENTAL MODEL OF HUMAN AORTIC DISSECTION

by

Martin S. Schlicht Jr.

A dissertation submitted in partial fulfillment
of the requirements for the degree of
Doctor of Philosophy
(Biomedical Engineering)
in The University of Michigan
2011

Doctoral Committee:

Professor Ramon Berguer, Co-Chair
Associate Professor Joseph L. Bull, Co-Chair
Professor Gilbert R. Upchurch Jr.
Assistant Research Scientist Khalil M. Khanafer

This is dedicated to my sister-in-law Jill, the youngest sister of my wife Cindy. She was like the daughter I never had, especially after we lost their father to cancer in 1993 and then their mother to cancer as well in 2000. She was always very supportive and encouraged me throughout my studies. She would keep me company nearly daily, talking on our cell phones as I commuted the seventy mile trip to Ann Arbor and then back home again. She was looking forward to the day I graduated and I know she is still by my side even though she lost her battle with cancer in December 2006.

ACKNOWLEDGMENTS

I would like to thank my committee, Frankel Professor Ramon Berguer, Associate Professor Joseph L. Bull, Professor Gilbert R. Upchurch Jr. and Assistant Research Scientist Khalil M. Khanafer, for taking time from their busy and demanding careers to guide me in my graduate studies. I would especially like to express my sincere gratitude to Dr. Ramon Berguer, my advisor and mentor. It was an honor to conduct my studies under such a renowned surgeon. His straight-forward approach and passion for research made my time here exciting and seem almost effortless.

I will miss my friends and co-workers from the Biotransport lab (past & present: Ambroise Duprey, Zheng Zheng Wong, Yu-chun Lin, James Stephen, Harm Nieuwstadt, Andres Calderon, Balaji Srinivasan, Brijesh Eshpuniyani, Tom Tsai, Doug Valassis, Stan Samuel, Adnan Qamar, David Li, Robinson Seda, Rob Dodde). I am grateful for the support and help they provided me. Special thanks go to Ambroise Duprey for all the work he did with me during his year-long fellowship. His passion for engineering and dedication advanced my studies significantly. Thank you to Tom Tsai and Doug Valassis for all their work on the chronic bench-top model. Thank you to Adnan Qamar who helped a great deal with computer modeling and was always willing to discuss theory and lend me a hand in the lab. Thank you to Zheng Zheng Wong for all his help and discussions on theory and experimental modeling even after returning home to Singapore. And finally to Rob Dodde for his help with Labview and electronics.

The staff here at the University of Michigan are the ones behind the scene that help us graduate students accomplish our work with all of our energy directed toward our research. In the BME department Tonya Thompson became not only a close friend but, the one I relied on for all of my supplies ordering. Chuck Nicholas, Brandon Baier and formerly Dan McHugh are the IT specialists that kept our computers up and running and provided a great deal of support for the technology in the BME department. Thank you to Maria Steele and Susan Bitzer the graduate and undergraduate student advisors. I would also like to thank Kim Savage, Sandy Martin and Thomas Draper, the staff members in the Cardiovascular Center for all their assistance and for keeping me connected to Dr. Berguer and his schedule.

I owe a great deal to a number of people that provided me with technical support. Steve Emanuel, formerly with the Graduate Student Machine Shop, not only taught me how to use the machines there but, would stay open all hours of the night to accommodate me when needed. Steve has become a great friend and still continues to support me with advice and machining after moving to another University. Kent Pruss in the Auto Lay Machine Shop for all the machining he has done for me once my schedule became too hectic for me to be in the shop. I would like to thank Harald Eberhart, Master glassblower, for his expertise in creating the glass fittings, imaging boxes and a number of other devices that were pivotal in my research. Also, Nichole Baker for her work in ultrasound imaging of my bench-top models. And especially Dave Brant from the ECMO Lab who provided me with a great deal of help setting up my bench-top flow loop when I first started here.

Most of all I would like to thank my family and especially my wife Cindy, who is the one that encouraged me to go back to school and supported my changing careers. It is with their support and sacrifices that I was able to pursue my degree. They always encouraged me and understood when my studies kept me from spending time with them. My biggest regret was not finishing before my father passed in July, 2010 so he could see me graduate.

TABLE OF CONTENTS

LIST OF TABLES

LIST OF FIGURES

LIST OF APPENDICES

ABSTRACT

AN EXPERIMENTAL MODEL OF HUMAN AORTIC DISSECTION

by

Martin S. Schlicht Jr.

Co-Chairs: Ramon Berguer and Joseph L. Bull

Vascular diseases such as aortic dissections, aneurysms and stenosis are becoming frequent disorders in the industrialized world, and aortic diseases constitute an emerging share of these. An acute aortic dissection of the ascending aorta has an increasing mortality rate of 1% to 2% per hour after symptom onset. Determining whether an aortic dissection is at risk for rupture is not straightforward, and a better understanding of the role of thrombus, vessel geometry and wall components, entry tears, and other features of the diseased aorta is needed.

The focus of this dissertation is to build an experimental bench top model of an aortic dissection which provides a fundamental knowledge of the flow characteristics and flap behavior under various physiological conditions. This model may help to emulate the forces and appearance of a dissection and explain the flow/pressure events that affect the stability or progression of a dissection. The operation of such a model will permit ranking the variables that determine the evolution of a dissection towards aneurysm or rupture. The mechanical properties of the polydimethylsiloxane (PDMS) material used to create experimental models of aortic dissections were investigated in the range of physiological parameters. This research may also be used as a benchmark to validate numerical models of aortic dissection. It also paves the road for researchers in the area of imaging to determine the elastic modulus of a living *in-vivo* arterial wall based on dynamic DICOM files in a non-invasive manner using high resolution CT scans.

Chapter 1

Introduction

1.1 Aortic Dissection: Background and Significance

Cardiovascular diseases are currently and are projected to remain the single leading cause of death globally through 2030 [1]. Aortic dissection, one of the most catastrophic diseases that can affect the aorta, is a tear in the inner layer of the aortic wall that allows blood under physiological pressure to insinuate itself within the layers of the aortic wall forcing them apart. In this research, we focus on type B dissections (See Figure 4.1A) that start at the level of the left subclavian and extend distally into the descending thoracic aorta. Following an intimal tear at the level of the left subclavian artery the dissection may extend proximally (towards the heart), distally (away from the heart) or both directions. The flow of blood within the wall creates a false lumen that is separated from the true lumen by the intimal flap. One or several additional entry tears, distal to the primary tear, may be present. Aortic dissection occurs with a frequency of 2.6-3.5 per 100,000 person-years [2-4]. Acute aortic dissection is highly lethal, with a mortality rate that increases 1% to 2% per hour after symptom onset [5], the patient may die before treatment is begun or may reach the operating room in dire condition.

The acute phase in an aortic dissection extends to 14 days beyond symptom onset. The intimal flap that separates the two lumens is very compliant and fluctuates drastically in the flow with each cardiac cycle. Flow in the true lumen or its side branches may be occluded by the flap resulting in malperfusion and ischemic damage of vital organs or extremities. During this phase there is a high risk of rupture of the false lumen wall that typically occurs at the site of the primary entry tear. The chronic phase in an aortic dissection begins after the second month. The intimal flap shortens, thickens and becomes stiffer due to scarring and biochemical responses to the event creating a double-barreled appearance with the true and false lumen. The false lumen dilates becoming much larger than the true lumen and though the risk for rupture is still present it is lower than the extremely high initial death rate during the acute phase.

Although the etiology of aortic dissection is not well defined and the precise triggering events remain unclear, several predisposing factors have been identified [6]. Aortic dissection occurs generally in patients with hypertension, congenital diseases affecting the structural or elastic integrity of the aorta (Marfan’s syndrome, bicuspid valve, Ehlers-Danlos syndromes), or blunt trauma. An experimental model will allow for the study of conditions that are difficult or impossible to measure directly in humans experiencing an aortic dissection. It is generally accepted that mechanical stresses within the aortic wall play a significant role in the genesis of dissections. From a mechanical perspective, tear and dissection appear when the stresses acting on the wall rise beyond the wall’s elastic limit.

1.2 Motivation

There are no biological, physical or animal models of thoracic aortic dissection that can explain the mechanics and evolution of these lesions. The few physical models that have been used to mimic a thoracic aorta consisted of tubes with rigid or flexible walls that do not possess the mechanical properties of a human aorta. Animal models of human aortic dissection have been attempted by surgically lifting a flap in the normal aorta of an animal, but the resulting preparation does not have the geometry or the mechanical properties of a dissected human aorta. In addition, neither the physical nor the animal models reproduce the interacting variables, such as elasticity, intra-luminal thrombus, anisotropy, asymmetric dilation, and others that determine the mechanical behavior of a human aorta that is prone to or has developed a dissection.

The goal of this research is to build an experimental bench-top model of aortic dissection flow and wall mechanics which emulate the forces and appearance of a dissection and explain the flow/pressure events that affect the stability or progression of a dissection. The operation of such a model will permit ranking the variables that determine the evolution of a dissection towards aneurysm formation or rupture.

In addition we investigate a method to determine the elastic values of the walls of an aorta from dynamic CT (Computerized tomography) DICOM files of patients with aortic dissection. The concept of this algorithm will be verified, in terms of elastic parameters, by obtaining dynamic CT images of a phantom model at various heart rates and modulus of elasticity and comparing it with the elasticity values obtained for the material used in the phantom model on a tensile testing machine.

A fundamental understanding of how dissections grow and rupture is paramount to intelligent treatment strategies. This work is driven by the following hypotheses. The underlying biomechanical mechanism of aortic dissection results from material property differences, probably induced by biochemical changes, in the layers of the aortic wall that lead to shearing of the media, intramural hematoma and subsequent tearing of the intima with the formation of two channels of flow.

The dynamic behavior and the risk of enlargement and rupture of a dissected aorta are determined by biomechanical stresses. The elastic properties of an aorta may be determined from existing pressure/ flow conditions and from changes in its geometry that can be derived from dynamic cardiac-gated Computerized Tomography (CT) imaging.

1.3 Models and Assumptions

The few physical models of aortic dissections attempt to reproduce the aortic dissection structure with rigid or flexible tubing that does not have the mechanical properties of human aortas. Chung et al. [7, 8] investigated the factors that lead to true-lumen collapse in a model of aortic dissection. The compliant material used for the intimal flap was a bicycle tire inner tube and the true lumen was made of dilated polytetrafluorethylene (PTFE). None of these elements behave mechanically like their equivalence in the human dissected aorta. We built a flexible wall bench-top-model of aortic dissection to emulate the forces and appearance of a dissection. The components of the model were of known elastic modulus similar to those of a human aortic dissection. This may help explain the flow/pressure events that affect the stability or progression of a dissection. This work may also be used as a benchmark to validate numerical models of aortic dissection and develop a fundamental knowledge of the flow characteristics and flap behavior under various physiological conditions.

1.3.1 Mechanical Properties of Arterial Wall

Previous studies of the mechanical properties of the arterial wall required invasive measurements and aortic tissues [9-12]. In this study we propose a new non-invasive measurement of the mechanical properties of a live aortic specimen using dynamic DICOM files. The proposed method will be validated by measuring the elasticity of a phantom aorta made from polydimethylsiloxane (PDMS), a material of known elasticity interposed in a circulatory bench flow loop. The measurements will be derived from dynamic DICOM files obtained from an ECG-gated 64-slice CT scanner. This technique will allow us to perform complete dynamic quantitative analysis of an intact living vessel. The information provided by CT angiograms will be used to estimate *in vivo* the mechanical properties (e.g. Young's modulus) of healthy and diseased regions within the same vessel and will facilitate the prediction of the natural history of aortic dissection in a particular patient. The proposed method opens a new horizon in determining non-invasively the mechanical properties of a living and functioning human aorta using dynamic DICOM files. The proposed method will allow the determination of the physical properties of any vascular wall in-vivo and hence will contribute significantly to predict the outcomes of aortic aneurysms and dissections.

1.4 Objectives

Mechanical properties of the PDMS material used to create experimental models of aortic dissections will be investigated in Chapter 2. It will include the range of elastic modulus of the material that can be developed as well as its response to various physiological parameters. In Chapter 3 we will develop a bench-top flow loop to emulate flow conditions of the human aorta under normal and diseased conditions. This will be used in a novel method for non-invasive measurements of the elasticity of living aortas in-vivo. In Chapter 4 we will build models of both chronic and acute aortic dissections. We will investigate flow characteristics of the two lumens and the geometrical conditions that affect pressure changes and wall stresses in them. Such a model does not currently exist, and would substantially improve the understanding of the various biomechanical factors involved in aortic dissections.

1.5 Literature Cited

[1] WHO. (2009, December 4, 2010). *Cardiovascular diseases* (*CVDs*), Fact sheet N°317. Available: http://www.who.int/mediacentre/factsheets/fs317/en/index.html.

[2] W. D. Clouse*, et al.*, "Acute Aortic Dissection: Population-Based Incidence Compared With Degenerative Aortic Aneurysm Rupture," *Mayo Clinic Proceedings,* vol. 79, pp. 176-180, 2004.

[3] I. Meszaros*, et al.*, "Epidemiology and Clinicopathology of Aortic Dissection*," *Chest,* vol. 117, pp. 1271-1278, 2000.

[4] D. S. Wang and M. D. Dake, "Endovascular therapy for aortic dissection," in *Thoracic Aortic Diseases*, H. Rousseau*, et al.*, Eds., ed New York: Springer, 2006, pp. 189 - 197.

[5] J. I. Fann and D. C. Miller, "Aortic Dissection," *Annals of Vascular Surgery,* vol. 9, pp. 311-323, 1995.

[6] M. A. Coady*, et al.*, "PATHOLOGIC VARIANTS OF THORACIC AORTIC DISSECTIONS: Penetrating Atherosclerotic Ulcers and Intramural Hematomas," *Cardiology Clinics,* vol. 17, pp. 637-657, 1999.

[7] J. W. Chung*, et al.*, "True-Lumen Collapse in Aortic Dissection 1," *Radiology,* vol. 214, pp. 87-98, 2000.

[8] J. W. Chung*, et al.*, "True-Lumen Collapse in Aortic Dissection 1," *Radiology,* vol. 214, pp. 99-106, 2000.

[9] D. H. Bergel, "Static Elastic Properties of Arterial Wall," *Journal of Physiology-London,* vol. 156, pp. 445-457, 1961.

[10] P. B. Dobrin, "Mechanical-Properties of Arteries," *Physiological Reviews,* vol. 58, pp. 397-460, 1978.

[11] R. B. Hickler, "Aortic and large artery stiffness: Current methodology and clinical correlations," *Clinical Cardiology,* vol. 13, pp. 317-322, 1990.

[12] M. Sherebrin, et al., "Effects of age on the anisotropy of the descending human thoracic aorta determined by uniaxial tensile testing and digestion by NaOH under load," Canadian journal of physiology and pharmacology, vol. 67, pp. 871 - 878, 1989.

Chapter 2

Mechanical Behavior of Polydimethylsiloxane (PDMS) Material as Related to its Biological Applications [1]

2.1 Introduction

We use polydimethylsiloxane (PDMS) to create models of arteries to study flow characteristics using a bench-top flow loop. The advantages of PDMS over other materials include low cost, optical transparency and relatively easy manufacturability. PDMS, due to its unique properties, has been used to fabricate lab-on-a chip [2] and a microarray for DNA analysis, micro-fluidic components for biomedical applications, MEMS and BioMEMS [3-7]. Mata et al. [8] studied the properties of PDMS for biomedical micro/nanosystems using different mixing ratios. To our knowledge, the estimation of the mechanical properties of the PDMS elastomer as they relate to physiological conditions has not been published in the literature for various mixing ratios and stretch speed.

This study is to determine the mechanical properties of the PDMS elastomer for various mixing ratios and to achieve a more physiologically relevant range of mechanical properties that can be used to model arteries. A secondary objective is to study the effect of the strain rate on the tensile properties of the PDMS elastomer. Different stress-strain curve definitions have been found in literature to determine the elasticity of human tissue (e.g. engineering stress-strain curve or true stress-engineering strain curve). However, the engineering stress-strain curve or true stress-engineering strain curves do not give a true indication of the deformation characteristics since they are based on the original dimensions of the specimen, and these dimensions change continuously during the test, as reported earlier by Duprey et al. [9]. Therefore, the third objective of this work is to conduct a thorough analysis and show the effect on the mechanical properties of the PDMS elastomer by varying the stress-strain curve definition. We have not found in scientific literature an analysis of the variance of the stress-strain curve definition for PDMS elastomer. This study paves the road for the researchers to select the required mixing ratio of the PDMS elastomer that give similar mechanical properties of a human tissue of particular interest.

2.2 Materials and Methods

2.2.1 PDMS preparation

PDMS Sylgard 184 silicon elastomer (Dow Corning Corporation, Midland, MI) consists of a pre-polymer (A: base) and cross-linker (B: curing agent) that are typically mixed at different weight ratios (ratio of A:B). Different mechanical properties are achieved with different mixing ratios to obtain a physiologically relevant range that would be of interest to the research community. To prepare PDMS elastomer with different elastic moduli, the silicon polymer base and curing agent are mixed thoroughly at various mixing ratios. Since air bubbles are usually trapped during mixing, the mixture is placed in a vacuum chamber for degassing at 25 inHg until the bubbles are removed. The mixture is then poured into an aluminum casting mold (see Figure 2.1). Care should be taken when pouring the mixture into the mold, to minimize air entrapment. The mold is then placed in a vacuum chamber at 29 inHg for an additional 4 hours of degassing. Thereafter, the mold is placed into an oven at 65 ^{o}C to cure for 12 hours.

2.2.2 Mechanical Properties of the PDMS elastomer

The mechanical properties of the PDMS elastomer were determined in a tensile testing machine (Instron, Inc, Norwood, MA). The dog-bone shaped specimen of the PDMS elastomer was designed according to ASTM standards (Figure 2.2) and was mounted in the grips of the Instron machine at a specified gauge length of 25 mm. The displacement and the corresponding force during the test were recorded automatically using LabView software. The force and displacement data were transformed into true stress and true strain using the assumption that the volume of the specimen was conserved with Poisson's ratio of 0.5. The true stress, which is defined as the ratio of the applied force (F) to the current cross-sectional area of the specimen (A), is defined as follows:

$$\sigma = \frac{F}{A} \tag{2-1}$$

Since there is no volume change in the specimen, the true stress can be related to the engineering stress (σ_E) and engineering strain (ε_E) as:

$$A \times L = A_o \times L_o \Rightarrow \sigma = \frac{F}{A} = \frac{F}{A_o}\frac{L}{L_o} = \sigma_E\left(1 + \varepsilon_E\right) \tag{2-2}$$

Where L_o is the initial length, $\varepsilon_E = \frac{\Delta L}{L_o}$, ΔL is the elongation, and $\sigma_E = \frac{F}{A_o}$. The true strain is defined as the sum of all instantaneous engineering strains. Therefore,

$$\varepsilon_T = \int d\varepsilon = \int_{L_o}^{L_f} \frac{dL}{L} = \ln \frac{L_f}{L_o} = \ln \frac{L_o + \Delta L}{L_o} = \ln(1 + \varepsilon_E) \tag{2-3}$$

The curve of stress versus strain was plotted for each mixing ratio at various crosshead speeds of the tensile testing machine. The slope of the curve at any point gives the incremental modulus, E. Thus,

$$E = \frac{d\sigma}{d\varepsilon} \tag{2-4}$$

Curve fitting was done using Excel 2003. A third-order polynomial was found to provide the best fit and the elastic modulus formula was obtained by differentiating the closest fitting curve. It is very important to know the value of the modulus that should be used when modeling different aortic diseases for determining the development and eventually their rupture under physiological conditions.

2.3 Results and Discussion

2.3.1 Effect of the Stress-Strain Curve Definition on the Mechanical Behavior of the PDMS Elastomer

Figure 2.3 illustrates a comparison of the stress-strain curve between engineering stress-strain, true stress-engineering strain and true stress-strain definitions on the mechanical behavior of the PDMS elastomer at two different crosshead speeds (i.e. strain rate). It can be seen from this figure that the true stress-strain curve is indistinguishable from the true stress-engineering strain and engineering stress-strain curve at small strains. However, as the strain becomes large and the cross-sectional area of the specimen decreases, Figure 2.3 shows that the true stress-strain curve can be much larger than the true stress-engineering strain curve and the engineering stress-strain curve. Figure 2.4 shows the elasticity parameter (e.g. Young's modulus) calculated using different definitions of the stress-strain curve. The engineering stress-strain curve is linear yielding a constant elastic modulus calculated at any point on the slope. Figure 2.4 demonstrates that the true stress-engineering strain curve and true stress-strain curve are nonlinear and therefore, curve fitting was done using a third-order polynomial equation. The elastic modulus formula was obtained by calculating the derivative of the third-order polynomial equation. The elastic modulus for true stress-strain curve increases significantly at higher strains compared with other curves. This increase is evident at the higher crosshead speed of 500 mm/min. Figure 2.3 and Figure 2.4 show that the stress-strain curve and the corresponding elastic modulus depend substantially on the stress-strain definition.

2.3.2 Effect of the Mixing Ratio on the Elastic Modulus

The effect of the mixing ratio on the elastic modulus using engineering stress-strain curve and true stress-strain curve at different crosshead speeds is shown in Figure 2.5. It can be seen from this figure that the elastic modulus increases as the mixing ratio increases until it reaches a maximum value at around a mixing ratio of 9:1. However, as the ratio is increased beyond this level to ratios of 10:1 and more the elastic modulus starts to decrease. This may be associated with the fact that given the high ratio of base present the cross-linker is unable to associate with all of the base molecules , thus, the higher the portion of the base in the PDMS the more un-reacted base polymer is present and the lower the elastic modulus. Figure 2.5 shows that the elastic modulus increases significantly using true stress-strain curve compared with the engineering stress-strain curve. To accurately mimic blood flow in-vitro the elastic modulus should be determined in the range of physiological values. Figure 2.6 shows the effect of the mixing ratio on the elastic modulus in the range of physiological values using different stress-strain curves. The elastic modulus in the range of physiological values was determined under physiologically relevant arterial pressures between 70 and 160 mmHg. This is the first comprehensive figure in literature to show the elastic modulus in the range of physiological values for various mixing ratios and crosshead speeds. Better understanding of vascular diseases and testing of endografts require in-vitro experiments and knowledge of the biomechanical properties of the arterial wall. Once the elastic modulus of an arterial wall is determined, the corresponding mixing ratio of the PDMS elastomer may be selected from Figure 2.6.

2.3.3 Effect of the Strain Rate on the Elastic Modulus

The effect of the strain rate (or crosshead speed) on the elastic modulus of the PDMS elastomer using different definitions of the stress-strain curve and mixing ratios is depicted in Figure 2.7. It can be seen from this figure that the elastic modulus increases with the increase in strain rate. This behavior has been observed in elastic testing of circumferential strips from animal carotid arteries [10].

2.3.4 Effect of the Stress-Strain Curve Definition on the Elastic Modulus

The effect of the stress-strain curve definition on the physiological relevant elastic modulus is depicted in Figure 2.8. It can be seen from this figure that for a mixing ratio of 6:1 the elastic modulus depends strongly on the stress-strain curve definition and the strain rate. For stiffer PDMS elastomer (mixing ratio of 9:1), the elastic modulus depends mainly on the definition of the stress-strain curve over the range of the crosshead speeds considered in this study.

2.4 Conclusions

There is little quantitative knowledge regarding the effect of mixing ratio, strain rate, and the definition of the stress-strain curve on the behavior of the PDMS material. The mechanical behavior of the PDMS material was determined in this study for various mixing ratios and strain rates using a tensile testing machine to quantify the ability of the PDMS to reflect the actual strain a soft tissue would experience. The results of this study demonstrate that elastic modulus increases as the mixing ratio increases to 9:1 after which the elastic modulus decreases as the mixing ratio continues to increase. Moreover, our results showed that the elastic modulus in the physiological range depends substantially on the definition of the stress-strain curve, mixing ratio, and strain rate. As such, the true stress-strain definition reveals higher stress and elastic modulus compared with engineering stress-strain and true stress-engineering strain definitions for various mixing ratios and strain rates.

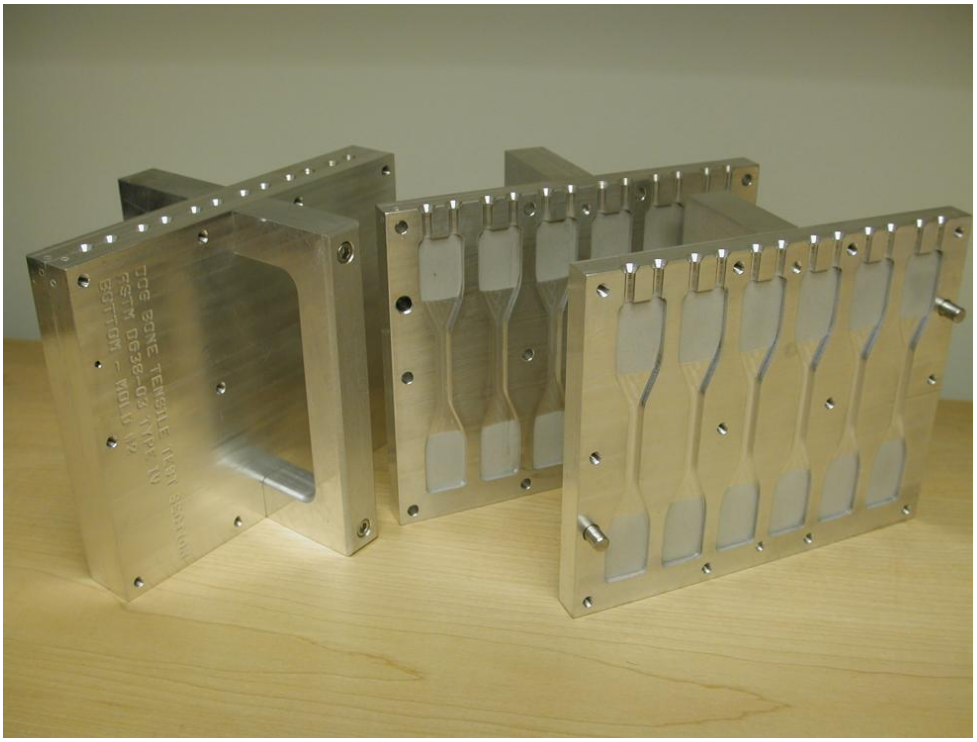

Figure 2.1 Tensile test section mold

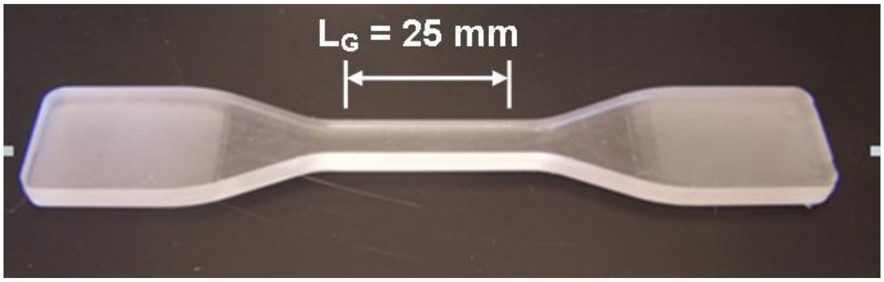

Figure 2.2 Schematic illustration of the PDMS elastomer used for tensile testing. Dimensions are according to ASTM standards *(Gauge length L_G = 25 mm, Width = 6 mm, Thickness = 4 mm)*

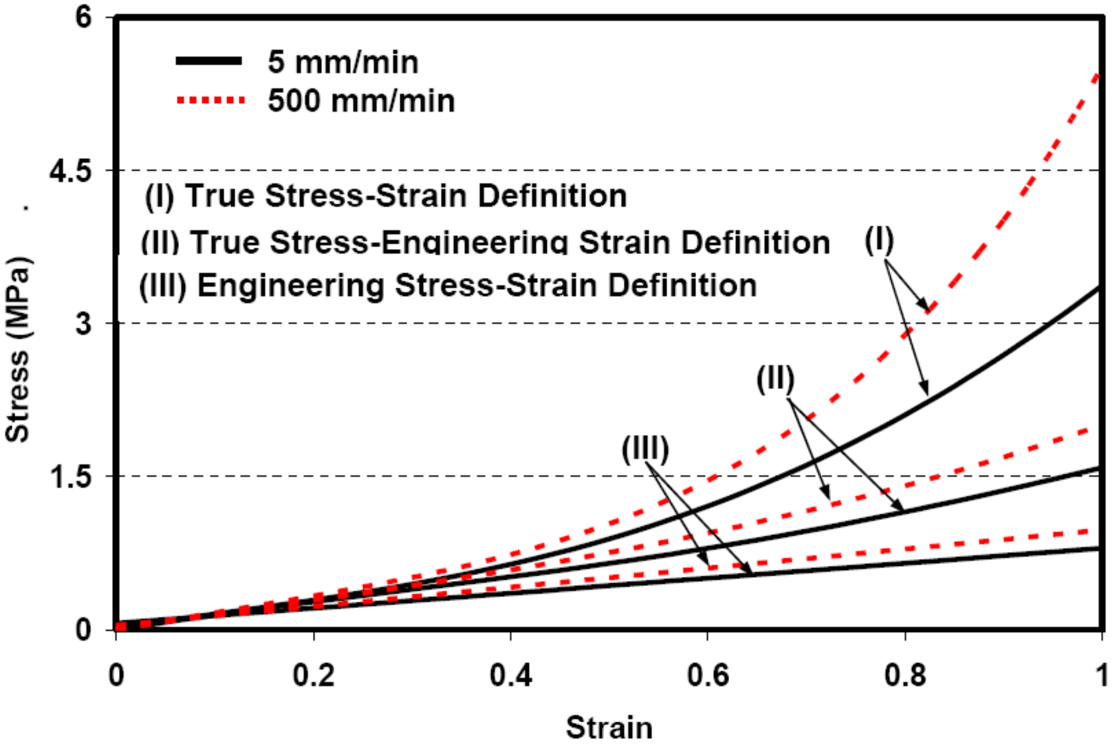

Figure 2.3 Comparison of the tensile stress-strain curve using different definitions at different crosshead speeds (Mixing ratio 6:1)

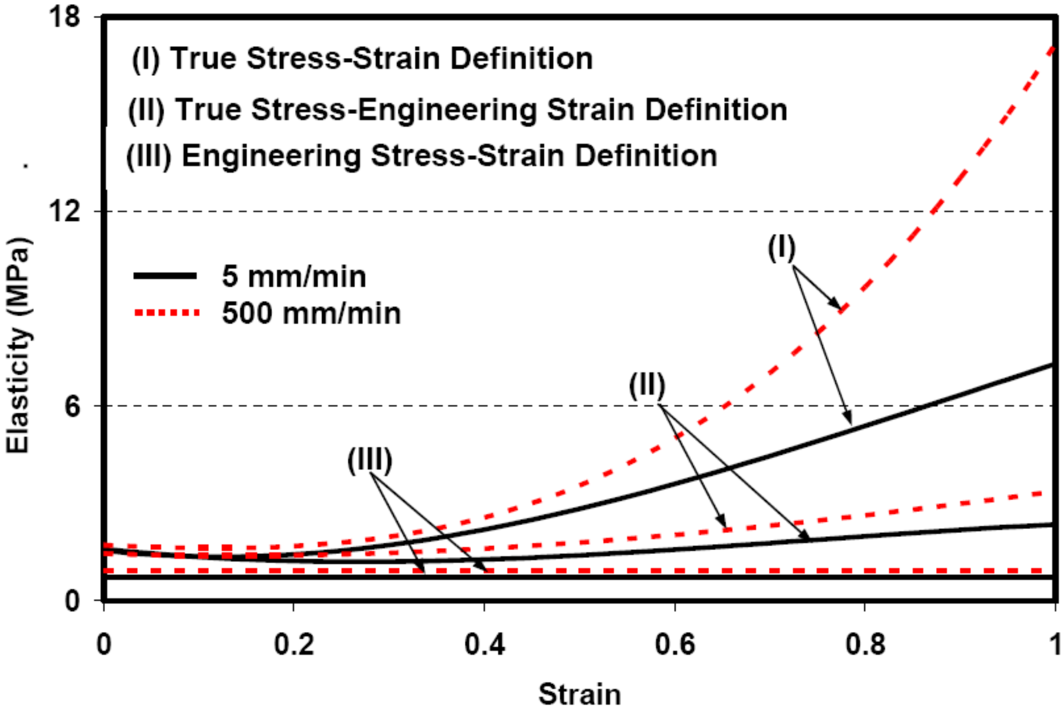

Figure 2.4 Comparison of the Elasticity using different stress-strain definition at different crosshead speeds (Mixing ratio 6:1)

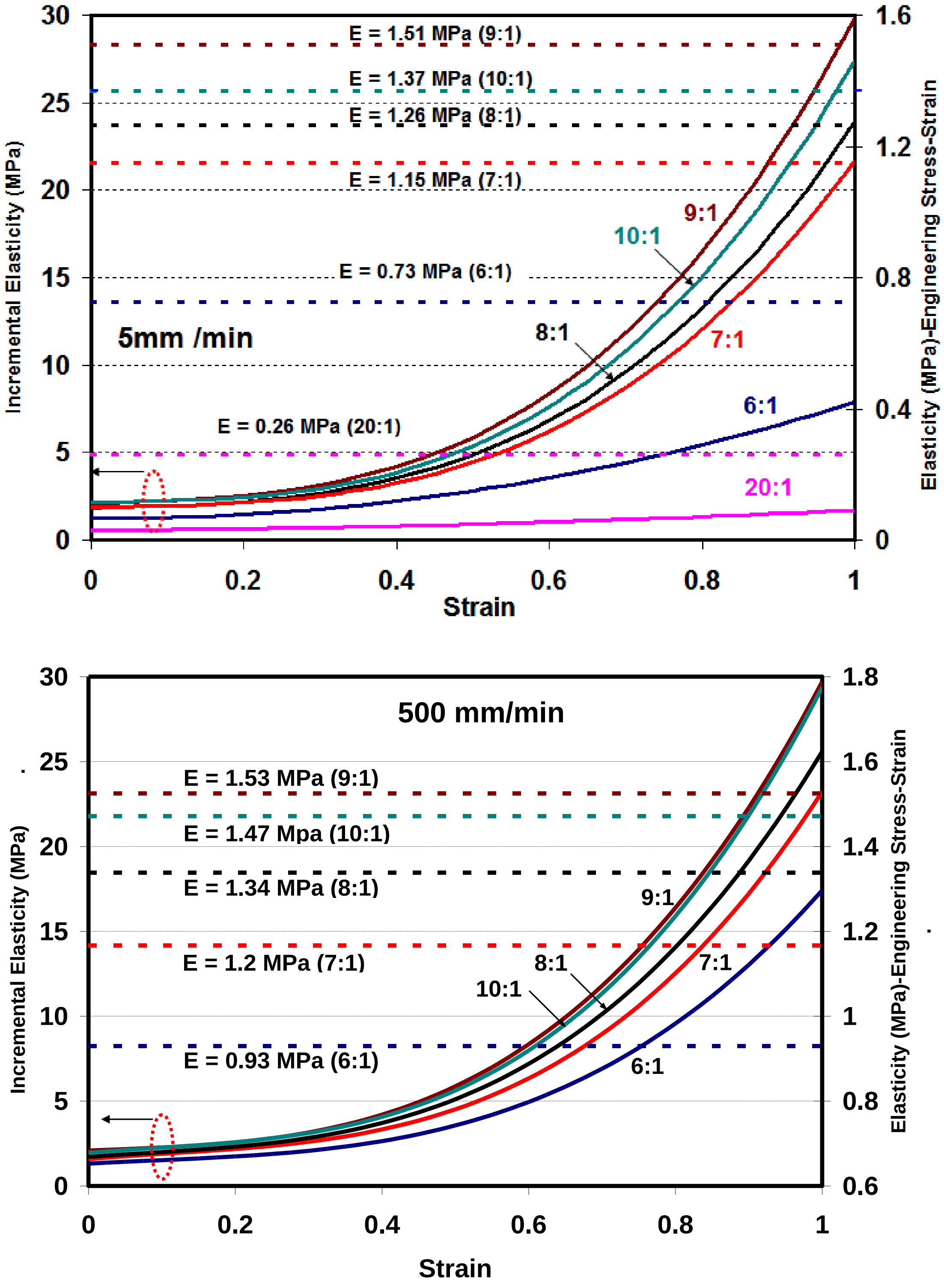

Figure 2.5 Effect of the mixing ratio on the elastic modulus using engineering stress-strain and true stress-strain curves at different crosshead speeds

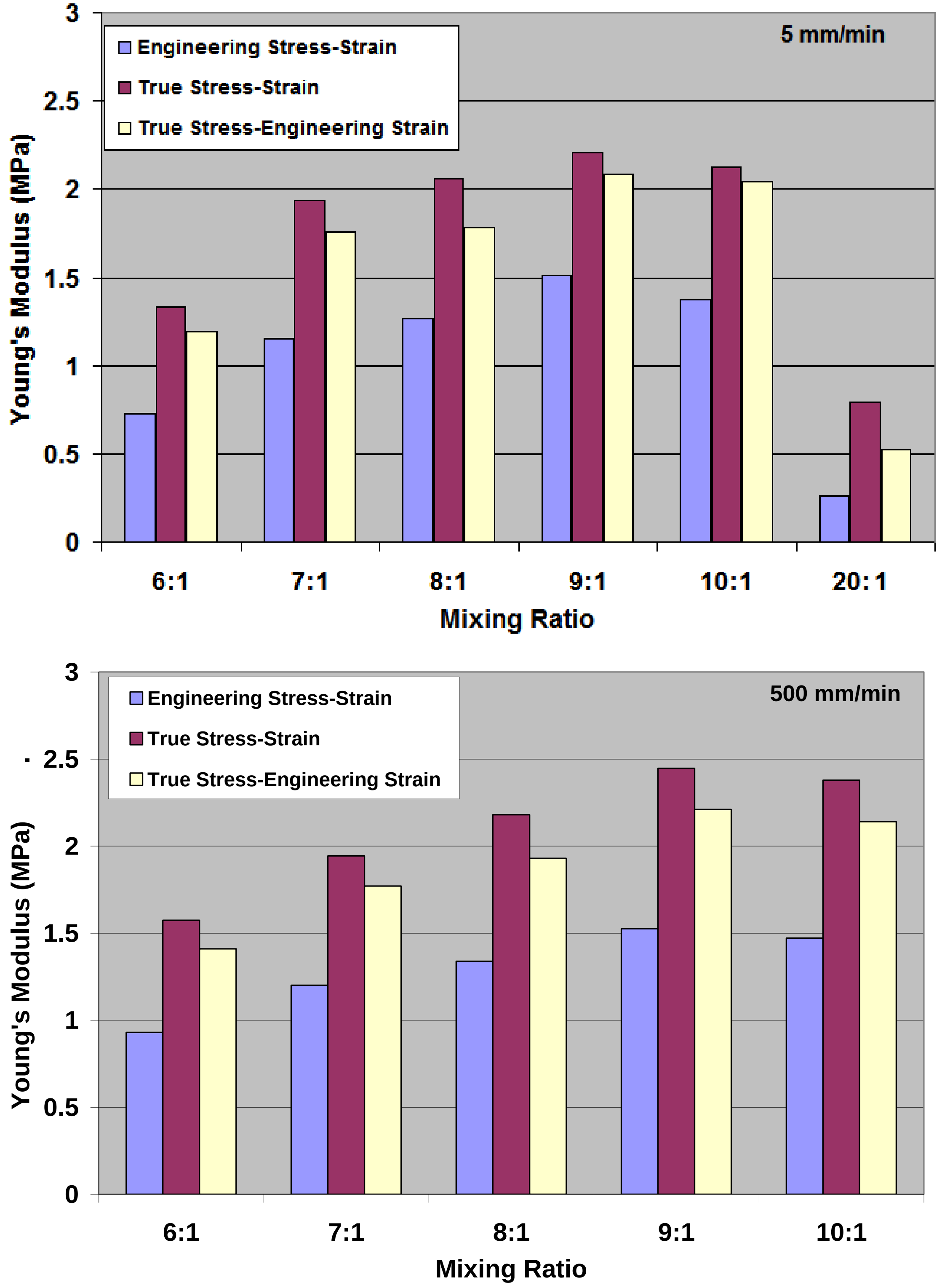

Figure 2.6 Effect of the PDMS mixing ratio on Young's modulus in the physiological range using different stress-strain definition at different crosshead speeds

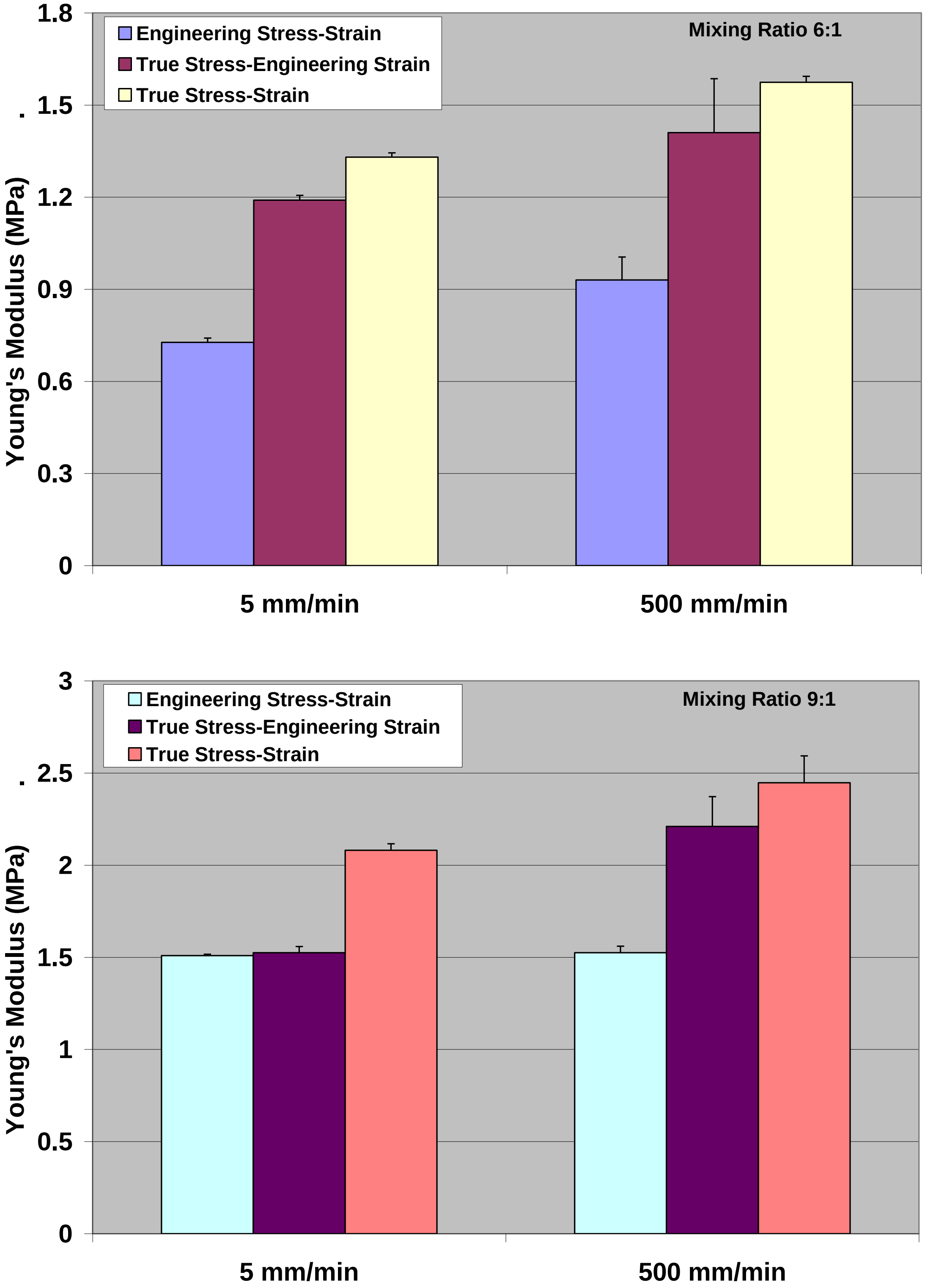

Figure 2.7 Effect of the crosshead speed on Young's modulus in the physiological range using different mixing ratios

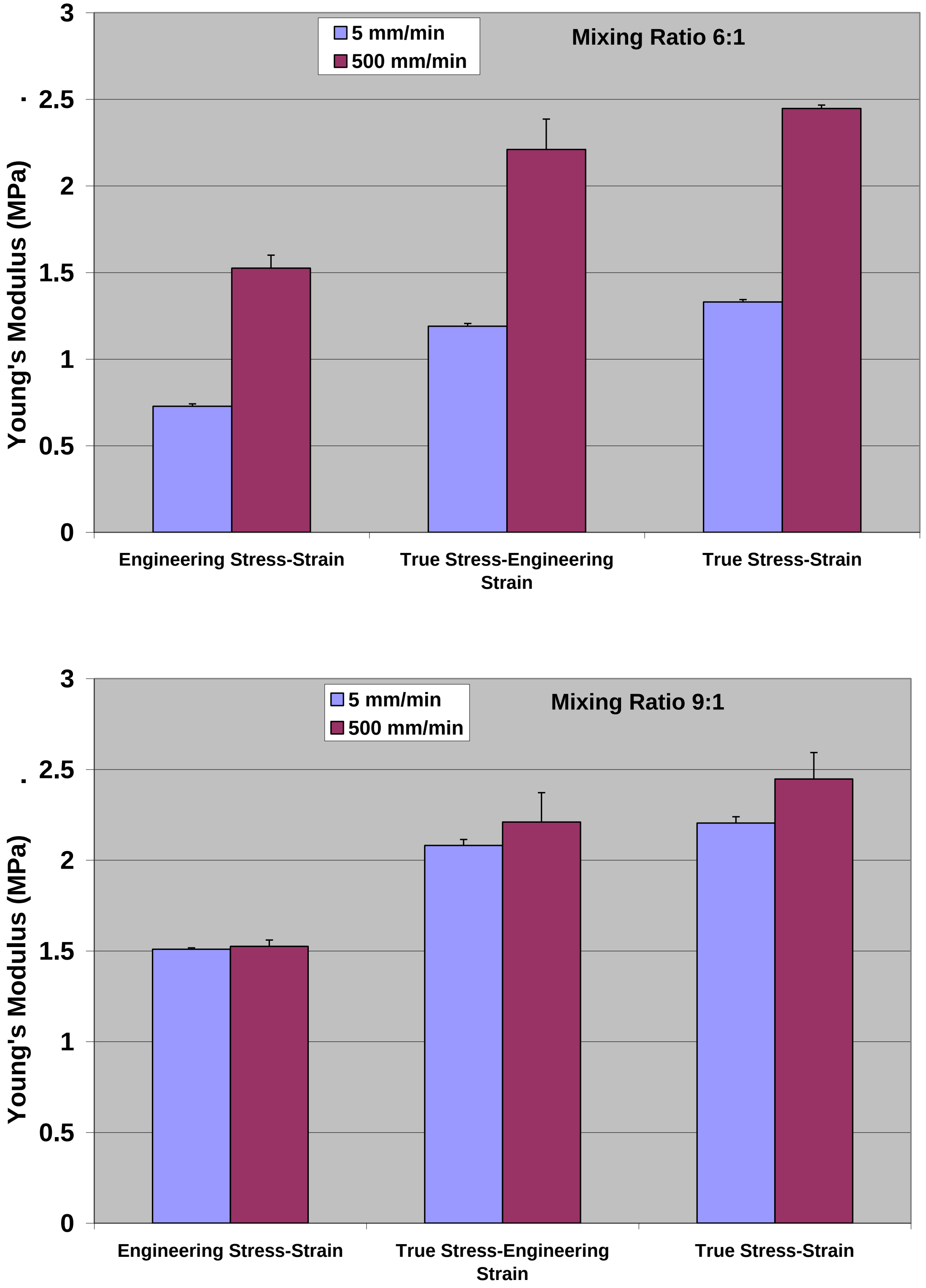

Figure 2.8 The effect of stress-strain definition on Young's modulus in the physiological range at various crosshead speeds and mixing ratios

2.5 References

[1] K. Khanafer*, et al.*, "Effects of strain rate, mixing ratio, and stress-strain definition on the mechanical behavior of the polydimethylsiloxane (PDMS) material as related to its biological applications," *Biomedical Microdevices,* vol. 11, pp. 503-508, Apr 2009.

[2] M. Liu and Q. Chen, "Characterization study of bonded and unbonded polydimethylsiloxane aimed for bio-micro-electromechanical systems-related applications," *Journal of Micro/Nanolithography, MEMS and MOEMS,* vol. 6, pp. 023008-6, 2007.

[3] M. A. Unger*, et al.*, "Monolithic Microfabricated Valves and Pumps by Multilayer Soft Lithography," *Science,* vol. 288, pp. 113-116, 2000.

[4] R. Bashir, "BioMEMS: state-of-the-art in detection, opportunities and prospects," *Advanced Drug Delivery Reviews,* vol. 56, pp. 1565-1586, 2004.

[5] A. Mata*, et al.*, "Growth of connective tissue progenitor cells on microtextured polydimethylsiloxane surfaces," *Journal of Biomedical Materials Research,* vol. 62, pp. 499-506, 2002.

[6] A. Mata*, et al.*, "Osteoblast attachment to a textured surface in the absence of exogenous adhesion proteins," *NanoBioscience, IEEE Transactions on,* vol. 2, pp. 287-294, 2003.

[7] J. C. McDonald and G. M. Whitesides, "Poly(dimethylsiloxane) as a Material for Fabricating Microfluidic Devices," *Accounts of Chemical Research,* vol. 35, pp. 491-499, 2002.

[8] A. Mata*, et al.*, "Characterization of Polydimethylsiloxane (PDMS) Properties for Biomedical Micro/Nanosystems," *Biomedical Microdevices,* vol. 7, pp. 281-293, 2005.

[9] A. Duprey*, et al.*, "In Vitro Characterisation of Physiological and Maximum Elastic Modulus of Ascending Thoracic Aortic Aneurysms Using Uniaxial Tensile Testing," *European Journal of Vascular and Endovascular Surgery,* vol. 39, pp. 700-707, 2010.

[10] B. D. Stemper, et al., "Biomechanical characterization of internal layer subfailure in blunt arterial injury," Annals of Biomedical Engineering, vol. 35, pp. 285-291, Feb 2007.

Chapter 3

A Method for *In-vivo* Measurement of the Elasticity of the Aorta in CT Angiograms

3.1 Introduction

Knowledge of the biomechanical properties of the arterial wall is crucial for understanding the changes brought to the cardiovascular system by aging, arteriosclerosis, and hypertension. Changes in elasticity determine the beginning and outcome of vascular diseases such as aortic dissections and aneurysms. The elasticity of a recipient artery may also be important in the design or choice of endovascular stents or stent-grafts [1-4].

Previous studies of the mechanical properties of the aorta (e.g elasticity and Poisson's ratio) have lead to several constitutive models [5-11]. However; these properties have been estimated *in-vitro* from autopsy or surgical specimens and may be different from those in living aortas. Due to the difficulty of measuring elasticity *in-vivo,* there have only been a handful of animal studies that have compared *in-vivo* measurements with results from *in-vitro* studies [9, 12-16]. In the only comparative study found in the literature, Zanchi et al. [13] showed that the mechanical properties of the rat carotid artery differed substantially *in-vivo*, *in-situ*, and *in-vitro*.

Imaging technologies have substantially improved our knowledge of arterial wall dynamics under diseased and normal conditions [17-24]. In recent years, several methods (e.g. Speckle Tracking Technique [25, 26], Array-Transducer Catheter [27]) have been developed for tracking motion of soft tissue. Multidetector Computed Tomography (MDCT) technology with retrospective electrocardiographic-gating (ECG) has been used to provide cardiac images with high temporal resolution [28-30]. Recently, MDCT was used to evaluate vessel distensibility: a physical characteristic of the vessel wall important for grading vascular disease [31-33]. Ganten et al. [31] calculated change in aortic cross-sectional area and developed an image reconstruction algorithm to calculate aorta diameter and area as a function of the cardiac cycle. Their algorithm was tested on porcine aortic specimens and was compared with an optical reference method (CCD camera). The error of the relative vessel area comparing the two methods was found to be about 3%. Zhang et al. [32] prospectively examined vessel distensibility measurements by using ECG-gated Computed Tomography (CT) on a phantom and compared the results with measurements using a digital camera. The authors observed that CT distensibility measurements agreed well with the optical measurements. Ganten et al. [33] determined the distensibility changes in 67 patients with abdominal aortic aneurysms (AAA) using ECG-gated four detector-row CT system. Ganten et al. [34] also investigated distensibility changes in 32 patients with chronic Stanford Type B aortic dissection.

The authors cited above used ECG-gated CT systems to obtain quantitative information on the elastic properties of vessel wall using a distensibility coefficient. This study proposes an innovative non-invasive method of determining the elastic modulus of the arterial wall based on dynamic DICOM files (Digital Imaging and Communications in Medicine) using high resolution CT scanning (64-slice multidetector CT scanner with ECG-gating). Therefore, the aim of this investigation was to prove that the elastic parameters derived in an aortic phantom using a Computed Tomography Angiogram (CTA) protocol (64-slice multidetector CT scanner with ECG-gating) correlated with actual elastic measurements obtained from a tensile testing machine.

3.2 Materials and Methods

Wall material may be characterized by Young's modulus, E, which is the ratio of stress and circumferential strain in the vessel wall. We used true strain and true stress to determine E as outlined in Section 2.2.2 except for this experiment stress was first calculated using Lamé's equation:

$$\sigma = \frac{P(r)}{t} \tag{3-1}$$

where σ is engineering stress, P is pressure, r is the radius and t is the wall thickness of the vessel. And the strain was determined by the equation:

$$\varepsilon = \frac{A - A_{\min}}{A_{\min}} \tag{3-2}$$

where ϵ is the engineering strain, A is the measured area of interest and $A_{\min}$ is the minimum cross-sectional area at end diastole.

To estimate the elasticity values, time-dependent measurements of the cross-sectional area of a phantom model and the arterial pressure were made during each phase of the cardiac cycle along the model. The minimum and maximum cross-sectional areas of the inner lumen were determined from the CT imaging data. The model was made of polydimethylsiloxane (PDMS) material and its mechanical properties were predetermined in a tensile testing machine as described in Chapter 2. The proposed method was validated by comparing the elasticity measurements obtained with the CT data with the known values of elasticity for the PDMS from our tensile tests.

3.2.1 Experimental Setup

The setup consisted of a pulsatile pump with a phantom test section in a bench-top flow loop. The flow loop was constructed to simulate physical properties of a human vascular system under normal and diseased conditions. This experimental model allows us to examine pulsatile flow effects of flexible-wall aortic models and record responses of flow and wall structure. The model is full scale and is compatible to study flow around endovascular devices as well.

3.2.1.1 Design of Bench-top Flow Loop

A bench-top flow loop (Figure 3.1) was constructed to simulate physical properties of a human vascular system under normal and diseased conditions. This experimental model allows us to examine pulsatile flow effects of flexible-wall aortic models and record responses of flow and wall structure. The model is full scale and is compatible to study flow around endovascular devices as well.

3.2.1.1.1 Heart Pump

Flow in the system was provided with a pulsatile heart pump (Model 1421, Harvard Apparatus Inc., Holliston, MA). This model provides a maximum of thirty cubic centimeters of output per stroke and did not meet the design requirements. The ventricular cardiac output of the human heart ranges from sixty to one-hundred-and-twenty cubic centimeters per stroke. Therefore the existing pump was re-tooled, in order to meet the requirements, with a larger motor and pump head. The pump is now similar to the Model 1423 with a maximum stroke volume of one hundred cubic centimeters per stroke. A cam micro-switch was installed to synchronize the new motor as shown in the wiring diagram Appendix C, C.1 – Wiring diagram of Heart Pump). A second cam micro-switch was also installed, as seen in the wiring diagram, for external triggering of equipment and monitoring pump frequency in the Labview software. The pump is also adjustable for heart rate, stroke volume and phase ratio (i.e. systole/diastole) to simulate pulsatile left ventricular output.

3.2.1.1.2 Tubing and Connectors

Clear Tygon tubing, 1/2” I.D. with 1/8” thick walls (McMaster Carr Company) was used for the majority of the flow loop. A less compliant clear ether-based polyurethane tubing 5/8" I.D. with 3/32" thick walls (McMaster Carr Company) was used for the supply line from to the heart pump to prevent collapse as the pump pulls fluid from the reservoir. To eliminate minor fluctuations in the pressure readings, a 5/8” diameter x 6” long double-walled section of penrose tubing was added just after the pump head. The fluctuations were from the ball valves chattering as fluid rushed by them; this noise was being picked up by the transducers. A twenty liter HDPE carboy (Thermo Scientific, Madison, WI) container is used as a reservoir for the fluid. The fluid temperature is maintained at 38°C by a Micro-Temp II ® Hyperthermia Water System (Cincinnati Sub-Zero Products, Inc.) Heat is transferred by water from the Micro-Temp II to the model fluid via a BioTherm Heat Exchanger from Medtronic Inc. The glass connectors (See Appendix A, A.20 - PIV connector 1 - sheet 1 of 1, A.21 - PIV connector 2 - sheet 1 of 2 and A.22 - PIV connector 2 - sheet 1 of 2) proximal and distal to the test model are tapered to achieve a less turbulent flow when transitioning from the 1/2” tubing to the larger diameters of the test model. There are also port holes where luer connectors are set in epoxy for connecting the pressure transducers.

3.2.1.1.3 Capacitance and Resistance

The capacitance device utilizes a spring mounted piston; springs with various k-values are utilized to obtain the desired pressure during diastole. Detailed drawings of the capacitance device may be seen in Appendix A, A.7 – Capacitance assembly – sheet 1 of 1. This device acts as a windkessel effect, storing the energy from the bolus of fluid during systole, and recoiling when the pump head retracts during diastole. This way pressure and flow are maintained when the pump or, cardiac ejection cease. Adjustable tube clamps (Castaloy hosecock screw-type clamp, Thermo Scientific, Madison, WI) are used before and after the compliance chamber to adjust peripheral resistance comparable with physiologic values. The clamp prior to the pump adjusts for overall mean pressure while the two clamps distal to the capacitance device adjust the diastolic pressure.

3.2.1.1.4 Monitoring Equipment

An ultrasonic transit-time sensor flow meter is used to measure the flow rate (Transonic Systems Inc, Ithaca, NY). A type K thermocouple (GIC Thermodynamics, Inc., Royal Oak, MI) is used in the flow loop to monitor the temperature as well as a pressure transducer (AD Instruments, Model MLT-3018, Colorado Springs, CO) both proximal and distal to the test section. And a DAQ System model SC-2345 from National Instruments is used to collect the signals and display them in the LabView software (see Appendix B, B.1 - Labview front panel, B.2 - Labview block diagram) on an XPS M1730 laptop from Dell.

The entire setup may be recorded with the Sony color video camera, model DXC-930, Sony camera control unit, model CCU-M5, remote pan/tilt and Panasonic DVD recorder. The camera image as well as the Labview front panel from the laptop can both be viewed on a Westinghouse 19” flat panel TV monitor, model LTV-19W3. This allows spectators to view the live data from either side of the display as well as facilitate adjustments being made to resistance and capacitance around the table. Ultrasonography imaging as well as particle imaging velocimetry (PIV) studies may also be performed on test models in the flow loop.

3.2.2 Polydimethylsiloxane (PDMS) Preparation

PDMS (Sylgard 184, Dow Corning Corp., Midland, MI) prepolymer (A: base) and cross-linker (B: curing agent) were mixed at various weight ratios: 6:1, 8:1, and 9:1 (ratio of A : B) to prepare phantom models and tensile testing specimens in this study. Different ratios result in polymers of different Young's moduli. Parts A and B were mixed at these ratios and then placed in a vacuum chamber at 25 inHg to remove air bubbles caused during mixing. The mixture was slowly poured into the Aluminum mold to minimize air entrapment. The Aluminum mold was then placed in a vacuum chamber at 29 inHg up to 8 hours for additional degassing. Thereafter, the PDMS was cured at 65 ^{o}C for 12 hours and then removed from the mold.

The mechanical properties of the PDMS polymer were determined in a tensile testing machine (Instron, Inc, Norwood, MA) as described in detail in Chapter 2 [35]. This allowed us to create a library of PDMS mixing ratios of predictable Young's modulus. The value of the elastic modulus of the PDMS material relating to physiological arterial pressure was determined from the stress-strain curve for pressures between 60 mmHg and 160 mmHg.

The phantom models consisted of a straight tube with a wall thickness of 1.5 mm, 26.4 mm inside diameter and an overall length of 300 mm. The drawings for the mold design of this model can be seen in Appendix A (A.8 Acute Dissection mold: Base 7 - sheet 1 of 2, A.9 Acute Dissection mold: Base 7 - sheet 2 of 2, 3.2.10 Acute Dissection mold: Base 8 - sheet 1 of 2, 3.2.11 Acute Dissection mold: Base 8 - sheet 2 of 2, A.16 Acute Dissection mold: Cap 2 - sheet 1 of 1). This mold is also designed for casting the outer wall of the acute dissection test section.

3.2.3 CT Imaging

Imaging was performed (Figure 3.2) using a 64-slice CT scanner (GE LightSpeed VCT 64-slice Scanner, GE Medical System, Milwaukee, WI), with retrospective ECG-gating. Scans were performed on the three different phantom models of mixing ratio 6:1, 8:1 and 9:1 and at heart rates of 40, 50 and 60 bpm for each model (n=9 total). De-ionized water was utilized in the flow loop; Iopamidol 370 was injected into the flow loop during the scan to enhance contrast between the phantom model and the surrounding air. There is 40 mm of anatomical coverage per rotation with 64 slices at 0.625 mm thickness, producing a high-resolution 3D view. With 0.625 mm width per each detector row, imaging is isotropic (isotropic voxels) since the height and length of the detectors is also approximately 0.625 mm in the x- and y- axes of the detectors. This allows sub-millimeter spatial resolution. The scan parameters were as follows: 250 mm dedicated field of view (DFOV), pitch for a heart rate of 45 was 0.2, detector collimation of 64 x 0.625 mm (with ECG-gating), and a gantry rotation time of 0.4 second. A standard kernel and partial reconstruction algorithm with 270 degrees of data was used.

The raw data was then reconstructed in a 98 mm field of view with a 512 x 512 pixel matrix to improve image resolution. CT images, were reconstructed to correspond to each 5% of the R-R interval for phases 0% to 95% and had a section thickness of 1.25 mm. Images (see Figure 3.3) were reviewed on an Advantages Workstation version 4.4 (GE Healthcare, Milwaukee, WI) to determine maximum and minimum aortic distensibility. The displayed field of view will have a maximum of 250 mm and 512 x 512 pixels and the resolution of each monitor pixel will be 0.5 mm or less. Therefore, monitor resolution was equivalent to or better than the spatial resolution of the original data (i.e. the monitor did not significantly reduce overall resolution).

3.2.4 CT Post-Processing Technique

Advanced Vessel Analysis software (GE Healthcare, Milwaukee, Wis.) for the Advantage Windows workstation was used to generate the measurements. It is an integrated post-processing image analysis software technique for the application of cardiovascular imaging. It provides semi-automated analysis tools that allow the user to track, extract, visualize and measure blood vessels such as the aorta. Short axis, cross-sectional, long axis, and rotating curved views of the phantom are provided allowing accurate measurements to be made of the aortic diameter and cross-sectional area. The software initially generates a 3D model and long-axis reformatted image of the phantom. The user then identifies predetermined anatomical points along the phantom and the software generates minimum, maximum and mean aortic diameter measurements.

Optimum results are obtained in 3D imaging when the inter-slice distance is the same in all three axes resulting in isotropic voxels. Our study was performed with isotropic voxels. The software calculates and displays measurements with a resolution of one decimal place (i.e. 0.1 mm). Geometrical accuracy is limited by display resolution or pixel size. The geometrical accuracy of measurements performed with the Vessel Analysis software, when related to vessel measurements, is valid if the vessel diameter is larger than 2 mm. When the four views are displayed, each view is 512 x 512 pixels, hence with a display field of view (DFOV) of 25 cm a pixel is equivalent to 0.5 x 0.5 mm. Our study was performed with DFOV of 98 mm. The geometrical accuracy for a distance measurement is equal to the displayed length ± image pixel size. The geometrical accuracy defines a lower bound on the overall accuracy that can be obtained. The image set resolution is determined by the size of the field-of-view, the matrix size and the inter-slice distance. In the acquisition plane, for a field-of-view of about 98 mm, the smallest detail in an image acquired with a 512 x 512 matrix will be approximately 0.2 x 0.2 mm. The measurement accuracy can obviously not be better than the size of the smallest element. In the same way, the accuracy in a direction perpendicular to the acquisition plane cannot be better than the inter-slice distance. The center line created during the vessel tracking analysis is automatic and will be the same each time the image data set is opened. Therefore, the only variability in the distance measurement is due to where the user deposits the two points for the measurements. The distance along the center line is calculated by the nearest voxel associated with the point where the operator deposits the cursor. The 0.1 mm is more relevant to the measurements in question. So, with this accuracy of the curvilinear measures and the fact that the center line is created the same each time, the accuracy should be 0.1 mm.

3.3 Results

GE software was used to determine the dynamic changes of the area in each phantom model. Figure 3.4, Figure 3.5 and Figure 3.6 shows the temporal variation of the area at three locations of the phantom models of mixing ratio 6:1, 8:1 and 9:1 respectively, for heart rates of 40, 50 and 60 bpm. The calculation of the elasticity of the phantom model was estimated using the changes in the cross-sectional area of the phantom at min/max pressures within a cardiac cycle and applying them in Equation 3-1. Table 3.1 shows a comparison between the elasticity determined from the phantom models to those of the tensile testing machine. As the heart rate was increased in the phantom models the strain rate is of course increased as well. The elasticity values increase for a given mixing ratio as the strain rate increases exhibiting viscoelastic behavior (For 6:1 - 103.3% increase from 40 bpm to 50 bpm and 103.72% increase from 50 bpm to 60 bpm. 101.03% and 101.02% for 8:1, 40 to 50 bpm and 50 to 60 bpm, respectively. 104.76% and 120.83% for 9:1, 40 to 50 bpm and 50 to 60 bpm, respectively). Figure 3.7 shows a typical hysteresis loop formed when comparing the diameter change as related to pressure in a viscoelastic material. Although Table 3.1 shows good correlation comparing the CT data for 40 bpm to tensile testing machine data at a strain rate of 500 mm/min (relative error: 13.75%, 11.01% and 1.2%, for 6:1, 8:1 and 9:1 respectively), further studies should be done with higher strain rates in the physiogical range.

Computational methods have become powerful and popular tools in investigating vascular diseases which are influenced by hemodynamic factors. The accuracy and reliability of computational dynamic fluid-structure interaction (FSI) models can be established by comparison with experimental and clinical data. We embedded the elasticity values we measured in the aortic phantom model in a numerical model (Adina R&D Inc.) of the descending aorta to correlate the changes we observed in the CT with those that would be predicted by the numerical model. The numerical model, based on finite element formulation, was used to solve for fluid flow and structure dynamics in test sections utilizing the same velocity and pressure waveforms recorded in the CT scan experiment. Figure 3.8 shows the temporal variation of the area in a numerical model compared to the area of the phantom model obtained by the CT scanner. Good agreement is found between both sets of results. These findings suggest that the measurement of elastic value in the phantom model by ECG-gated multidetector CT angiographic protocol is promising. Also, the results suggest that computational models are capable of accurately capturing the mechanics of a functioning aorta.

3.4 Discussion

Vascular diseases are associated, through cause or effect, with changes in the mechanical properties of the arterial wall. Published studies on the mechanical properties of the arterial wall in humans have been conducted by testing strips of arteries obtained from surgical specimens or autopsies. The measurements of elasticity in these aortic strips have been conducted uni-axially, corresponding to either the circumferential or longitudinal direction. We acknowledge that the elastic properties of the aorta are anisotropic and that *in-vivo* stresses, being both radial and longitudinal should ideally be performed in a bi-axial testing machine with biaxial strain imposed on the aortic tissue simultaneously.

Imaging technologies allow us to see and measure the motion of the living and functioning vascular wall *in-vivo*. The arterial wall motion of a functioning aorta is a signal reflection of its mechanical properties. Among vascular imaging technologies, ultrasound is the one most widely available because of its relatively low cost. Ultrasound imaging of vascular anatomy, though commonly used in the clinic, has yet to play a significant role in image-based computational fluid dynamics or mechanical analysis. This is because the two-dimensional ultrasound images are acquired manually without reference to a fixed coordinate system, making it impossible to reconstruct a scanned artery in three-dimensions. In addition, the quality of aortic images obtained by transcutaneous ultrasound is affected by the surrounding anatomic structures (lungs and ribs for the thoracic aorta, or bowels and fat for the abdominal aorta).

Intravascular ultrasound (IVUS) imaging is a catheter based system that allows acquisition of vessel images from inside their lumen. IVUS can provide measurements of lumen and vessel size, plaque area and volume. However, it is invasive and the overall vessel structure and geometry cannot be reproduced accurately using the current available catheter pullback withdrawal systems because, similar to transcutaneous ultrasound, the IVUS probe is not related to a fixed reference coordinate system [36]. In addition, tortuous vessels are not well demonstrated by IVUS where their reconstruction may appear as a straight cylinder. This will introduce errors in diameter measurements, possibly overestimating it when the probe is not in the axis of the vessel [37]. Magnetic resonance imaging (MRI) has also been used to determine arterial wall dimensions and motion. However, its limited availability and high cost make MRI less attractive.

The definition of aortic geometry is made today with CT scanners. Newer 64-slice CT scanners have much improved spatial and temporal resolution resulting in a high-resolution 3D view of the patient's anatomy. These high resolution images of a pulsating human aorta permit us to estimate the mechanical properties of a living aorta.

3.5 Conclusions

An aortic phantom may be scanned with standard CTA aortic protocols and, from the geometry data embedded in its DICOM files, the value of the Young's modulus of elasticity of this phantom may be derived. We have calculated the elastic parameters of a functioning aortic phantom model using CTA data. We have shown the correlation found between this set of CT-derived data, the direct measurements of PDMS used in the phantom aortic wall on a tensile testing machine and the data predicted by fluid-solid interface computational modeling. We continue to explore the possibility of measuring changes in arterial dimensions by CTA in patients with aortic dissections and aortic aneurysms.

From this data we may derive the mechanical properties of the aortic wall. Accurate and fast calculation of the physical properties of aortic tissues will allow better assessment of the risk of rupture of an aortic dissection or aneurysm.

Table 3.1 Comparison of the Young's modulus calculation between CT experiment and the tensile testing of a PDMS material of known elasticity

Ratio	CT Experiment	Tensile Testing Machine (500 mm/min)
6:1 (40 bpm)	1.82 MPa	1.6 MPa
6:1 (50 bpm)	1.88 MPa	
6:1 (60 bpm)	1.95 MPa	
8:1 (40 bpm)	1.94 MPa	2.18 MPa
8:1 (50 bpm)	1.96 MPa	
8:1 (60 bpm)	1.98 MPa	
9:1 (40 bpm)	2.52 MPa	2.49 MPa
9:1 (50 bpm)	2.64 MPa	
9:1 (60 bpm)	3.19 MPa	

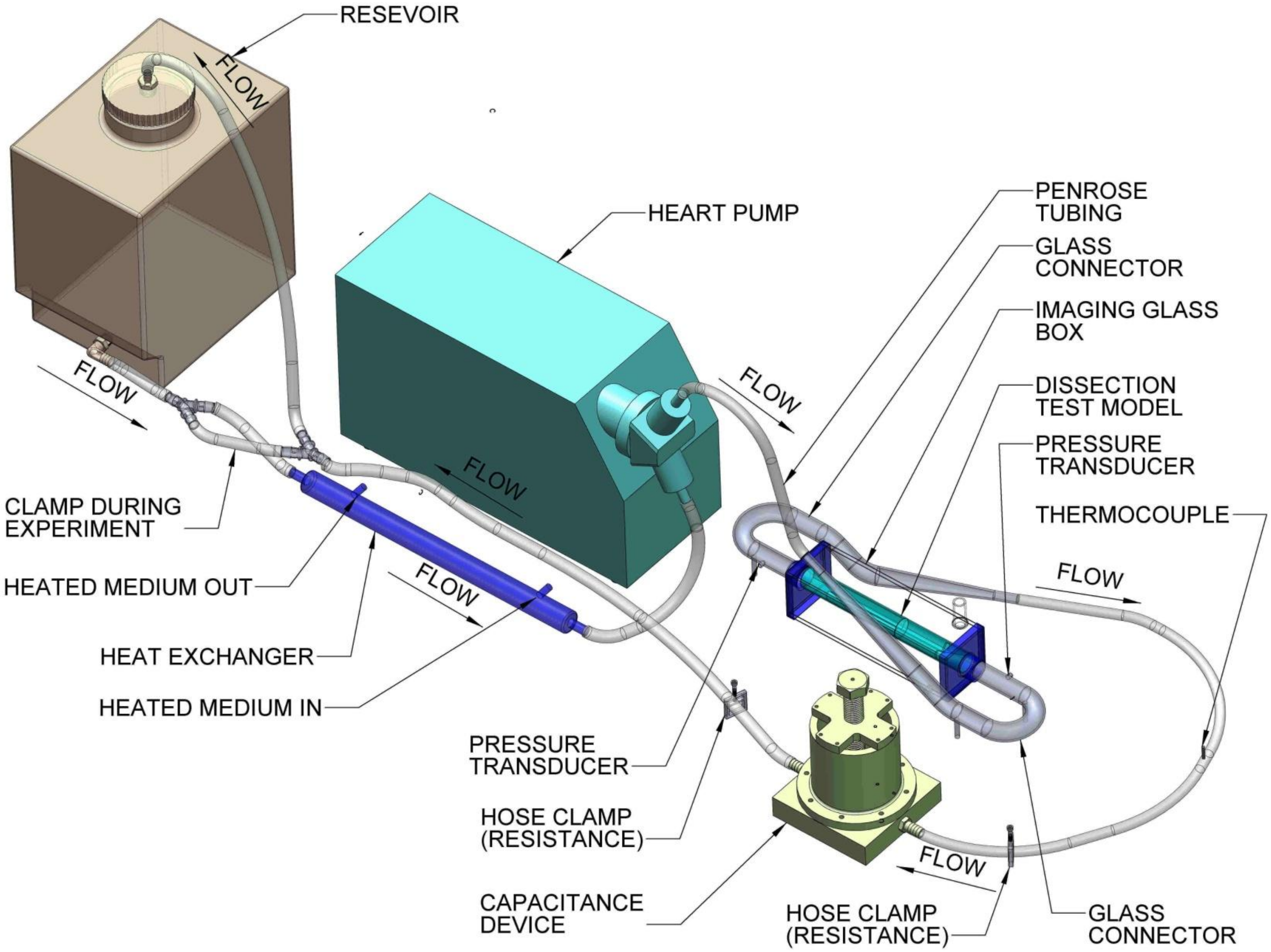

Figure 3.1 Bench top model schematic layout

Figure 3.2 Phantom Setup

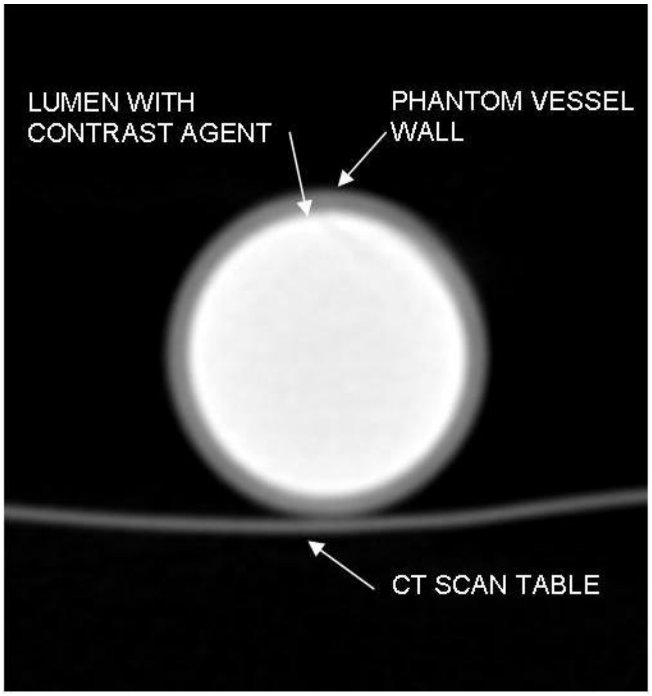

Figure 3.3 DICOM image of phantom model

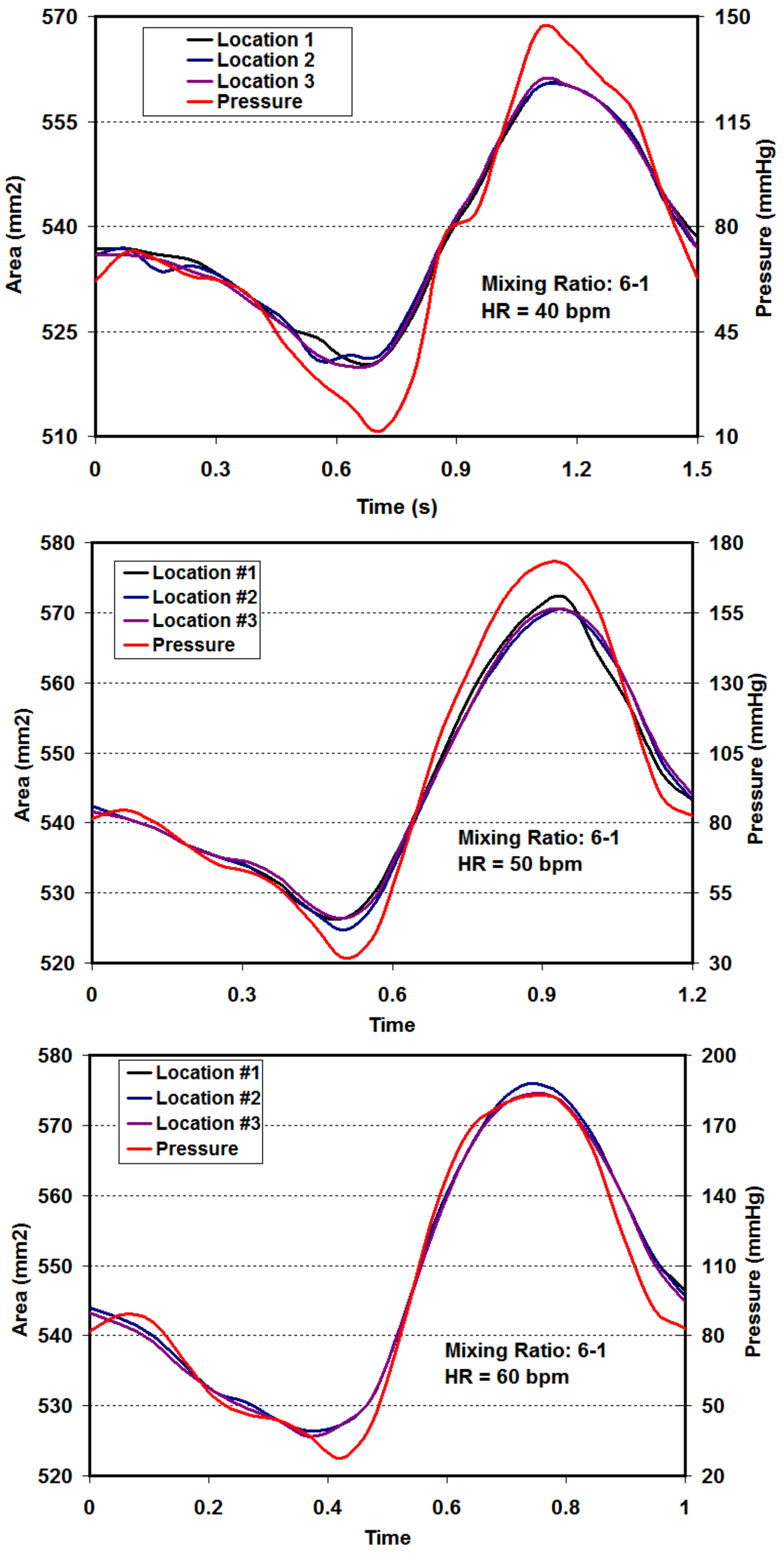

Figure 3.4 Comparison of the temporal variations of the test section area at three locations (Mixing ratio 6:1, heart rate 40, 50 and 60 BPM)

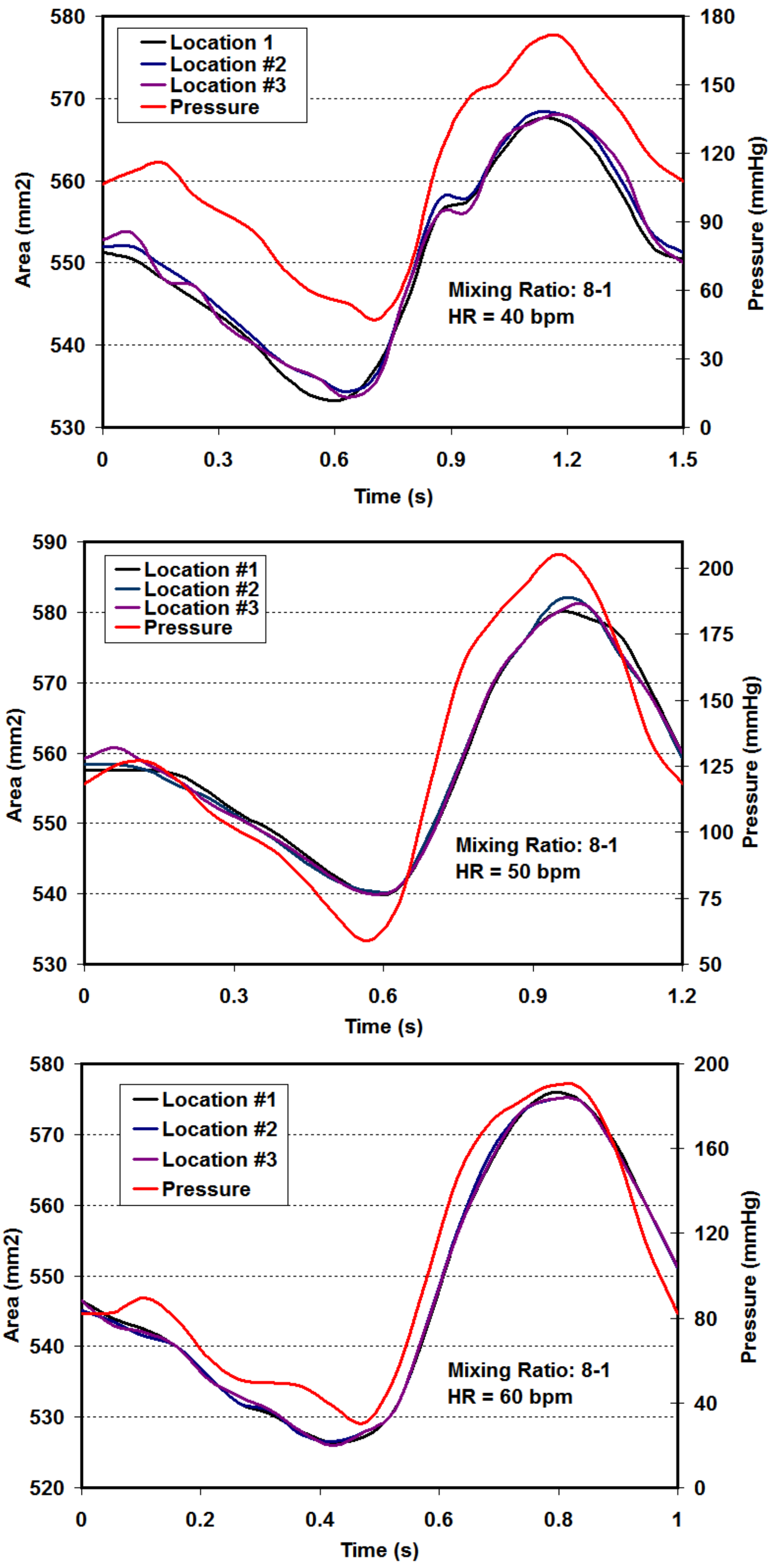

Figure 3.5 Comparison of the temporal variations of the test section area at three locations (Mixing ratio 8:1, heart rate 40, 50 and 60 BPM)

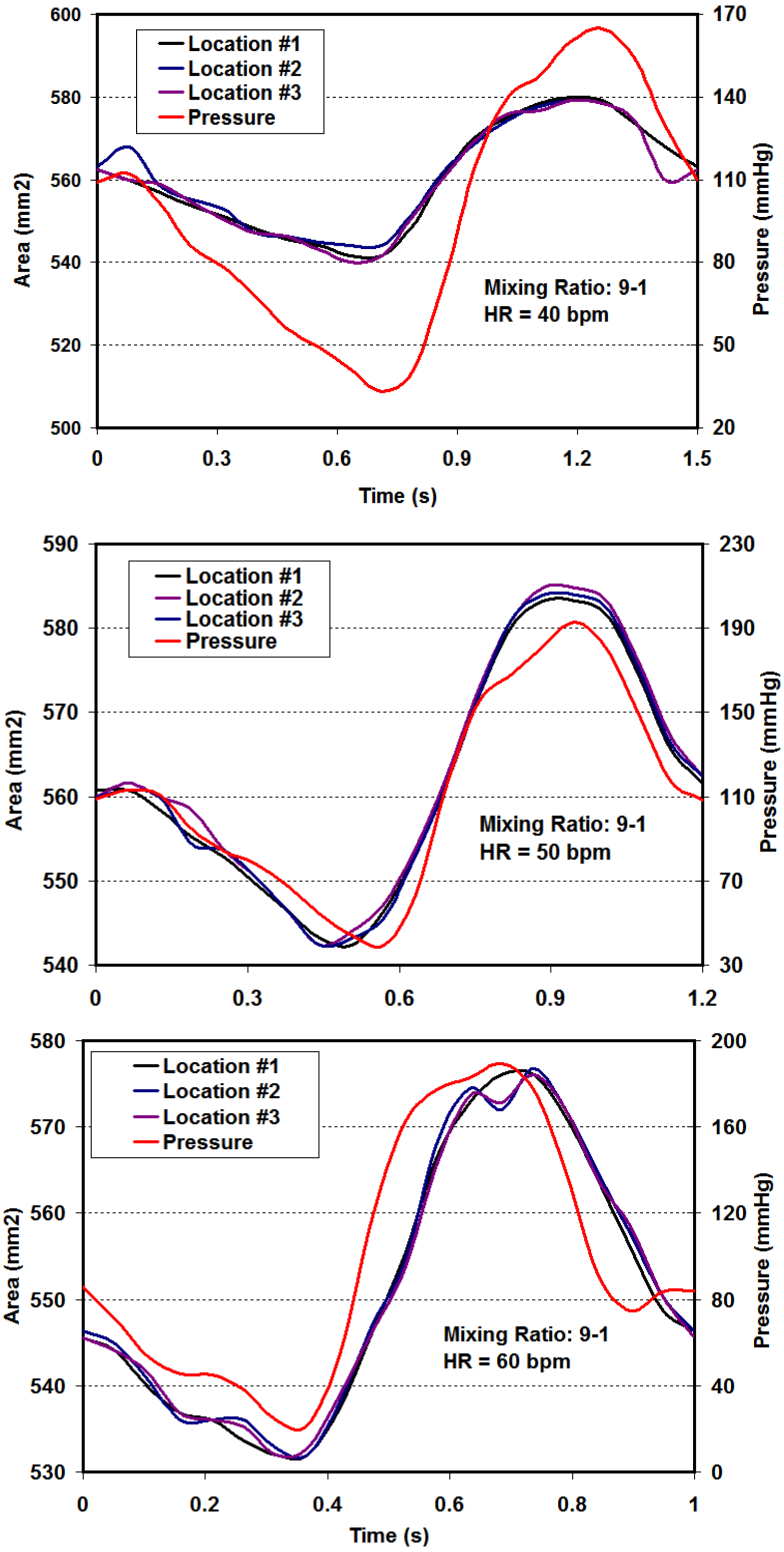

Figure 3.6 Comparison of the temporal variations of the test section area at three locations (Mixing ratio 9:1, heart rate 40, 50 and 60 BPM)

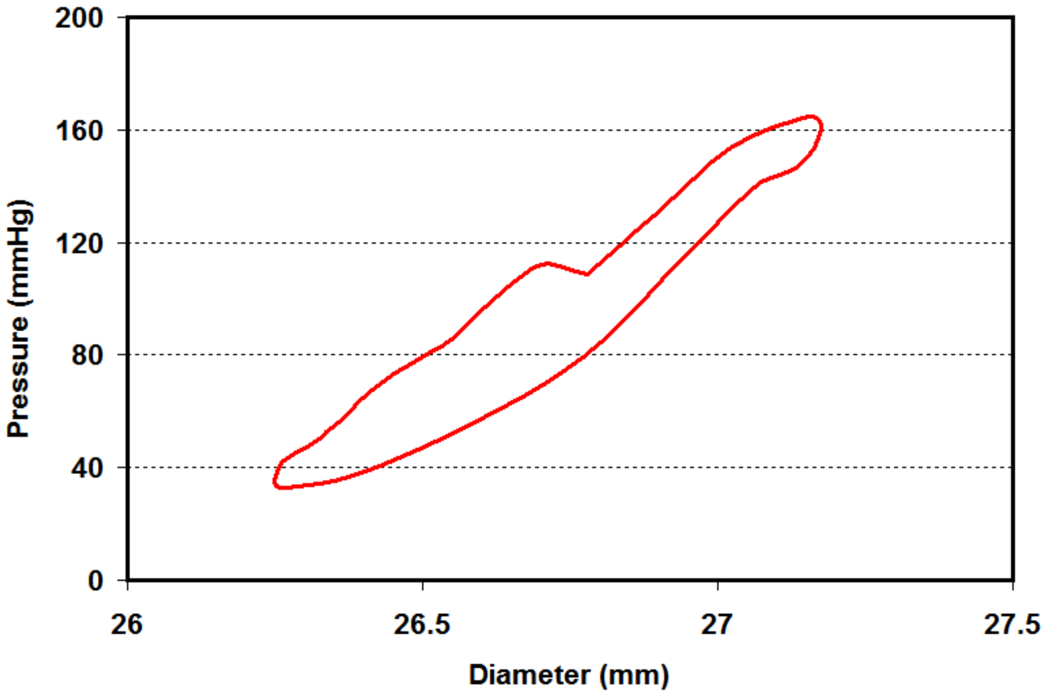

Figure 3.7 Representative hysteresis loop (Mixing ratio 9:1, heart rate 40 bpm)

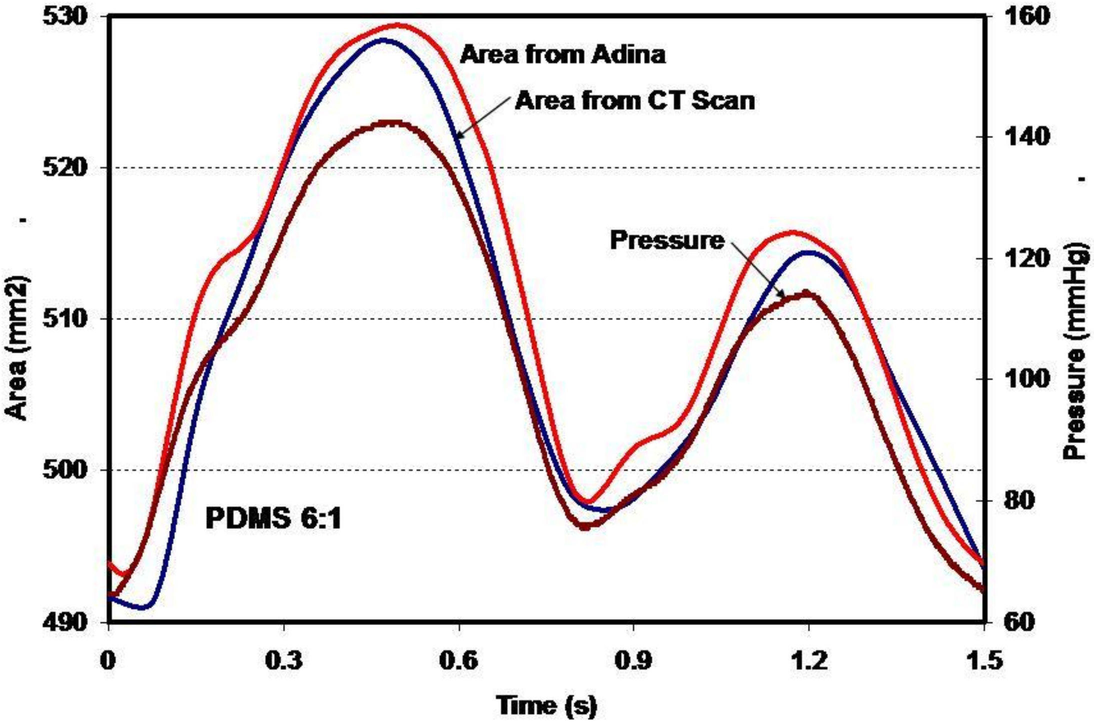

Figure 3.8 Comparison of the temporal variations of the test section area between CT scan experiment and the numerical method (Mixing ratio 6:1, heart rate 40 bpm)

3.6 References

[1] L. Xue and H. P. Greisler, "Biomaterials in the development and future of vascular grafts," *Journal of Vascular Surgery,* vol. 37, pp. 472-480, Feb 2003.

[2] R. Y. Kannan*, et al.*, "The roles of tissue engineering and vascularisation in the development of micro-vascular networks: a review," *Biomaterials,* vol. 26, pp. 1857-1875, May 2005.

[3] J. Yang*, et al.*, "Synthesis and evaluation of poly(diol citrate) biodegradable elastomers," *Biomaterials,* vol. 27, pp. 1889-1898, Mar 2006.

[4] G. S. Kassab and J. A. Navia, "Biomechanical considerations in the design of graft: The homeostasis hypothesis," *Annual Review of Biomedical Engineering,* vol. 8, pp. 499-535, 2006.

[5] D. H. Bergel, "Static Elastic Properties of Arterial Wall," *Journal of Physiology-London,* vol. 156, pp. 445-457, 1961.

[6] P. B. Dobrin, "Mechanical-Properties of Arteries," *Physiological Reviews,* vol. 58, pp. 397-460, 1978.

[7] K. B. Chandran and M. J. Vonesh, "The role of mechanics in vascular biology," in *Non-invasive imaging of atherosclerosis*, M. D. Mercuri M, Bassiuony H, et al, Ed., ed: Kluwer Academic Publishers, 1998, pp. 130 – 168.

[8] C. J. Chuong and Y. C. Fung, "Three-dimensional stress distribution in arteries," *J Biomech Eng,* vol. 105, pp. 268-74, Aug 1983.

[9] R. H. Cox, "Comparison of Carotid-Artery Mechanics in Rat, Rabbit, and Dog," *American Journal of Physiology,* vol. 234, pp. H280-H288, 1978.

[10] P. B. Dobrin and R. Mrkvicka, "Estimating the elastic modulus of non-atherosclerotic elastic arteries," *J Hypertens Suppl,* vol. 10, pp. S7-10, Aug 1992.

[11] Y. C. Fung, *Biomechanics: Mechanical properties of living tissues*, Second ed. New York: Springer-Verlag, 1993.

[12] B. S. Gow and C. D. Hadfield, "Elasticity of Canine and Human Coronary-Arteries with Reference to Postmortem Changes," *Circulation Research,* vol. 45, pp. 588-594, 1979.

[13] A. Zanchi*, et al.*, "Differences in the mechanical properties of the rat carotid artery in vivo, in situ, and in vitro," *Hypertension,* vol. 32, pp. 180-185, Jul 1998.

[14] W. D. Coats, Jr.*, et al.*, "Remodelling and restenosis: insights from animal studies," *Semin Interv Cardiol,* vol. 2, pp. 153-8, Sep 1997.

[15] D. R. Gross*, et al.*, "Pressure-Diameter Relationships in the Coronary-Artery of Intact, Awake Calves," *Journal of Biomechanics,* vol. 14, pp. 613-620, 1981.

[16] R. S. Schwartz*, et al.*, "Differential neointimal response to coronary artery injury in pigs and dogs. Implications for restenosis models," *Arterioscler Thromb,* vol. 14, pp. 395-400, Mar 1994.

[17] P. R. Hoskins, "Physical properties of tissues relevant to arterial ultrasound imaging and blood velocity measurement," *Ultrasound Med Biol,* vol. 33, pp. 1527-39, Oct 2007.

[18] J. Dineley*, et al.*, "Design and characterisation of a wall motion phantom," *Ultrasound Med Biol,* vol. 32, pp. 1349-57, Sep 2006.

[19] A. Long*, et al.*, "Compliance of abdominal aortic aneurysms: evaluation of tissue Doppler imaging," *Ultrasound Med Biol,* vol. 30, pp. 1099-108, Sep 2004.

[20] F. Hansen*, et al.*, "Diameter and compliance in the human common carotid artery--variations with age and sex," *Ultrasound Med Biol,* vol. 21, pp. 1-9, 1995.

[21] O. Bonnefous*, et al.*, "New TDI developments for vascular and cardiac applications," presented at the IEEE Ultrasonic Symposium, 2000.

[22] O. Bonnefous*, et al.*, "Non invasive echographic techniques for arterial wall characterization," presented at the IEEE Ultrasonic Symposium, 1996.

[23] A. J. Luik*, et al.*, "Arterial compliance in patients on long-treatment-time dialysis," *Nephrol Dial Transplant,* vol. 12, pp. 2629-32, Dec 1997.

[24] A. Eriksson*, et al.*, "Arterial pulse wave velocity with tissue Doppler imaging," *Ultrasound Med Biol,* vol. 28, pp. 571-80, May 2002.

[25] M. O'Donnell*, et al.*, "Measurement of arterial wall motion using Fourier based speckle tracking algorithm," presented at the Ultrasonics Symposium, 1991.

[26] M. A. Lubinski*, et al.*, "Speckle tracking methods for ultrasonic elasticity imaging using short-time correlation," *IEEE Trans Ultrason Ferroelectr Freq Control,* vol. 46, pp. 82-96, 1999.

[27] B. Shapo*, et al.*, "Ultrasonic displacement and strain imaging of coronary arteries with a catheter array," presented at the IEEE Ultrasonics Symposium, 1995.

[28] M. Kachelriess*, et al.*, "ECG-correlated image reconstruction from subsecond multi-slice spiral CT scans of the heart," *Med Phys,* vol. 27, pp. 1881-902, Aug 2000.

[29] J. M. Boese*, et al.*, "[Optimizing temporal resolution in CT with retrospective ECG gating]," *Radiologe,* vol. 40, pp. 123-9, Feb 2000.

[30] M. Bahner*, et al.*, "Spiral CT of the heart with retrospective ECG-gating," presented at the Electromedica, 1999.

[31] M. Ganten*, et al.*, "Quantification of aortic elasticity: development and experimental validation of a method using computed tomography," *Eur Radiol,* vol. 15, pp. 2506-12, Dec 2005.

[32] J. Zhang*, et al.*, "Large-vessel distensibility measurement with electrocardiographically gated multidetector CT: phantom study and initial experience," *Radiology,* vol. 245, pp. 258-66, Oct 2007.

[33] M. K. Ganten*, et al.*, "Quantification of aortic distensibility in abdominal aortic aneurysm using ECG-gated multi-detector computed tomography," *Eur Radiol,* vol. 18, pp. 966-73, May 2008.

[34] M.-K. Ganten*, et al.*, "Motion characterization of aortic wall and intimal flap by ECG-gated CT in patients with chronic B-dissection," *European journal of radiology,* vol. 72, pp. 146-153, 2009.

[35] K. Khanafer*, et al.*, "Effects of strain rate, mixing ratio, and stress-strain definition on the mechanical behavior of the polydimethylsiloxane (PDMS) material as related to its biological applications," *Biomed Microdevices,* Dec 5 2008.

[36] D. A. Steinman, "Image-based computational fluid dynamics modeling in realistic arterial geometries," Ann Biomed Eng, vol. 30, pp. 483-97, Apr 2002.

[37] D. B. Reid, et al., "The clinical value of three-dimensional intravascular ultrasound imaging," J Endovasc Surg, vol. 2, pp. 356-64, Nov 1995.

Chapter 4

Ex-Vivo Model of Chronic and Acute Aortic Dissection

4.1 Introduction

Imaging studies suggest that complete thrombosis of the false lumen has beneficial prognostic value while a patent or, open false lumen predicts poor outcomes [1-3]. Partial thrombosis of the false lumen, defined by the presence of both flow and thrombus was recently found to be associated with a 2.7 fold increased risk of death compared to patients with a patent false lumen [4].

Previous clinical anecdotes and phantom models of acute aortic dissection have shown that distal tears between the true and false lumen downstream to a proximal intimal tear, may help prevent true lumen collapse and the risk of malperfusion syndromes during the acute dissection [5-7]. A similar mechanism of risk may exist in patients with partial thrombosis of the false lumen in the chronic phase. An obstruction by thrombus of a previously patent distal tear may impair outflow resulting in an elevated diastolic pressure compared to a patient with a distal tear. Furthermore, in patients who receive aortic stent grafts covering the proximal tear, remaining uncovered distal tears may also result in an elevated diastolic pressure compared to a patient with an uncovered proximal tear (Figure 4.1) [8, 9].

We hypothesized that determinants of inflow and outflow, such as the size and location of intimal tears, can significantly increase the pressure within the false lumen of patients with Stanford Type B aortic dissection. The aim of this study was to assess the pressure changes within the false lumen after simulated changes in tear size, tear number and tear location in an ex-vivo model of chronic aortic dissection [10]. And develop an ex-vivo model of acute aortic dissection with realistic geometries and more physiological relevant mechanical properties of the vessel walls and intimal flap.

4.2 Experimental Methods

Polydimethylsiloxane (PDMS) was used to create compliant models of chronic and acute dissections of human aortas. These models were then used in a bench-top flow loop described in Section 3.2.1 to study flow characteristics and wall movement.

4.2.1 Chronic Dissection Model

An aluminum mold was designed and fabricated to create a compliant dissection model mimicking a chronic type B aortic dissection with 50% of the circumference dissected. The dimensions of the dissection model were selected to approximate the anatomical measurements of aortic dissections obtained from human clinical and pathologic studies. The dimensions were: aortic diameter = 40 mm, aortic length = 340 mm, true lumen wall thickness = 3 mm, dissection flap thickness = 2 mm and false lumen thickness 1 mm (Figure 4.2) [11-13]. This model simulates a chronic dissection with a dissection flap that is taught and stiff similar to the fibrosed flaps described on cross sectional imaging [2, 14]. A glass arch with a diameter of 30 mm was used to divert the flow just prior to the connection with the dissection model as is seen anatomically.

PDMS (Sylgard 184, Dow Corning Corp, Midland, MI) prepolymer (A: base) and cross-linker (B: curing agent) were mixed at a ratio of 6:1 (ratio of A : B), poured into the mold, degassed at 25 inHg, and cured in an oven at 60 ± 3°C for 18 hours. The PDMS was cooled and carefully removed from the mold. One side port on the false lumen was cannulated with a 6 French sheath (St. Jude Medical, St. Paul, Minn) to measure false lumen pressures. The true lumen pressures were measured from the proximal aortic arch. Holes mimicking the size of anatomical tears between the true and false lumen, as imaged on computed tomography in humans, were simulated using 6.4 mm and 3.2 mm diameter punched holes [14]. The proximal hole was made distal to the connection at the glass arch simulating the common tear location just distal to the branch of the left subclavian artery in humans [15]. The distal hole was placed 240 mm downstream from the proximal hole.

4.2.1.1 Flow dynamics

The perfusion fluid used was a Doppler Test Fluid, Model 707 (ATS Laboratories Inc, Bridgeport, CT.) formulated to mimic the physical properties of human blood; it was warmed to 37°C. Pressures were measured in the true and false lumen with a pressure transducer (AD Instruments, Model MLT-3018, Colorado Springs, CO) and recorded with Labview software (National

Instruments Inc, Austin, TX.) (See Appendix B, B.1 – Labview front panel, B.2 – Labview block diagram). The area under the pressure waveforms were used to calculate mean pressures. Heart rate and peripheral resistance were varied for different simulations and stroke volume was maintained at 60 ml/stroke with a fixed diastolic/systolic phase ratio of 60/40. Systemic pressure was varied from 93/44 mmHg to 198/171 by adjusting the resistance and the heart rate. With changes in heart rate of between 40-80 beats per minute, flow rates of 1.6 to 3.7 L/min and peripheral resistance of 1200 to 3113 dyne-s/cm^5 were achieved.

4.2.1.2 Model simulations

Multiple simulations were performed in each dissection model varying heart rate and peripheral resistance. Each dissection model was subjected to 5 different heart rates (40, 50, 60, 70 and 80 beats per minute) and corresponding pressure waveforms were recorded. Pressure values reported represent an average of 10 cycles after hemodynamic conditions were at steady state. To compare false lumen diastolic pressure between models, a False lumen Pressure Index (FPI%) was calculated for all simulations as FPI% = (false lumen diastolic pressure/true lumen diastolic pressure) X 100.

4.2.1.3 Statistical analysis

Continuous variables were expressed as the mean ± SD. The Wilcoxon rank sum test was used to analyze simulation means of the systolic, diastolic, mean, and normalized pressures both within and between dissection models. Linear regression was used to test for an association between heart rate and diastolic pressure in the false lumen.

4.2.2 Acute Dissection Model

An aluminum mold was also designed and fabricated to create a compliant dissection model mimicking an acute type B aortic dissection with 50% of the circumference dissected. The mold design for the outer wall of the model can be seen in Appendix A, (A.8 Acute Dissection mold: Base 7 - sheet 1 of 2, A.9 Acute Dissection mold: Base 7 - sheet 2 of 2, 4.2.10 Acute Dissection mold: Base 8 - sheet 1 of 2, 4.2.11 Acute Dissection mold: Base 8 - sheet 2 of 2, A.16 Acute Dissection mold: Cap 2 - sheet 1 of 1). The mold design for the inner wall (intimal flap) of the model can be seen in Appendix A, (A.12 Acute Dissection mold: Base 9 - sheet 1 of 2, A.13 Acute Dissection mold: Base 9 - sheet 2 of 2, 4.2.14 Acute Dissection mold: Base 10 - sheet 1 of 2, 4.2.15 Acute Dissection mold: Base 10 - sheet 2 of 2, A.17 Acute Dissection mold: Cap 3 - sheet 1 of 1). These two mold sets produce an inner (intimal flap) and outer wall tube that can be cast with different mixed ratios of PDMS.

PDMS prepolymer (A: base) and cross-linker (B: curing agent) were mixed at a ratio of 9:1 (ratio of A : B) for the outer wall and a more compliant mixing ratio of 20:1 for the inner wall. After thoroughly mixing it was placed in a vacuum chamber and degassed at 25 inHg until it was absent of bubbles. It was then slowly poured into the mold base and degassed at 29 inHg for two hours before inserting the lumen (rod) mold. The cap was placed loosely on top of the base mold after inserting the rod and held in position with four bolts but, the cap was held elevated above the base with two jam bolts to allow bubbles to escape. The mold was then degassed at 29 inHg for an additional 8 hours before being placed in an oven and cured at 65°C for 12 hours. If needed, additional PDMS was added to top off the mold prior to placing in the oven.

After cooling, the molds are placed in a bath containing dish soap to facilitate careful removal of the tubes from the molds. Once removed from the mold, the tubes are cleaned with a wash of acetone, then isopropyl alcohol and finally with de-ionized water. The inner tube is then carefully placed inside the outer tube. A mixture of PDMS at a ratio of 2:1 that will act as a bonding agent is prepared and degassed. This bonding agent is loaded into a 10mm syringe that is attached to a 5 French catheter which is placed in between the inner and outer wall tubes. The bonding agent is slowly dispensed in between the tubes as the catheter is slowly pulled down the length. A halved section (lengthwise) of 1/8” thick x 1” O.D. Teflon tube is placed inside the inner tube and then held in place with a 3/8” x 1/2” thick stainless steel bar clamped to one of the base molds. This is then placed in the oven at 65°C for 18 hours to bond the tubes together leaving a 180° dissection un-bonded.

Once cooled, the model may be removed from clamping and tears may be cut into the flap. The dimensions of the completed model are detailed in Figure 4.3. The true lumen wall now consists of the inner and outer tube bonded together; the overall thickness is 2.25 mm. The outer wall of the false lumen, which was the outer tube, is 1.25 mm thick. And the intimal flap, which was the inner tube, is 0.75 mm thick. The overall length of the model is 220 mm with tears both proximal and distal at 140 mm apart, 40 mm in from each end. The inside diameter of the true lumen is 24.9 mm, the inside diameter of the false lumen is 26.4 mm and outside diameter of the model is 29.4 mm. This model simulates an acute dissection with proximal and distal tears and a dissection flap that is flexible and moves similar to those seen in cross sectional imaging (Figure 4.4).

4.2.2.1 Ultrasound Imaging

Duplex ultrasonography was performed to evaluate the presence of acute aortic dissection model as shown in Figure 4.5. Doppler imaging was performed with a linear intraoperative multi-hertz (13-5 MHz) transducer and Siemens Sonoline Antares (Siemens Medical Solutions USA Inc, Mountain View, CA) unit. Images were obtained in the transverse and longitudinal plane, using color Doppler, spectral Doppler, and gray scale imaging. The fluid used in the flow loop is a Doppler Test Fluid, Model 707 (ATS Laboratories Inc, Bridgeport, CT) which contains a mixture of water and glycerin with small plastic particulates. The glycerin increases the viscosity of the fluid to match that of blood and the plastic particulates are sized to emulate red blood cells and other cells found in blood. It is the particulates that are picked up and recorded by the ultrasound device.

The model was housed in a glass imaging box as detailed in Appendix A (A.18 – Ultrasound imaging glass box). De-ionized water surrounded the model inside the imaging box to facilitate transmission of the sound waves. The ends of the imaging box were sealed with diaphragms made of Plasti Dip (Plasti Dip

International, Blaine, MN) that were dip-cast from molds shown in Appendix A, A.19 – Diaphragm mold – sheet 1 of 1.

4.2.2.2 Flow dynamics

Pressure was measured with a pressure transducer (AD Instruments, Model MLT-3018, Colorado Springs, CO) proximal and distal to the dissection model and recorded with Labview software (National Instruments Inc, Austin, TX.) (See Appendix B, B.1 – Labview front panel, B.2 – Labview block diagram). The heart rate was set at 60 bpm and stroke volume was maintained at 60 ml/stroke with a fixed diastolic/systolic phase ratio of 50/50. Figure 4.6 shows the waveform results for pressure and flow rate; systemic pressure was 210/60 mmHg with a flow rate of 0.5 to 5.5 L/min.

4.2.3 Mold Preparation

The finish on the aluminum molds for the dissection models is critical for successful removal of the test sections as well as maintaining optical clarity for image analysis. After machining the molds an appropriate abrasive level of steel wool was chosen to remove tooling marks. This choice may vary from one project to another depending on tool choice, stepping and head speed. Chose a level that will remove ridges left by tooling but, not too quickly. Once the marks are removed, continue with finer and finer grades of steel wool until you reach the 0000 level. Then using a Dremel tool with a small-diameter felt polishing wheel (medium-hard density, 1" diameter x 1/4" thick) apply lapping paste and polish the areas that will form the casting. Again use a finer and finer grit (i.e.

General purpose lapping paste - 1200 grit, corundum aluminum oxide, gray, then 3000 grit, corundum aluminum oxide, gray followed by general purpose lapping paste, chrome oxide alumina, green) until no marks or blemishes are visible in the reflection of the surface. Finally to remove any marks left by the felt polishing wheel, hand polish using a soft polishing cloth and optical-finish medium #1/4 white diamond polishing compound. To prevent the PDMS from adhering to the mold apply Zero Stick mold release (Stoner Inc., Quarryville, PA). Mineral Spirits may be used for cleaning the molds after casting, then rinse with Krud Kutter (Supreme Chemicals of GA Inc., Atlanta, GA) followed by 70% ethanol.

4.3 Results

4.3.1 Chronic Dissection Model

The baseline dissection model used a 6.4 mm proximal and 6.4 mm distal tear as commonly observed on spiral computed tomography in humans (Dissection Model A,Figure 4.7). Data on true lumen and false lumen pressure for the baseline dissection model A is shown in Table 4.1. The systolic blood pressure was slightly lower in the false lumen compared to the true lumen while the diastolic pressure was slightly higher in the false lumen. Within the false lumen, systolic pressure was 99.3% ± 0.13% of true lumen pressure and diastolic pressure was 100.4% ± 0.20% of true lumen pressure ($P<.001$). The mean arterial pressures were not significantly different.

4.3.1.1 Effect of size and location of tear on flow dynamics

In the absence of a distal tear (Dissection Model B**,**Figure 4.7), systolic pressure was significantly higher in the true lumen (111.29 mmHg ± 0.08) compared to the false lumen (105.76 mmHg ± 0.06, p < 0.001) with a mean difference of 5.5 ± 0.1 mmHg (Table 4.1). Diastolic pressure was elevated within the false lumen (58.95 ± 0.10) compared to the true lumen (54.66 ± 0.17, P<.001) with a mean difference of 4.4 mmHg ± 0.2. False lumen pressure index (FPI%) was higher in dissection model B compared to dissection model A (107.9% versus 100.4%, P<.001). There was an even greater effect on the difference in pressures in model B compared to model A with the smaller tear size (109.0% vs 105.0%, P<.001). In the absence of a distal tear, the waveform of false lumen pressure was dampened compared with true lumen pressure, with higher diastolic pressure but lower systolic pressure (Figure 4.8).

The absence of a proximal tear in the presence of a distal tear (Dissection Model C,Figure 4.7) also correlated with a significant decrease in systolic pressure in the false lumen and an elevation of diastolic pressure (Table 4.1). FPI% was significantly higher in dissection model C versus A (104.6% vs 100.4%, P<.001).

4.3.1.2 Effect of heart rate on flow dynamics with constant systolic pressure

In dissection model B (3.2 mm proximal tear only) the heart rate was adjusted in steps of 10 beats per minute while adjusting peripheral resistance to keep the systolic pressures similar. Increasing heart rate under these conditions resulted in a decrease in the difference between systolic pressure in the true and false lumen while the change in diastolic pressure between the true and false lumen increased (Table 4.2). Linear regression revealed that an incremental increase in heart rate by 10 beats per minute resulted in a diastolic pressure increase by 13.9% ($p<.001$, R^2 0.69) and a normalized diastolic percentage that increased by 1.3% ($p<.001$, R^2 0.72).

4.3.2 Acute Dissection Model

Ultrasound imaging was performed on the acute dissection model to observe intimal flap movement and flow dynamics. Figure 4.9 shows transverse views and corresponding longitudinal view with Doppler imaging in the presence of a proximal and distal tear. Images A & B show flow in both the true and false lumens prior to peak systole. As the flap is forced down further due to filling of the false lumen, images C & D, just after peak systole, show flow occluded in the true lumen. Images E & F, just prior to diastole, show a negative flow observed in the true lumen as the lumen begins re-filling from the distal tear. The flow rate then decreases going into diastole, reducing the pressure in the false lumen allowing the flap to lift.

4.4 Discussion

4.4.1 Chronic Dissection Model

Our study reveals differences in hemodynamic pressures within the true and false lumen in models of chronic type B aortic dissection which simulate different anatomic configurations of tear size, number and location. The absence of a proximal tear is associated with a significant decrease in systolic pressure within the false lumen presumably due to impairment of inflow from the true to false lumen. The lack of a distal tear results in a significant increase in diastolic pressure presumably due to an impairment of outflow from the false lumen to the true lumen. The extent of the decrease in systolic pressure and increase in diastolic pressure in the false lumen is proportional to the tear size. With a 50% decrease in tear diameter both proximally and distally, false lumen systolic pressure further decreased while diastolic pressure increased.

Among the dissection models tested, the absence of a distal tear was associated with the largest incremental increase in false lumen diastolic pressure, between 4-9% greater than true lumen diastolic pressure within each dissection model. Further, false lumen diastolic pressure as a percentage of true lumen diastolic pressure (false lumen pressure index) in dissection model B (without a distal tear) was consistently higher than diastolic pressure in dissection model A (with a distal tear) (107.9% vs 100.4%, P<.001). The blind end of the false lumen impairs outflow of the blood that enters during systole which results in an increased diastolic pressure and the dampened waveform that was observed. A similar but blunted phenomenon is also observed when the proximal tear is occluded in the presence of a patent distal tear.

Additionally, we showed that in the absence of a distal tear (Table 4.2), increases in heart rate lead to increased false lumen diastolic pressure independent of systolic pressure in the true lumen. Here, we suspect that as heart rate increases and diastolic filling time decreases, a decreased outflow from the false lumen occurs before the next systolic cycle promoting a further increase in diastolic pressure in the false lumen.

Mean arterial pressure is consistently lower in the false lumen despite an increase in the diastolic pressure. This likely reflects the related decrease in systolic pressure. La Place’s law states that the wall stress of an artery is proportional to the radial and intraluminal pressure and inversely proportional to wall thickness. Therefore, the increase in pressure, which occurs during the longer diastolic phase, will increase wall tension over a longer period of the cardiac cycle and may increase the risk of expansion and rupture.

4.4.2 Acute Dissection Model

Our study reveals flap movement and flow occlusion within the true lumen in a model of acute type B aortic dissection. During systolic phase, the proximal tear acts as an entry tear and the fluid flows through both lumens. As the false lumen fills with fluid during the acceleration phase, the intimal flap is pushed down towards the true lumen. At peak systole, the true lumen is occluded as shown in Figure 4.9-D. Following peak systole, as the flow decelerates the intimal flap begins to move towards the false lumen wall as the fluid empties from the false lumen. The direction of the flow is reversed, exhibiting a negative flow condition, and consequently the flap progresses further towards the false lumen. This is depicted in Figure 4.9-F. Figure 4.9-B shows an interesting effect which is associated with pressure in both lumens. The true lumen exhibits higher pressure than the false lumen during negative flow condition. Moreover, negative flow is observed in the false lumen through the distal tear during the negative flow condition.

This experiment of acute dissection model was conducted with a heart rate of 60 beats per minute. Considerable noise was experienced in the ultrasound imaging due to turbulence at higher rates. However, patients presented with this disease characteristically will have a higher heart rate. The flow rate and pressure during diastole may still be in the range experienced during our analysis but, the diastolic phase will be shorter. Further studies with bench-top models at higher rates may show that the intimal flap will have less time to return to its native position.

4.5 Conclusions

Follow-up mortality in patients with acute type B aortic dissection is high, approaching 1 in every 4 patients at 3 years [16] and current surveillance and treatment strategies appear to be inadequate. Cross sectional imaging during the follow-up period focuses on the diameter of the post-dissection aneurysm whose indications for operative intervention are similar to those of other thoraco-abdominal aneurysms [17]. Better predictors of false lumen expansion and dissection-related morbidity and mortality are needed. This study provides experimental evidence that the false lumen diastolic pressure in patients without distal tears may be higher than patients with proximal and distal tears. Increased diastolic pressure in the false lumen may predict worse outcomes than has been observed in studies of abdominal aortic aneurysms. We postulate that patients with impaired outflow from the false lumen may be at increased risk for expansion and aortic related events and may require more aggressive management including surgery or stent-graft therapy.

Table 4.1 Pressure in the true and false lumen stratified by tear size and tear location

	Model	A	B	C	A	B
	Tear Size / Location	6.4mm / proximal and distal tear	6.4mm / proximal tear	6.4mm / distal tear	3.2mm / proximal and distal tear	3.2mm / proximal tear
True Lumen	Systolic (mmHg)	117.34 ± 0.10	111.29 ± 0.08	114.58 ± 0.18	101.42 ± 0.18	124.04 ± 0.15
	Diastolic (mmHg)	**66.20 ± 0.12**	**54.66 ± 0.17**	**56.15 ± 0.16**	**58.01 ± 0.16**	**61.46 ± 0.22**
	Mean (mmHg)	91.46 ± 0.25	78.24 ± 0.23	78.62 ± 0.18	83.19 ± 0.18	88.63 ± 0.25
False Lumen	Systolic (mmHg)	116.51 ± 0.16	105.76 ± 0.06	107.86 ± 0.13	96.48 ± 0.13	112.89± 0.08
	Diastolic (mmHg)	**66.45 ± 0.16**	**58.95 ± 0.10**	**58.72 ± 0.24**	**60.91 ± 0.24**	**67.14± 0.04**
	Mean (mmHg)	91.30 ± 0.15	77.83 ± 0.31	77.62 ± 0.19	82.26 ± 0.19	87.53 ± 0.31
Comparison	Mean Difference	0.25 ± 0.13	4.41 ± 0.16	2.57 ± 0.21	2.90 ± 0.21	5.68 ± 0.16
	FPI%†	100.4% ±	107.9% ±	104.6% ±	105.0% ±	109% ± 0.38

P-value <.001 for all comparisons in the mean difference in Diastolic Blood Pressure (DBP) and in False lumen Pressure Index % (FPI%)

Table 4.2 Pressures (mmHg) in the presence of 3.2 mm proximal tear and constant systolic pressure with increasing heart rate

Heart Rate	TL-SP	TL-DP	TL-MP	FL-SP	FL-DP	FL-MP	SP▲	DP▲	MP▲	FL-SP%	**FPI%**
50 bpm	159.7	90.2	117.1	142.8	95.8	115.1	-16.9	5.6	-2.0	89.4	106.2
60 bpm	159.4	91.6	122.7	144.6	100.3	121.3	-14.7	8.7	-1.4	90.8	109.5
70 bpm	162.1	89.8	124.9	147.1	99.1	123.2	-15.0	9.3	-1.7	90.7	110.3
80 bpm	157.4	89.9	124.8	144.8	99.1	123.3	-12.6	9.2	-1.4	92.0	110.2

Abbreviations: TL-SP, true lumen systolic pressure; TL-DP, true lumen diastolic pressure; TL-MP, true lumen mean pressure; FL-SP, false lumen systolic pressure; FL-DP, false lumen diastolic pressure; FL-MP, false lumen-mean pressure; SP▲, change in systolic pressure; DP▲, change in diastolic pressure; MP▲, change in mean pressure; FL-SP%, false lumen pressure as percent of true lumen pressure; FPI%, false lumen pressure as percent of true lumen pressure

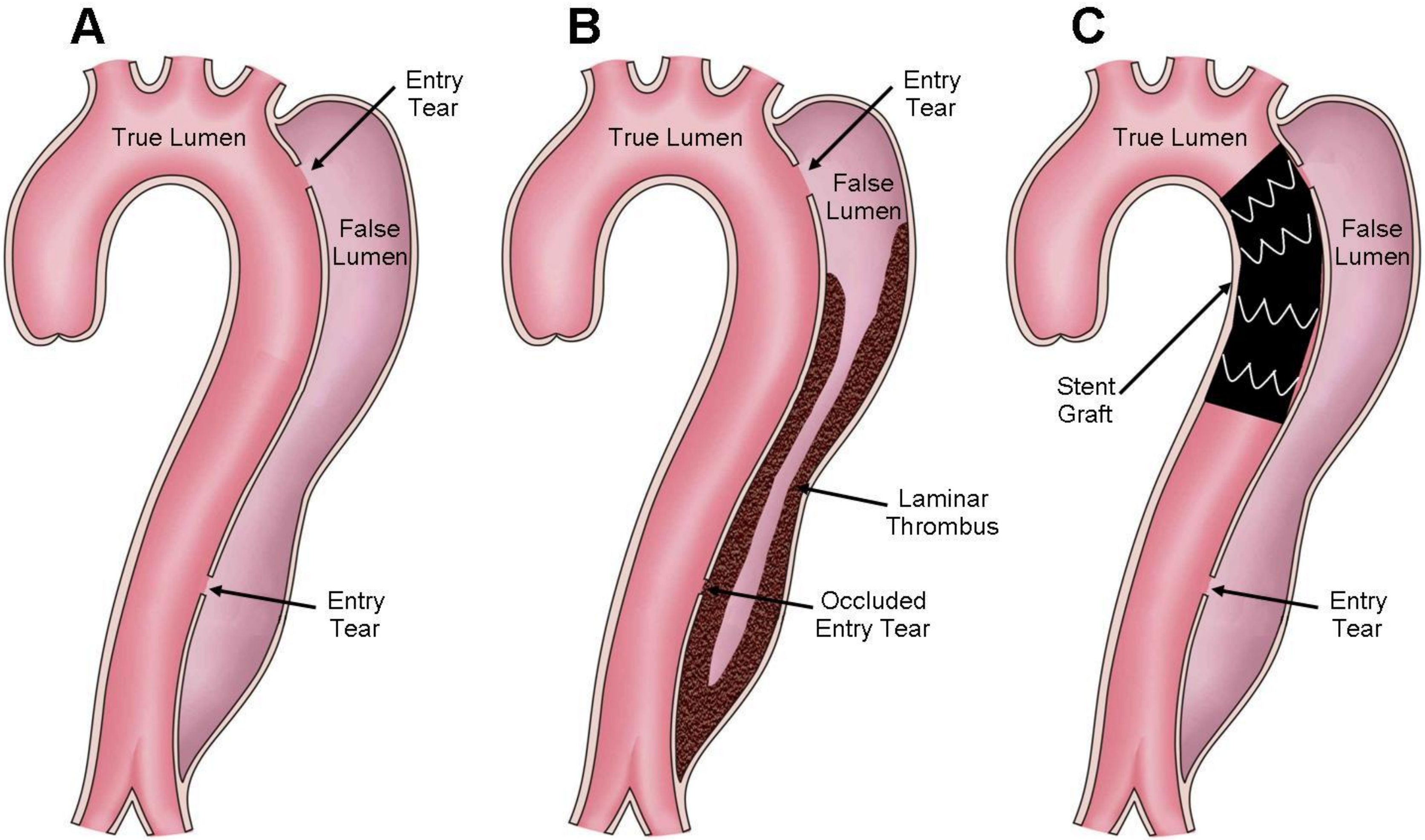

Figure 4.1 **A: Type B aortic dissection with a patent false lumen maintained by proximal and distal tears. B: Type B aortic dissection with partial thrombosis of the false lumen. The laminar thrombus can be seen occluding the distal tear. C: Type B aortic dissection with proximal stent graft and patent distal tear.**

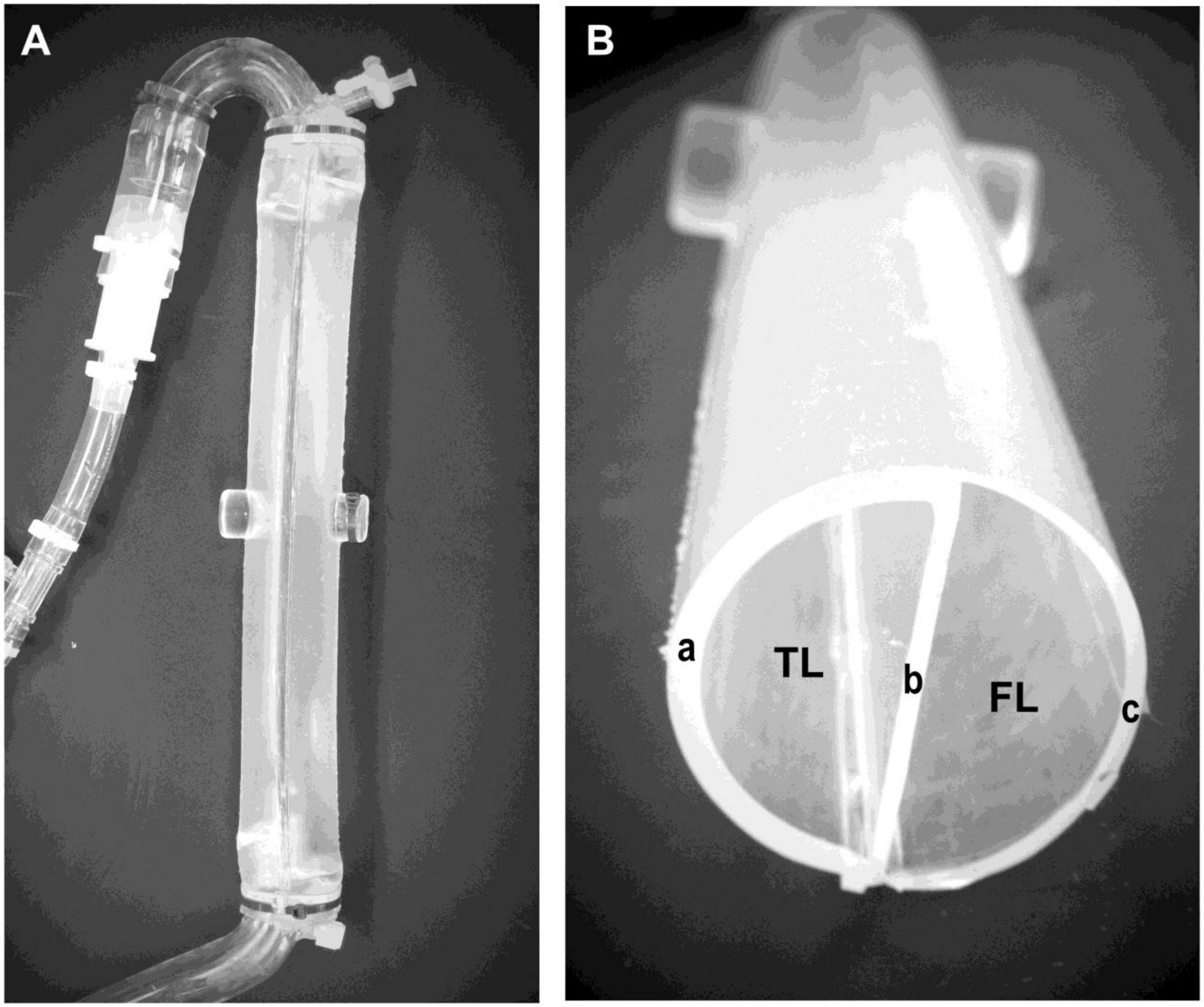

Figure 4.2 A: Photograph of chronic dissection model. B: Photograph of dissection model in cross section. TL; True Lumen, FL; False lumen, a: true lumen wall thickness = 3 mm; b: dissection flap wall thickness = 2 mm; c: false lumen wall thickness = 1 mm

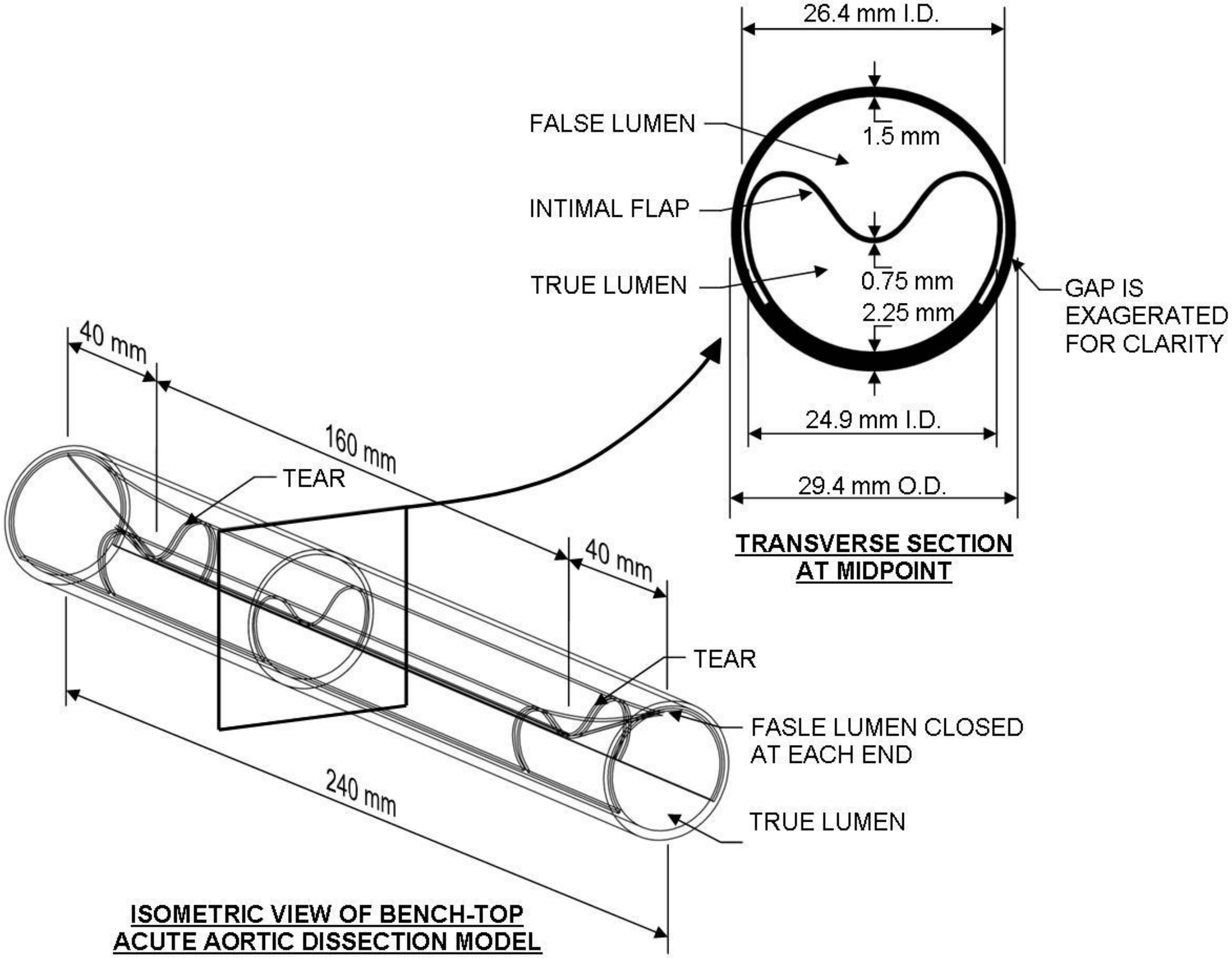

Figure 4.3 Schematic diagram of acute aortic dissection bench-top model

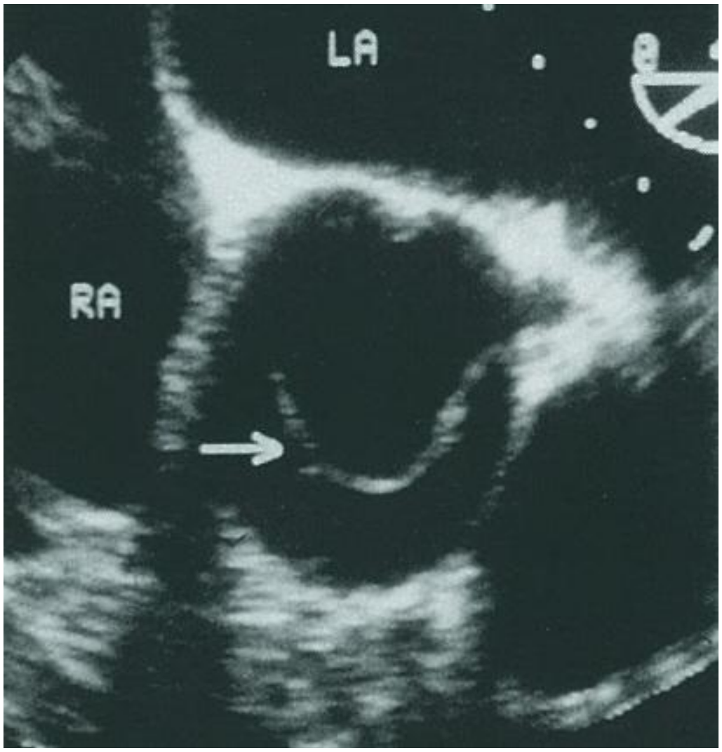

Figure 4.4 Image of acute type I aortic dissection, arrow points to intinmal flap [18]

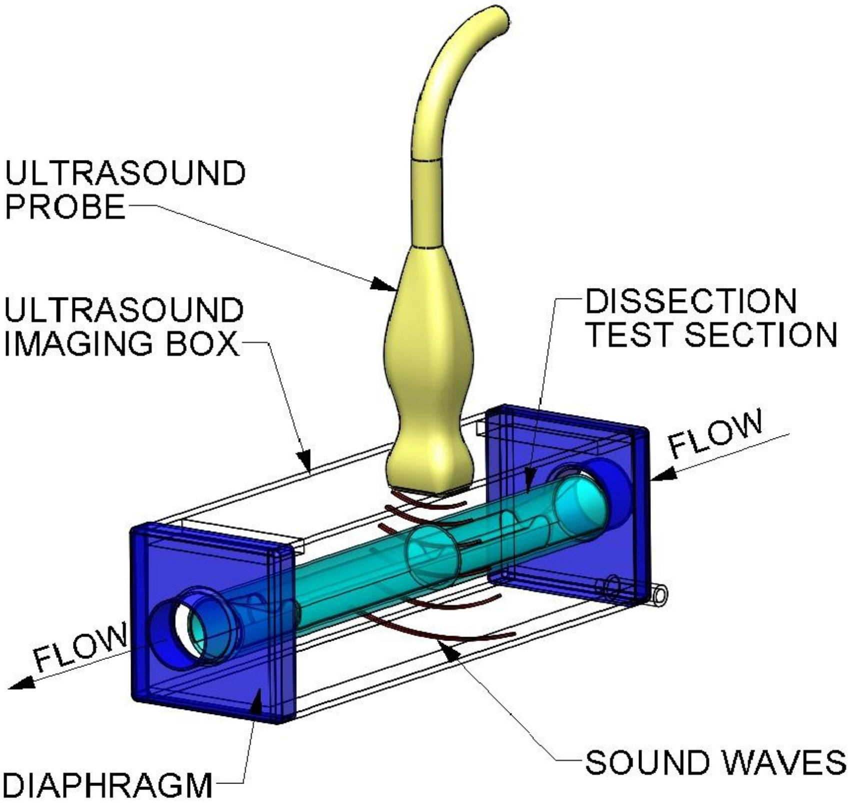

Figure 4.5 Ultrasound imaging setup

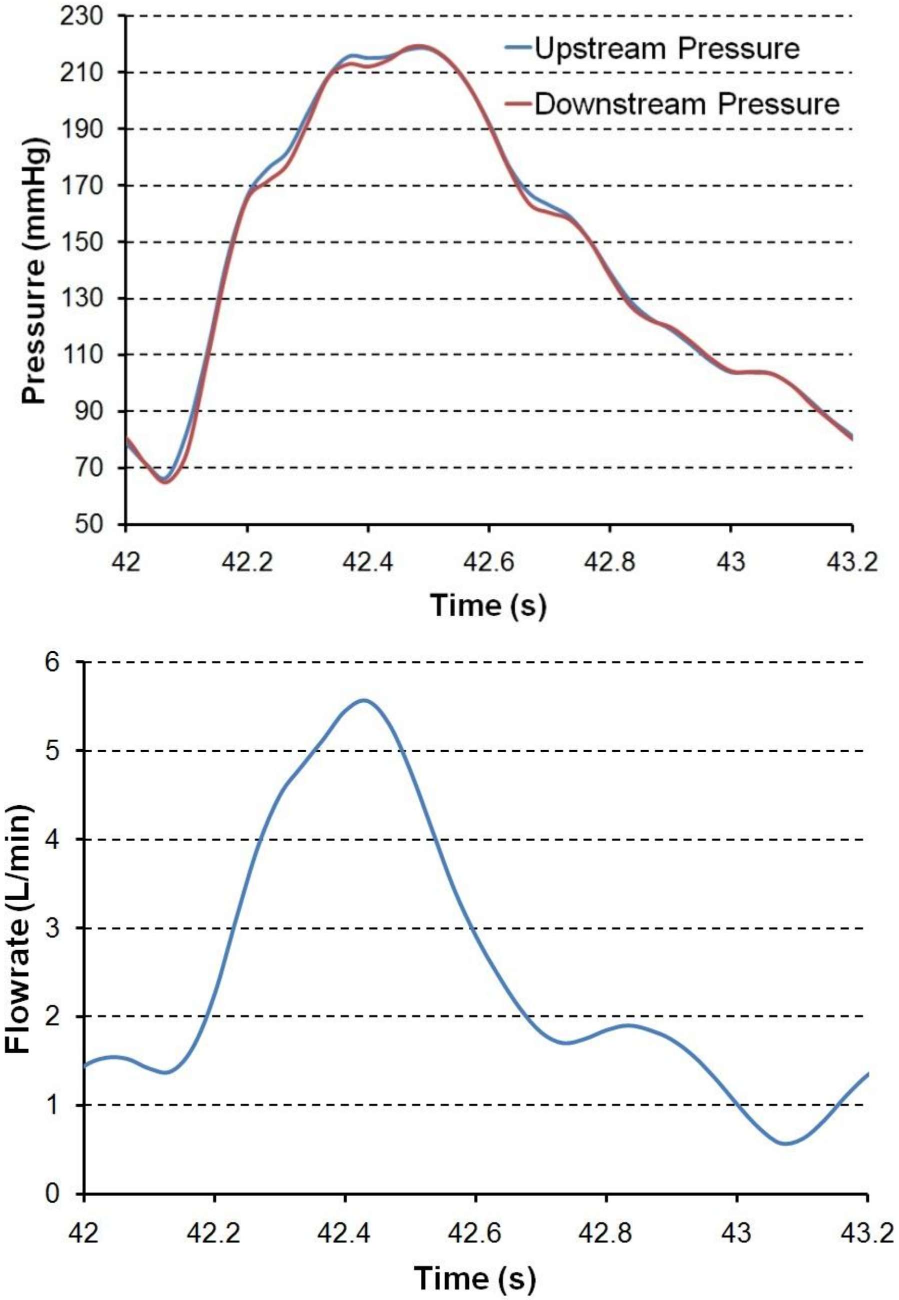

Figure 4.6 Pressure and flow rate waveforms of acute dissection model

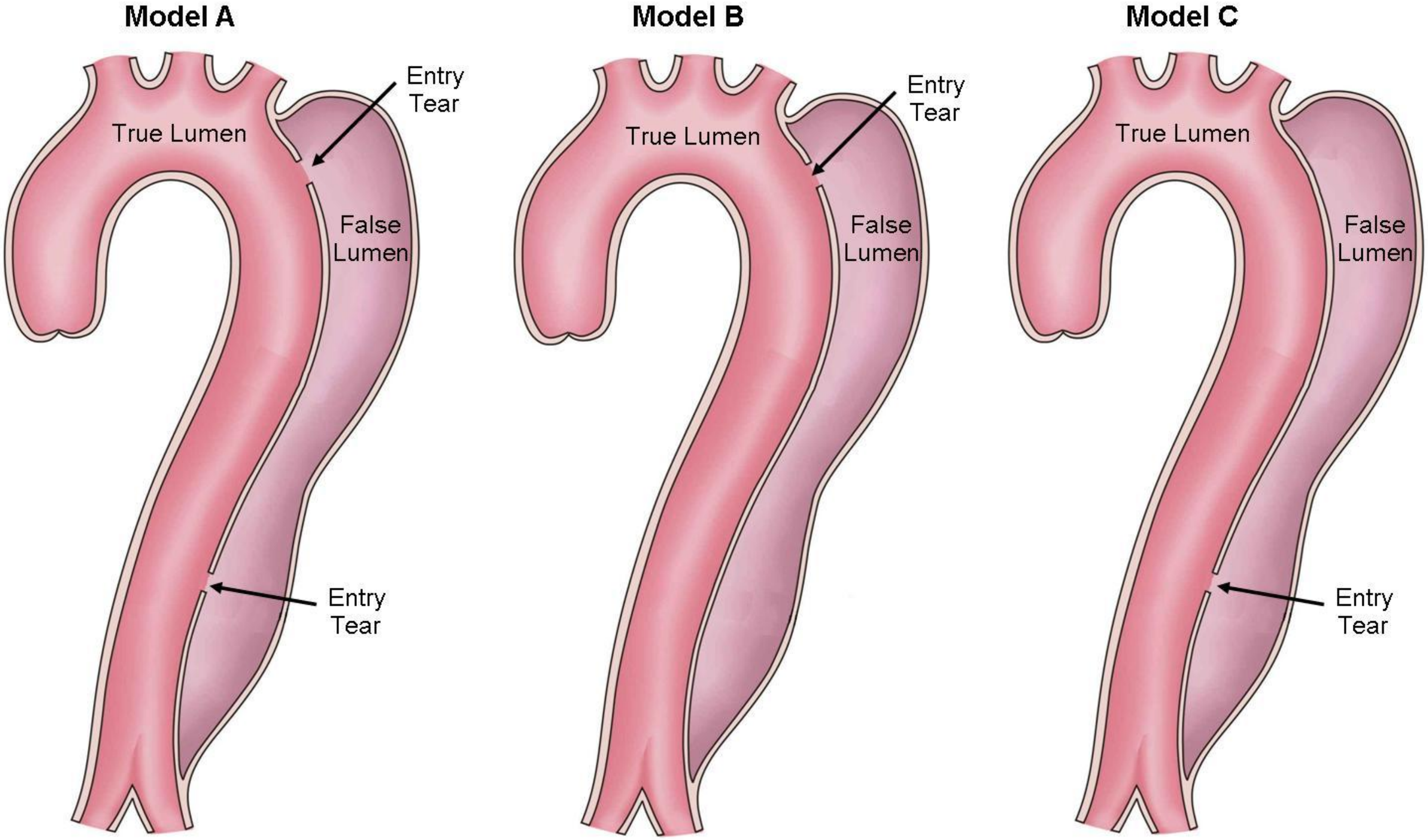

Figure 4.7 Dissection Model Configurations: Model A: Proximal and distal tear; Model B: Proximal tear only; Model C: Distal tear only

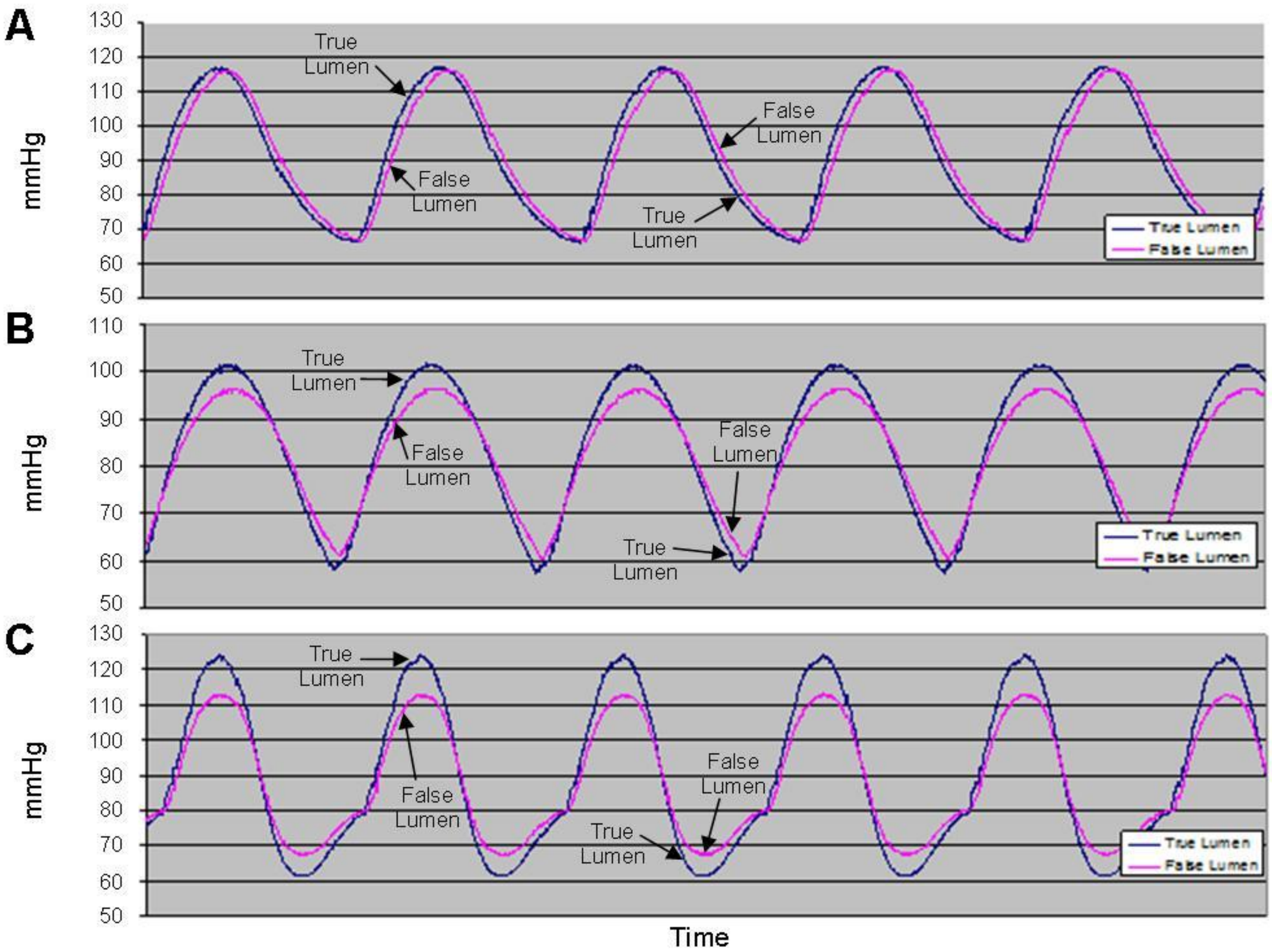

Figure 4.8 Pressure Waveforms. A: Dissection model A with 6.4 mm proximal and 6.4 mm distal tear; B: Dissection model B with proximal 6.4 mm tear only; C: Dissection model C with 3.2 mm tear only

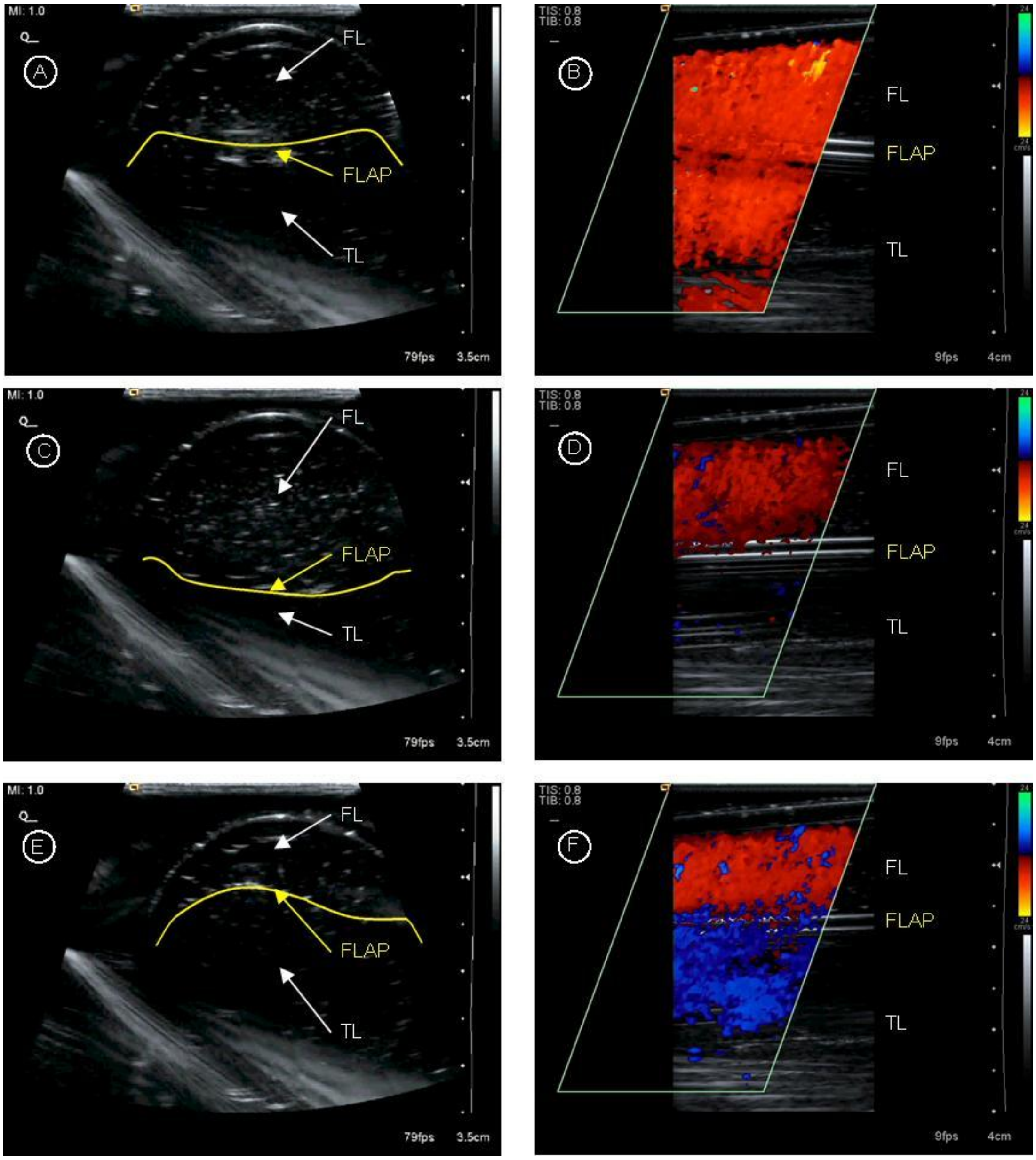

Figure 4.9 US images of acute dissection. Left column – transverse view, right column – longitudinal view with Doppler. Image A & B prior to peak systole – flow in both lumens. Image C & D just after peak systole – flow occluded in TL. Image E & F just prior to diastole – negative flow observed in TL (FL – False Lumen, TL – True Lumen)

4.6 References

[1] R. Erbel*, et al.*, "Effect of medical and surgical therapy on aortic dissection evaluated by transesophageal echocardiography. Implications for prognosis and therapy. The European Cooperative Study Group on Echocardiography," *Circulation,* vol. 87, pp. 1604-15, May 1993.

[2] Y. Bernard*, et al.*, "False lumen patency as a predictor of late outcome in aortic dissection," *Am J Cardiol,* vol. 87, pp. 1378-82, Jun 15 2001.

[3] R. Pretre and L. K. Von Segesser, "Aortic dissection," *Lancet,* vol. 349, pp. 1461-4, May 17 1997.

[4] T. T. Tsai*, et al.*, "Partial thrombosis of the false lumen in patients with acute type B aortic dissection," *N Engl J Med,* vol. 357, pp. 349-59, Jul 26 2007.

[5] D. M. Williams*, et al.*, "The dissected aorta: part III. Anatomy and radiologic diagnosis of branch-vessel compromise," *Radiology,* vol. 203, pp. 37-44, Apr 1997.

[6] J. W. Chung*, et al.*, "True-lumen collapse in aortic dissection: part I. Evaluation of causative factors in phantoms with pulsatile flow," *Radiology,* vol. 214, pp. 87-98, Jan 2000.

[7] J. W. Chung*, et al.*, "True-lumen collapse in aortic dissection: part II. Evaluation of treatment methods in phantoms with pulsatile flow," *Radiology,* vol. 214, pp. 99-106, Jan 2000.

[8] H. Eggebrecht*, et al.*, "Endovascular stent-graft placement in aortic dissection: a meta-analysis," *Eur Heart J,* Oct 14 2005.

[9] C. A. Nienaber*, et al.*, "Provisional extension to induce complete attachment after stent-graft placement in type B aortic dissection: the PETTICOAT concept," *J Endovasc Ther,* vol. 13, pp. 738-46, Dec 2006.

[10] T. T. Tsai*, et al.*, "Tear size and location impacts false lumen pressure in an ex vivo model of chronic type B aortic dissection," *Journal of Vascular Surgery,* vol. 47, pp. 844-851, 2008.

[11] A. E. Li*, et al.*, "Using MRI to assess aortic wall thickness in the multiethnic study of atherosclerosis: distribution by race, sex, and age," *AJR Am J Roentgenol,* vol. 182, pp. 593-7, Mar 2004.

[12] K. Kumar, "Effect of Tangential Pressure of Pulsation on Tunica Media of Human Arteries," *J Anat Soc India,* vol. 51, pp. 35-38, 2002.

[13] M. L. Raghavan and D. A. Vorp, "Toward a biomechanical tool to evaluate rupture potential of abdominal aortic aneurysm: identification of a finite strain constitutive model and evaluation of its applicability," *J Biomech,* vol. 33, pp. 475-82, Apr 2000.

[14] L. E. Quint*, et al.*, "Aortic intimal tears: detection with spiral computed tomography," *J Endovasc Ther,* vol. 10, pp. 505-10, Jun 2003.

[15] T. T. Tsai*, et al.*, "Acute aortic syndromes," *Circulation,* vol. 112, pp. 3802-13, Dec 13 2005.

[16] T. T. Tsai*, et al.*, "Long-Term Survival in Patients Presenting With Type B Acute Aortic Dissection: Insights From the International Registry of Acute Aortic Dissection," *Circulation,* vol. 114, pp. 2226-2231, 2006.

[17] R. Erbel*, et al.*, "Diagnosis and management of aortic dissection," *Eur Heart J,* vol. 22, pp. 1642-81, Sep 2001.

[18] H. G. Borst, et al., Surgical treatment of aortic dissection. New York: Churchill Livingstone International, pp. 71, 1996.

Chapter 5

Conclusions and Future Direction

5.1 Conclusions

An experimental model was designed to study flow in chronic and acute human aortic dissection. This study aimed to develop flexible wall models with mechanical properties similar to those of human aortic dissection. Polydimethylsiloxane (PDMS) was utilized for the model's vessel walls and data was collected for mechanical properties of the PDMS in the range that soft tissue would experience. We investigated an innovative non-invasive method of determining the elastic modulus of the arterial wall based on dynamic DICOM files using high resolution CT scanning. The risk of enlargement and rupture of a dissected aorta may be determined by the biomechanical stresses mapped out by these scans. Flexible wall models of both chronic and acute Stanford Type B aortic dissections were built. Pressure differences in the true and false lumen as well as intimal flap movement were observed.

Several limitations of this study should be noted. Although the tensile strength of our dissection models was very similar to a healthy human aorta, the actual tensile strength of the true and false lumen of the descending aorta is unknown. We continue to explore the possibility of measuring changes in arterial dimensions by CTA in patients with aortic dissections. The dissection models we built were idealized straight tube geometries. Patient specific geometries are tortuous and the intact portion of the true lumen wall is normally spiraled as it progresses distally. However, we hypothesize that if a numerical model is validated for idealized three-dimensional geometries, it will also be accurate for the complex geometries of diseased human aortas. Lastly, the effects of space occupying thrombus, patent side branches, or both on false lumen hemodynamics are unknown and warrant further investigation.

5.2 Future Direction

The strain rates that we used for determining the mechanical properties of the PDMS were at the maximum (500 mm/min) for the machine that we used. However, strain rates experienced by the soft tissues in the human aortic wall are at a substantially higher rate. Oishi et al. [1] reported average strain rates observed in the human aorta of 39 patients utilizing ultrasonography of 2,250, 2,700 and 3,900 mm/min for young, middle and old-aged groups respectively. Further investigation is needed to determine the elastic modulus of PDMS mixing ratios at higher physiological strain rates for better experimental modeling utilizing PDMS and validation of numerical modeling. Furthermore, although vacuum level, temperature and curing time were consistent for tensile test sections and dissection models, an additional curing application was applied in the development of the acute dissection model. The tubes were subjected to an additional 18 hours in the oven at 65° C in order to bond the two previously cast tubes (inner and outer) for the acute model. The affect this had on the elastic properties of the PDMS was not investigated. In addition, the mechanical properties of the combination of the two different mixing ratios (inner and outer tubes) when bonded together as the true lumen wall was not investigated.

A coordinate-tracking algorithm may be developed to determine the elastic values of the walls of a dissected aorta from the dynamic CT (Computerized tomography) DICOM files of patients with aortic dissections. The measurements of elasticity in aortic strips that we conducted in a tensile testing machine were conducted uni-axially, corresponding to either the circumferential or longitudinal direction. The elastic properties of the human aorta are anisotropic with *in-vivo* stresses being both radial and longitudinal therefore, a more accurate measurement of elasticity would be in a bi-axial testing machine with biaxial strain imposed on the aortic tissue simultaneously (the design of a device to measure tissue bi-axially may be found in Appendix D). Using aortic tissue from a patient when they undergo direct surgical repair of their aortic dissection the elastomechanical measurement may be used to validate the calculations of elasticity derived from their dynamic CT scan files.

This dissertation represents the first experimental investigation of flexible wall aortic models of dissection with mechanical properties similar to those of human. As the techniques contained herein are better refined, it will enhance our knowledge of flow patterns and subsequent vessel wall response. Additional monitoring or visualizing of flow patterns, such as Particle Imaging Velocimetry (PIV), may discover factors that affect development or progression of dissection and may serve to validate future computational dynamic fluid-structure interaction (FSI) models.

5.3 References

[1] Y. Oishi, et al., "A Novel Approach to Assess Aortic Stiffness Related to Changes in Aging Using a Two-Dimensional Strain Imaging," Echocardiography, vol. 25, pp. 941-945, 2008.

APPENDICES

Appendix A

DRAWINGS

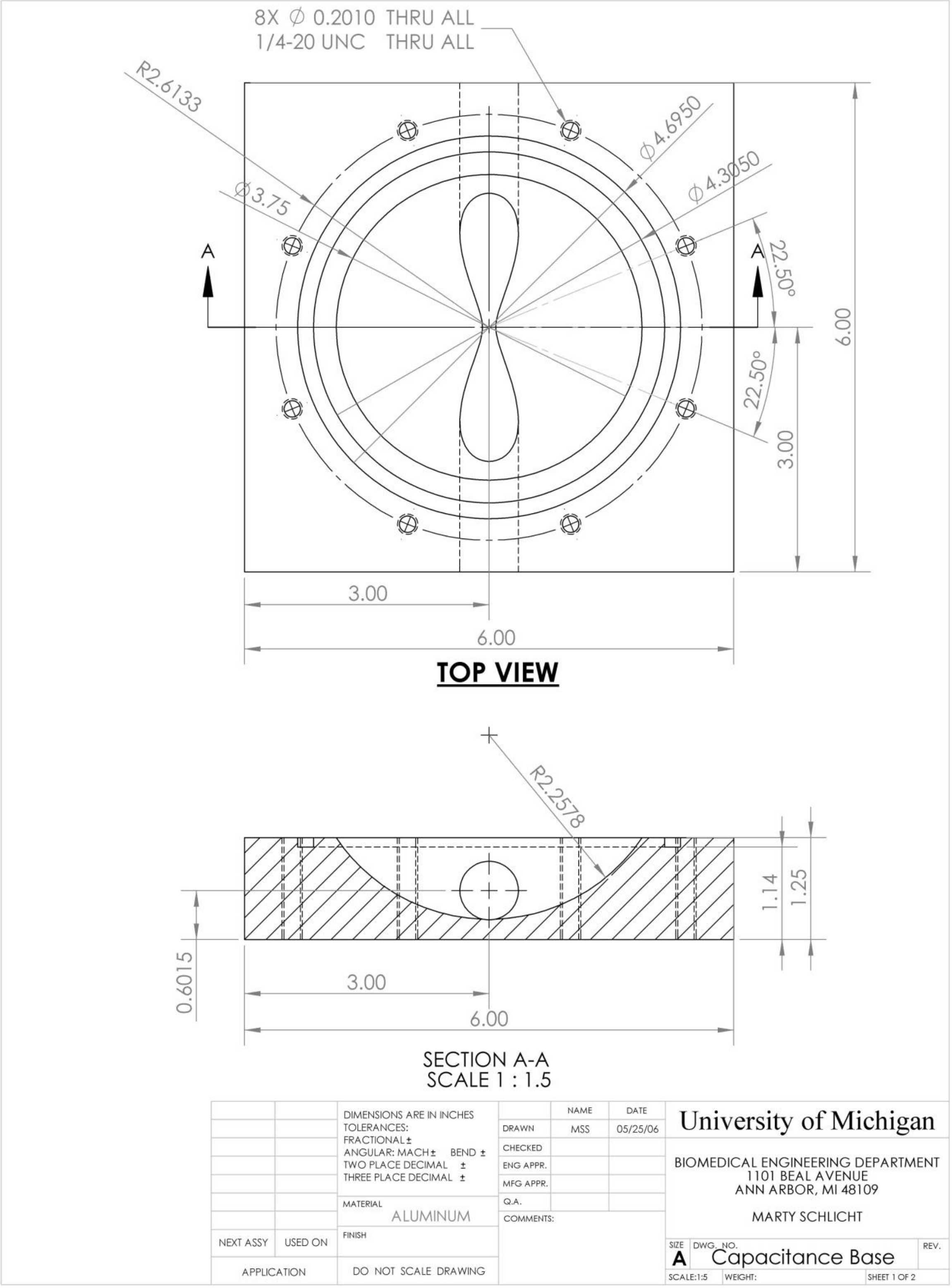

A.1 Capacitance base - sheet 1 of 2

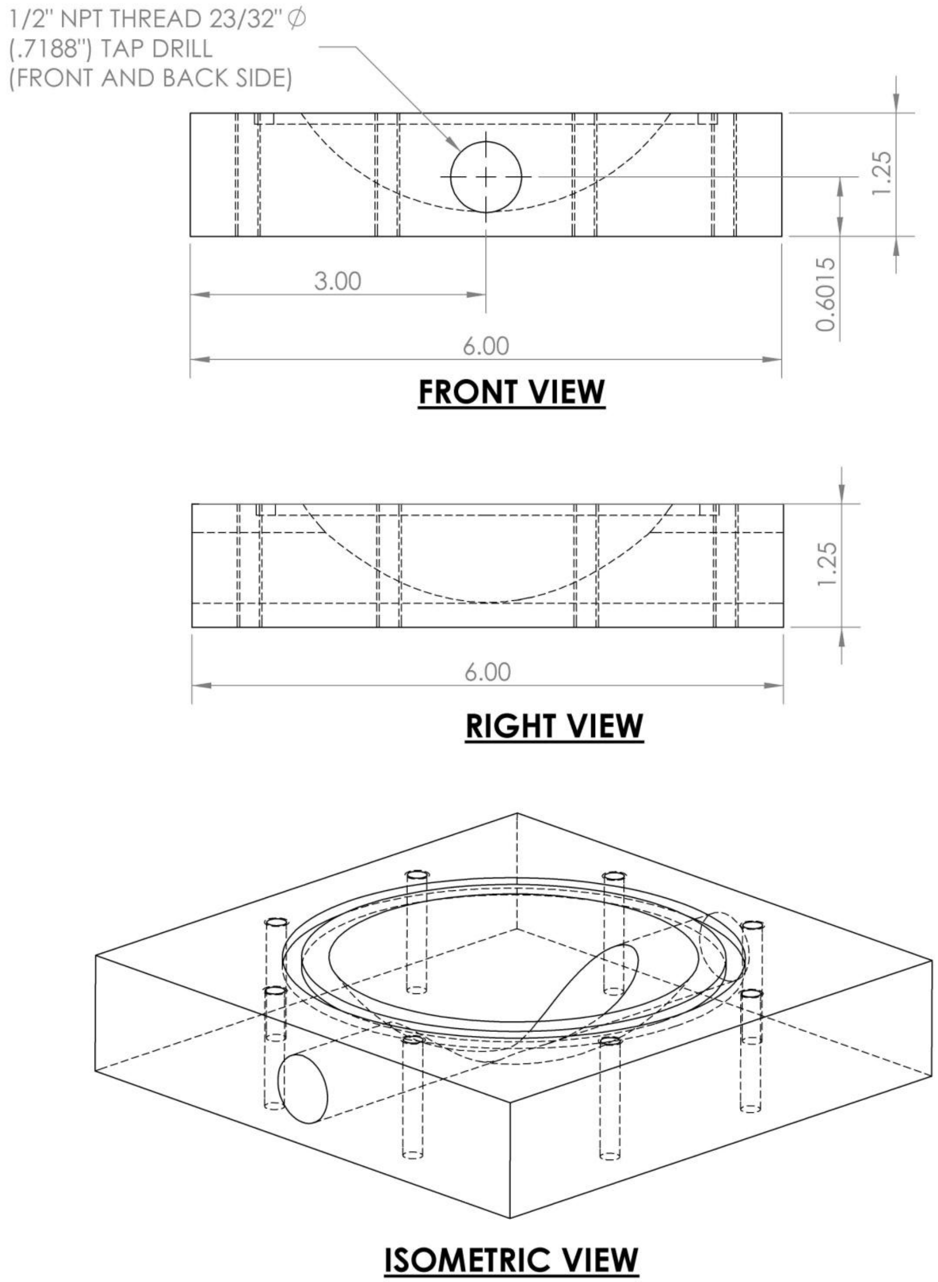

DIMENSIONS ARE IN INCHES
TOLERANCES:
FRACTIONAL ±
ANGULAR: MACH ± BEND ±
TWO PLACE DECIMAL ±
THREE PLACE DECIMAL ±

MATERIAL
ALUMINUM

FINISH

NEXT ASSY USED ON
APPLICATION
DO NOT SCALE DRAWING

	NAME	DATE
DRAWN	MSS	05/25/06
CHECKED		
ENG APPR.		
MFG APPR.		
Q.A.		

COMMENTS:

University of Michigan

BIOMEDICAL ENGINEERING DEPARTMENT
1101 BEAL AVENUE
ANN ARBOR, MI 48109

MARTY SCHLICHT

SIZE A DWG. NO. Capacitance Base REV.
SCALE:1:5 WEIGHT: SHEET 2 OF 2

A.2 Capacitance base - sheet 2 of 2

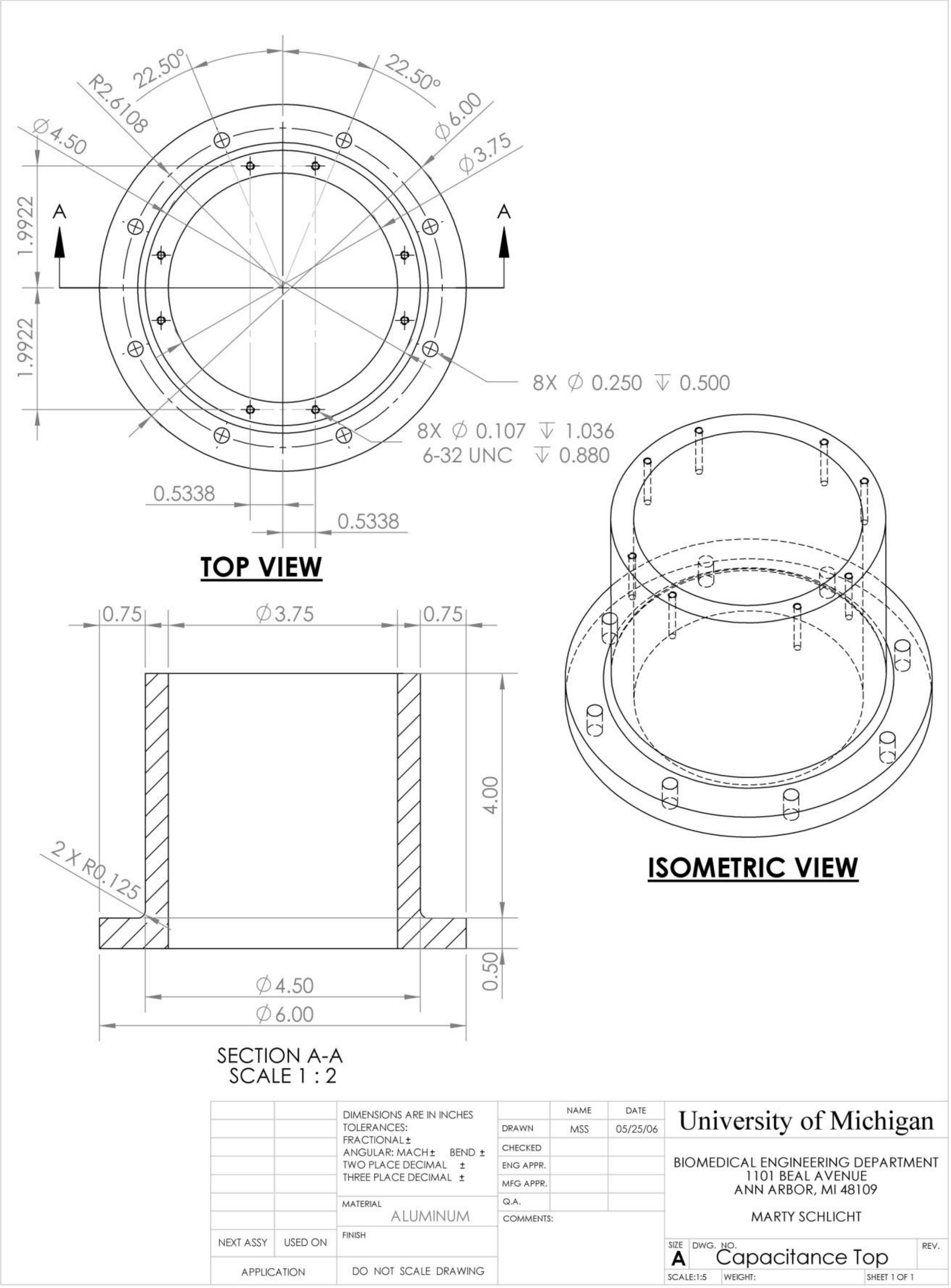

A.3 Capacitance top - sheet 1 of 1

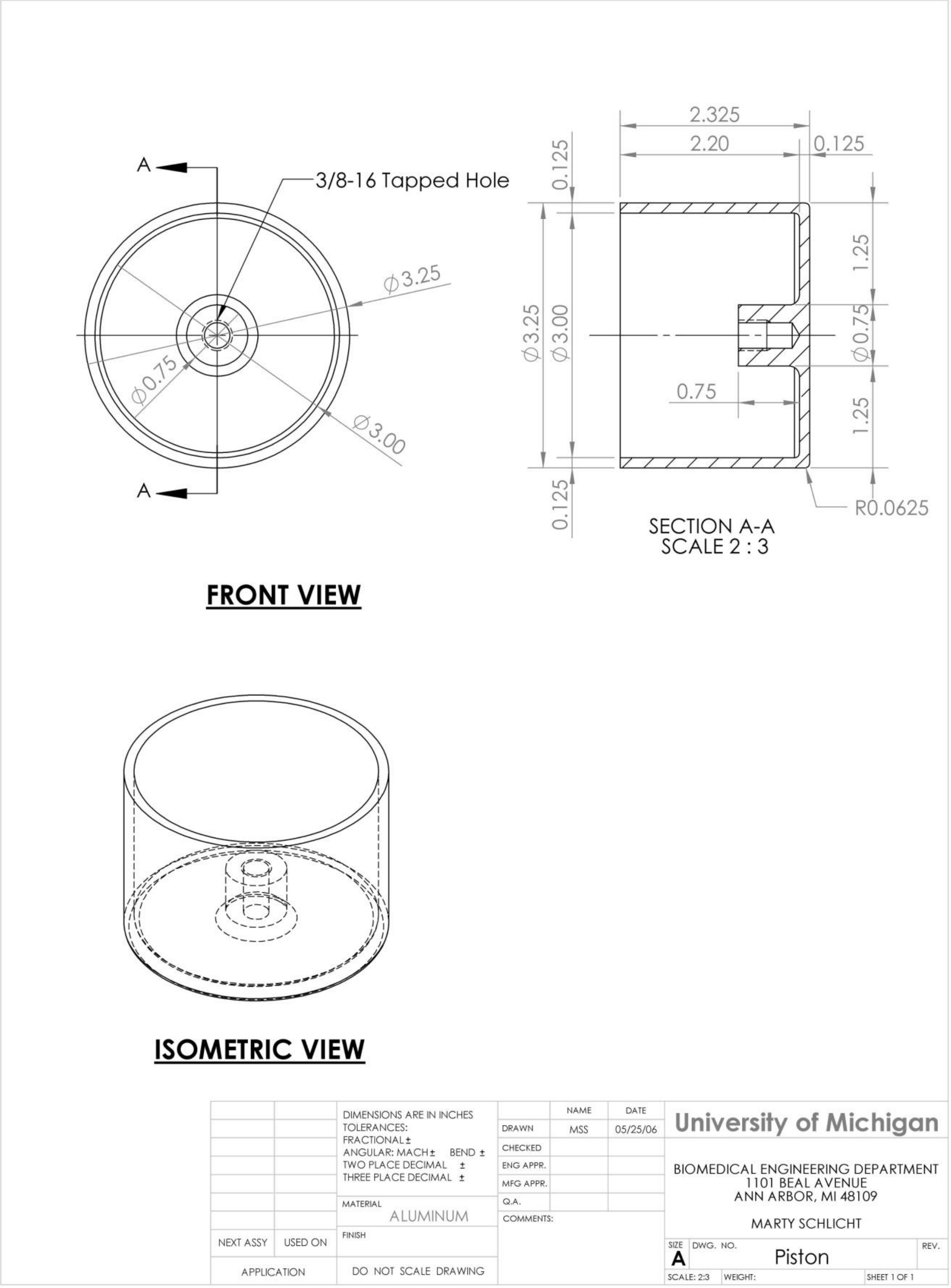

DIMENSIONS ARE IN INCHES
TOLERANCES:
FRACTIONAL ±
ANGULAR: MACH ± BEND ±
TWO PLACE DECIMAL ±
THREE PLACE DECIMAL ±

MATERIAL: ALUMINUM

FINISH

NEXT ASSY | USED ON

APPLICATION

DO NOT SCALE DRAWING

	NAME	DATE
DRAWN	MSS	05/25/06
CHECKED		
ENG APPR.		
MFG APPR.		
Q.A.		

COMMENTS:

University of Michigan

BIOMEDICAL ENGINEERING DEPARTMENT
1101 BEAL AVENUE
ANN ARBOR, MI 48109

MARTY SCHLICHT

SIZE A DWG. NO. Piston REV.

SCALE: 2:3 WEIGHT: SHEET 1 OF 1

A.4 Capacitance piston - sheet 1 of 1

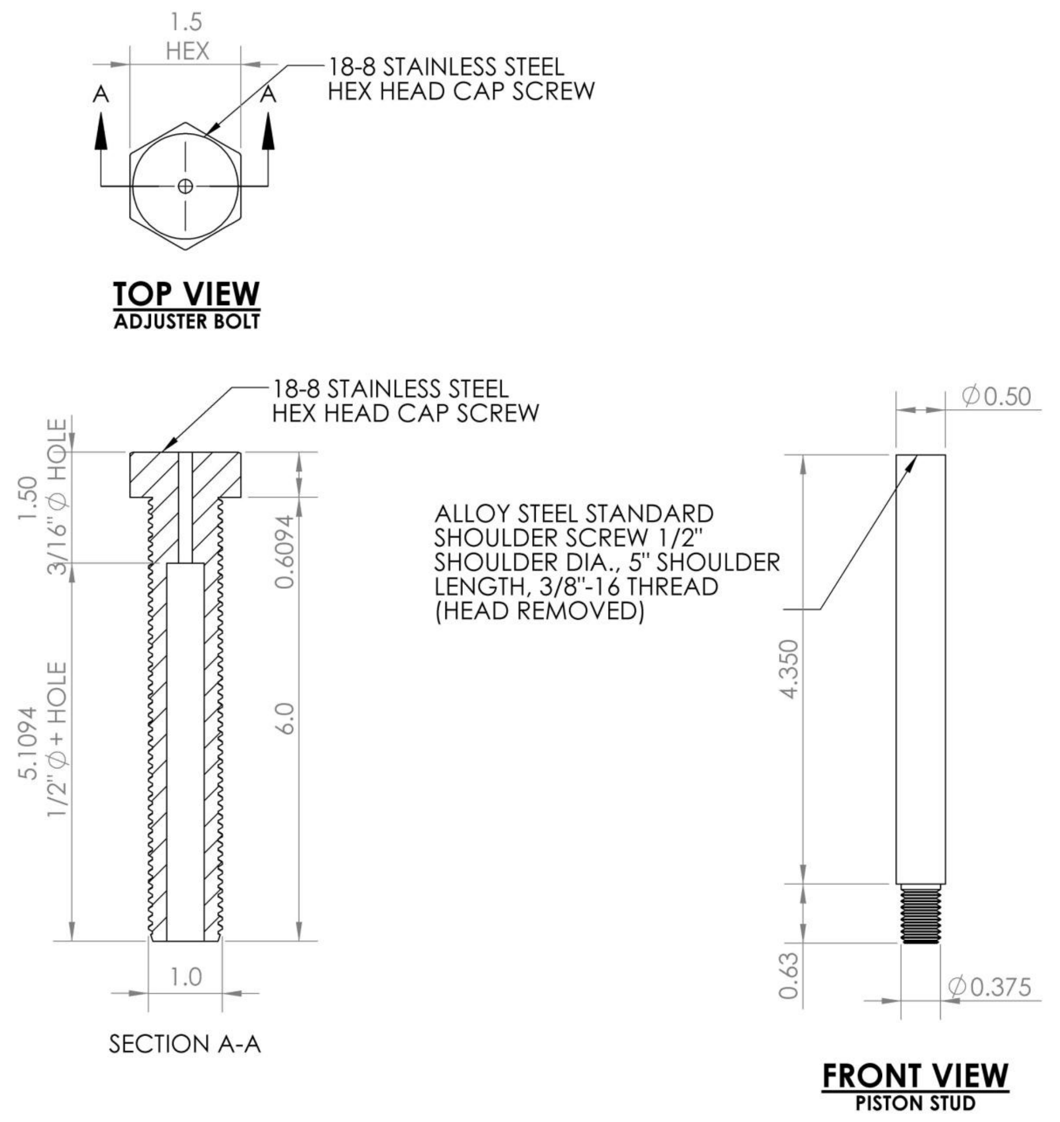

DIMENSIONS ARE IN INCHES TOLERANCES: FRACTIONAL ± ANGULAR: MACH ± BEND ± TWO PLACE DECIMAL ± THREE PLACE DECIMAL ±		NAME	DATE	University of Michigan
	DRAWN	MSS	05/25/06	BIOMEDICAL ENGINEERING DEPARTMENT 1101 BEAL AVENUE ANN ARBOR, MI 48109
	CHECKED			
	ENG APPR.			
	MFG APPR.			
MATERIAL LISTED	Q.A.			MARTY SCHLICHT
FINISH	COMMENTS:			SIZE A DWG. NO. Adjuster Bolt and Piston Stud REV.
DO NOT SCALE DRAWING				SCALE:1:2 WEIGHT: SHEET 1 OF 1

NEXT ASSY USED ON
APPLICATION

A.5 Adjuster bolt and piston stud - sheet 1 of 1

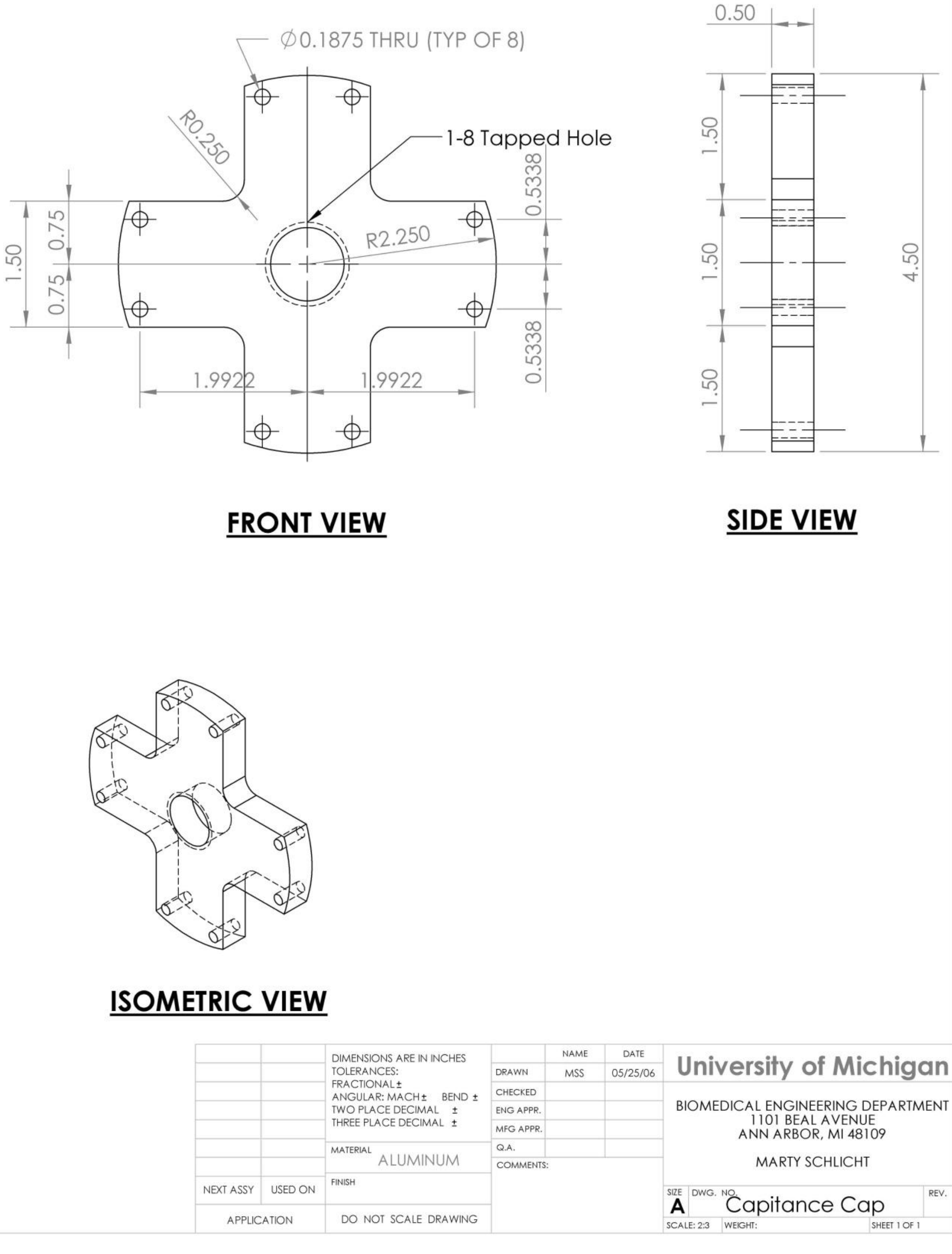

		DIMENSIONS ARE IN INCHES TOLERANCES: FRACTIONAL ± ANGULAR: MACH ± BEND ± TWO PLACE DECIMAL ± THREE PLACE DECIMAL ±		NAME	DATE	University of Michigan
			DRAWN	MSS	05/25/06	
			CHECKED			BIOMEDICAL ENGINEERING DEPARTMENT 1101 BEAL AVENUE ANN ARBOR, MI 48109
			ENG APPR.			
			MFG APPR.			
		MATERIAL ALUMINUM	Q.A.			MARTY SCHLICHT
			COMMENTS:			
NEXT ASSY	USED ON	FINISH				SIZE A DWG. NO. Capitance Cap REV.
APPLICATION		DO NOT SCALE DRAWING				SCALE: 2:3 WEIGHT: SHEET 1 OF 1

A.6 Capacitance cap - sheet 1 of 1

ITEM NO.	PART NUMBER	DESCRIPTION	QTY.
1	Capacitance Top	See Drawing Appendix A - A.3	1
2	Piston	See Drawing Appendix A - A.4	1
3	Piston Stud	See Drawing Appendix A - A.5	1
4	Adjuster Bolt	See Drawing Appendix A - A.5	1
5	Oring	Viton AS568A Dash Number 245	1
6	Capitance Cap	See Drawing Appendix A - A.6	1
7	5372K123 (McMaster)	Double Barbed Tube Fitting	2
8	92196A158 (McMaster)	6-32 Socket Head Cap Screw	8
9	Capacitance Base	See Drawing Appendix A - A.1, A.2	1
10	92196A544 (McMaster)	1/4-20 Socket Head Cap Screw	8
11	Rolling Diaphragm	Bellofram Corp., Class 4, 3.75" Cylinder Bore, 3.50" Piston Diameter, Height 3.75", Sidewall Thickness - D, Effective Pressure Area 10.32 sq in, Convolution 0.125", Max Half Stroke 3.24	1
12	Capacitance Spring	Varies	1

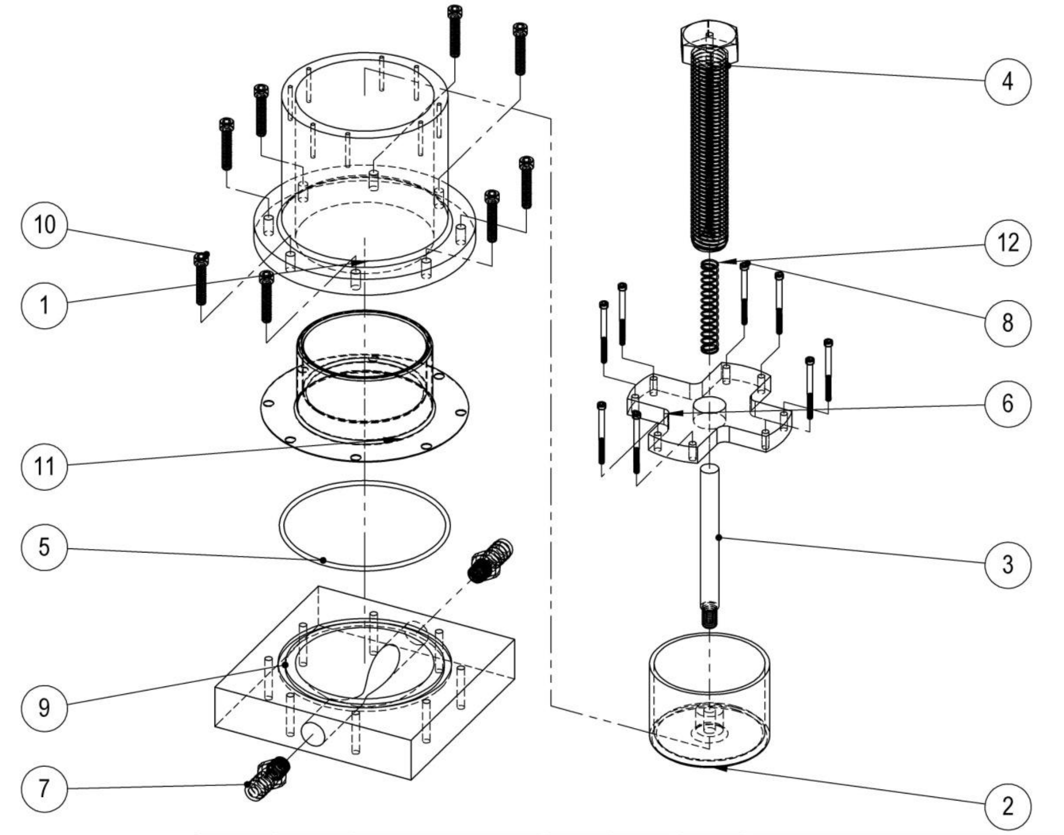

		DIMENSIONS ARE IN INCHES TOLERANCES: FRACTIONAL ± ANGULAR: MACH ± BEND ± TWO PLACE DECIMAL ± THREE PLACE DECIMAL ±		NAME	DATE
			DRAWN	MSS	11/10/10
			CHECKED		
			ENG APPR.		
			MFG APPR.		
		MATERIAL	Q.A.		
			COMMENTS:		
NEXT ASSY	USED ON	FINISH			
APPLICATION		DO NOT SCALE DRAWING			

University of Michigan

BIOMEDICAL ENGINEERING DEPARTMENT
1101 BEAL AVENUE
ANN ARBOR, MI 48109

MARTY SCHLICHT

SIZE A DWG. NO. capacitance assembly REV.

SCALE: 1:4 WEIGHT: SHEET 1 OF 1

A.7 Capacitance Assembly - sheet 1 of 1

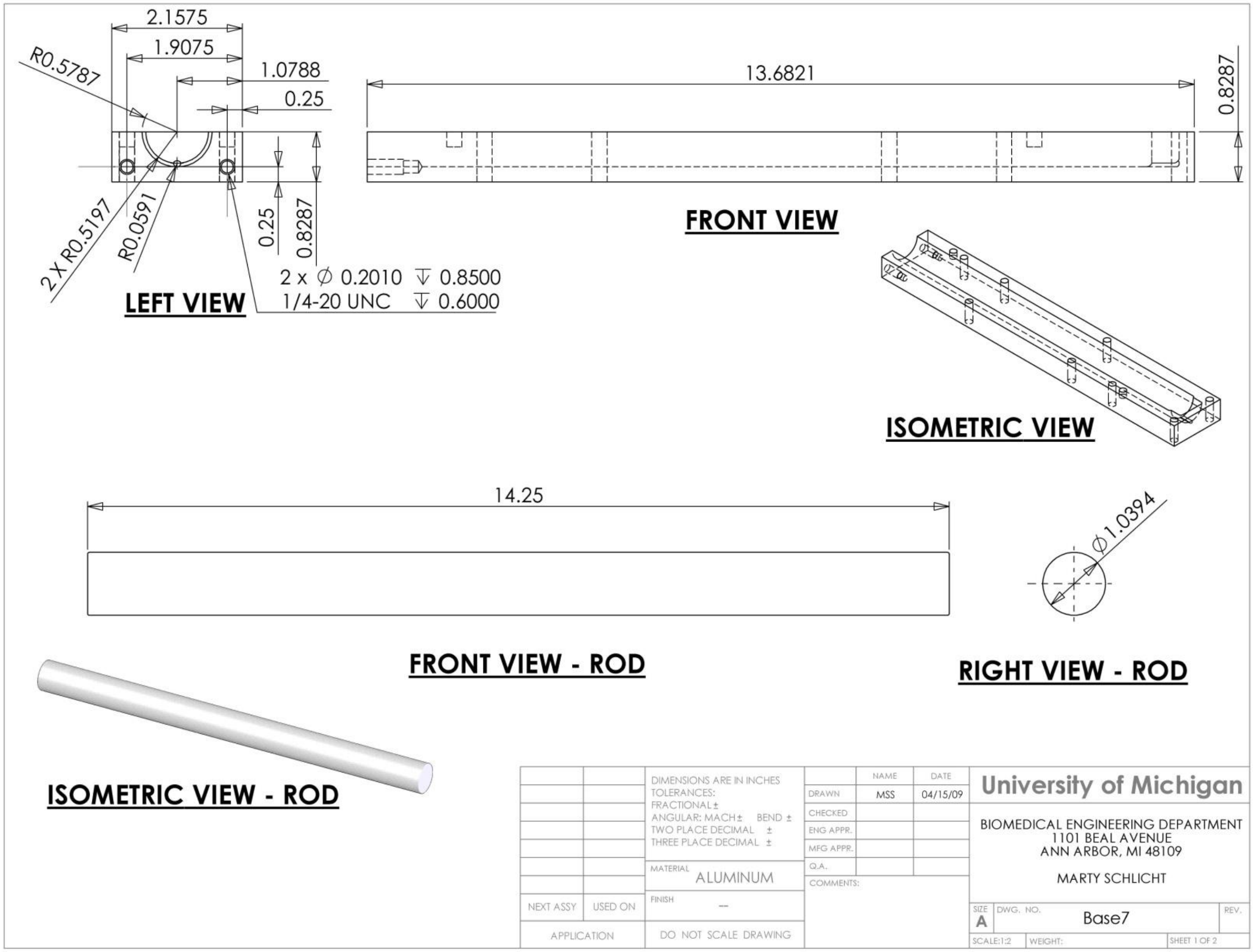

A.8 Acute Dissection mold: Base 7 - sheet 1 of 2

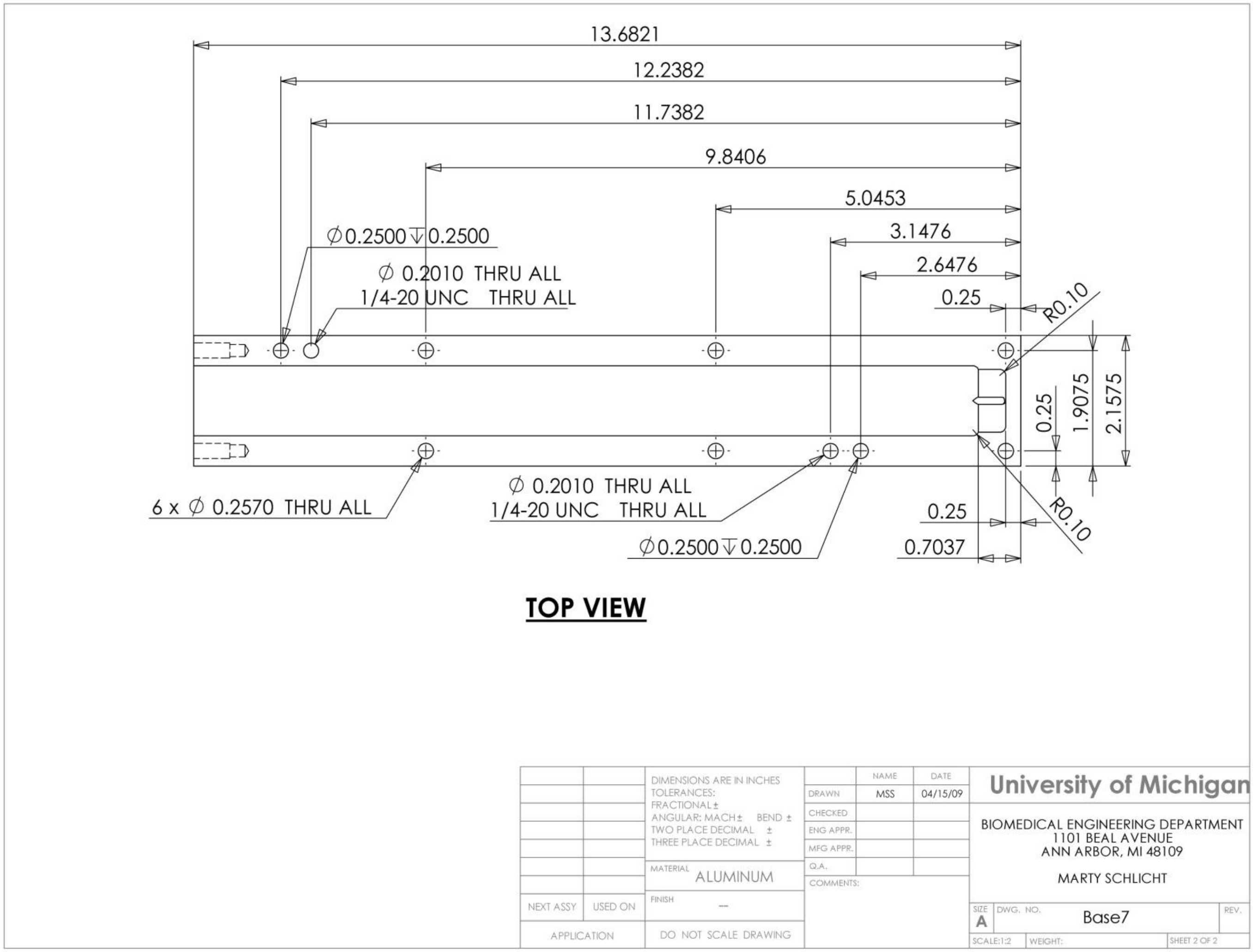

A.9 Acute Dissection mold: Base 7 - sheet 2 of 2

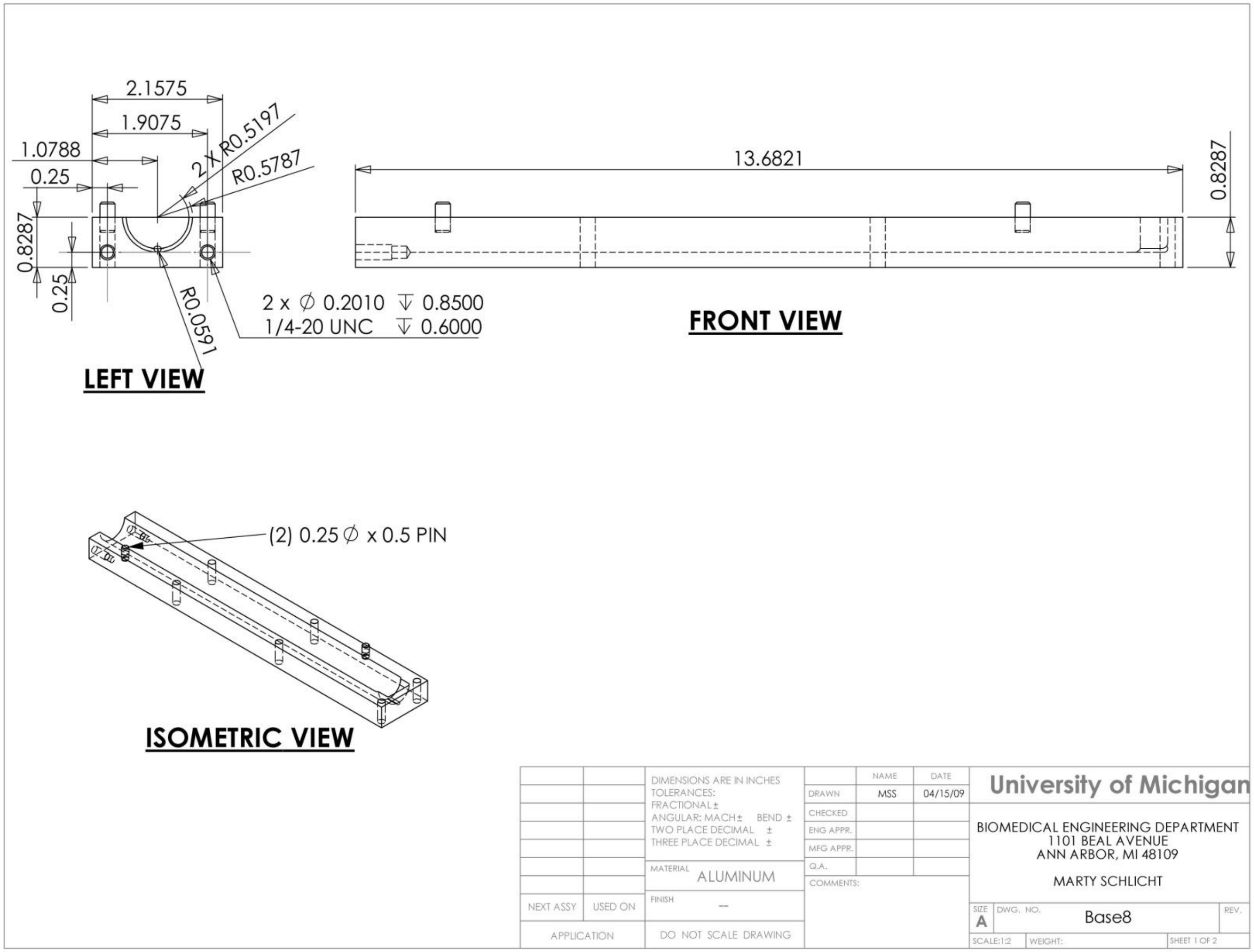

A.10 Acute Dissection mold: Base 8 - sheet 1 of 2

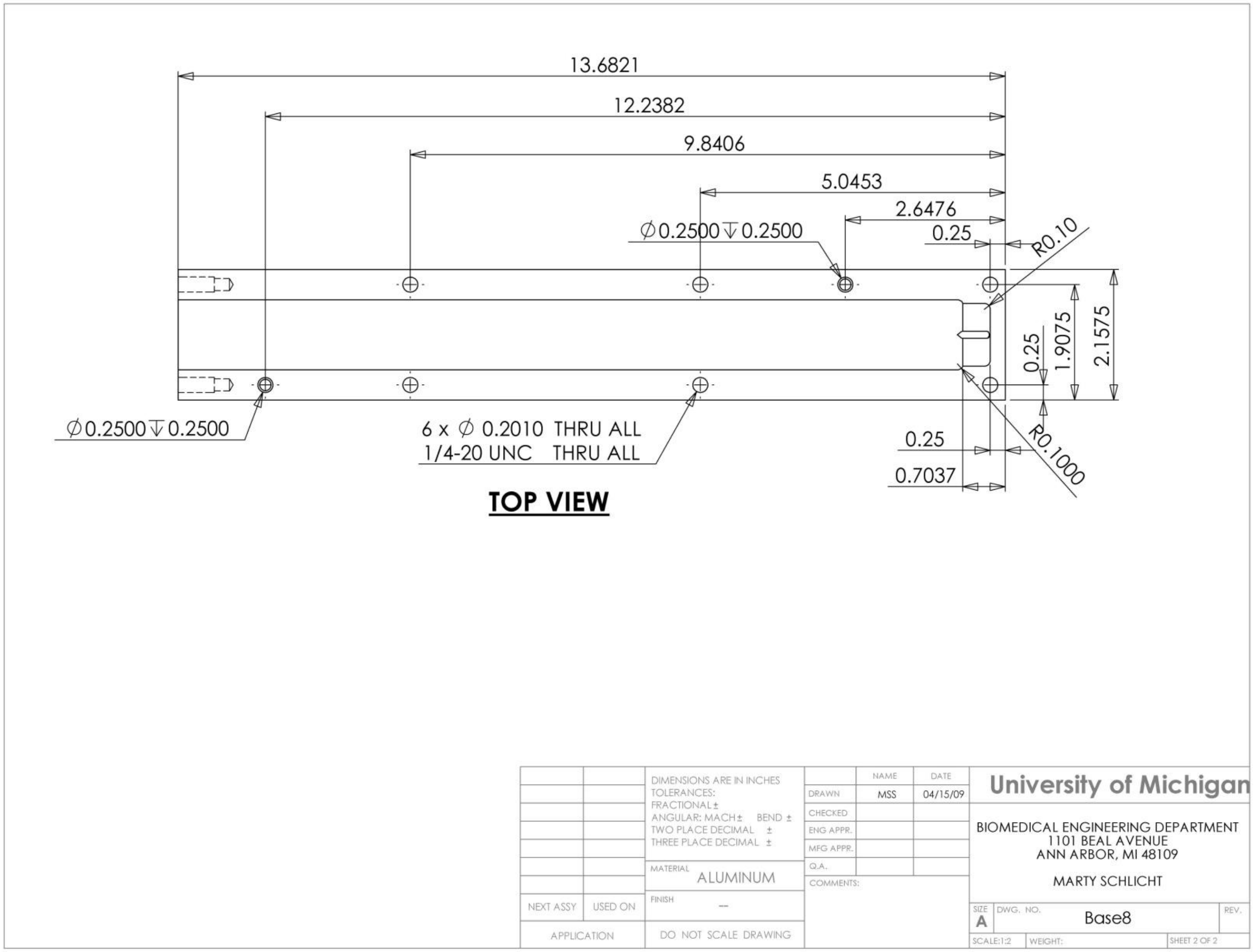

A.11 Acute Dissection mold: Base 8 - sheet 2 of 2

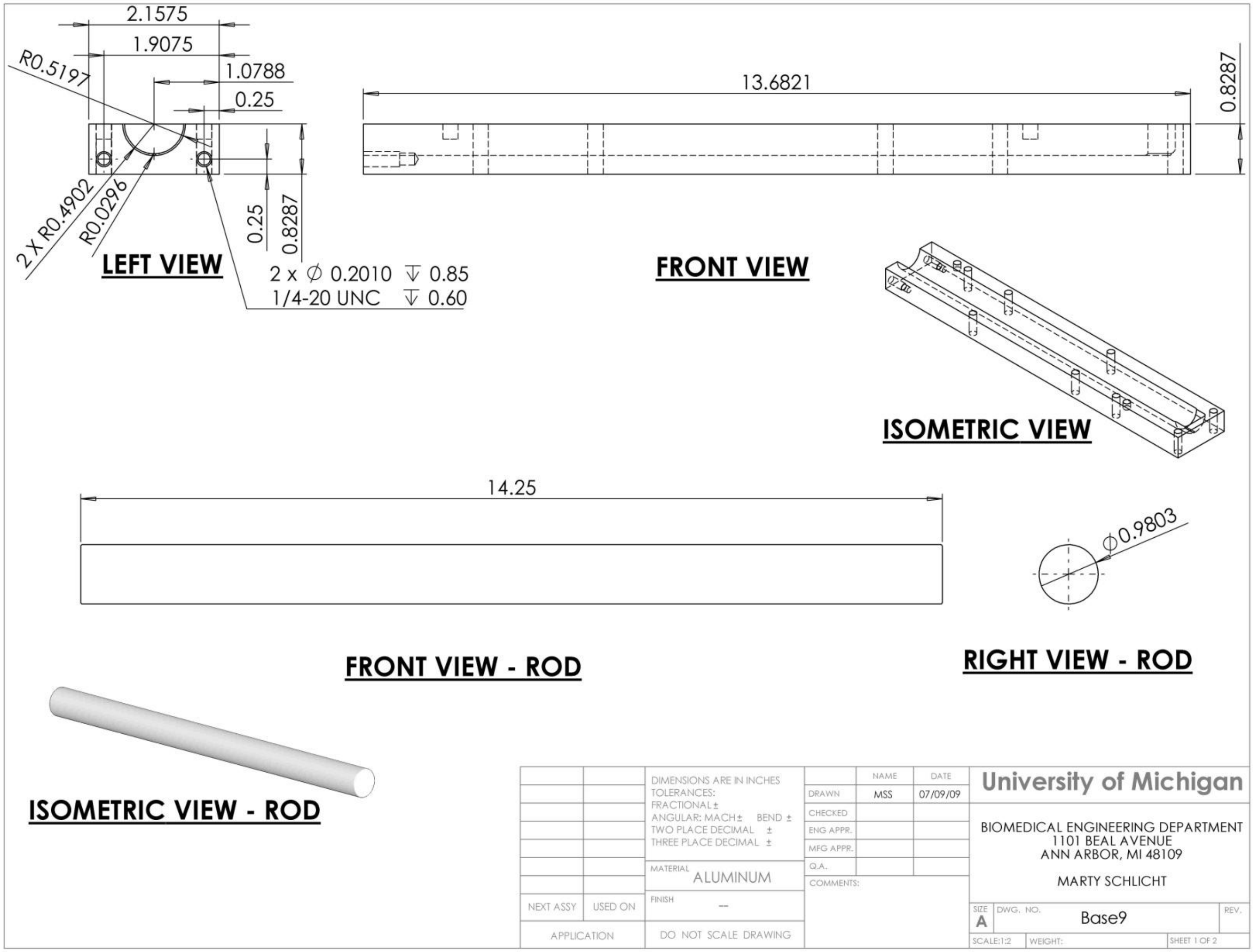

A.12 Acute Dissection mold: Base 9 - sheet 1 of 2

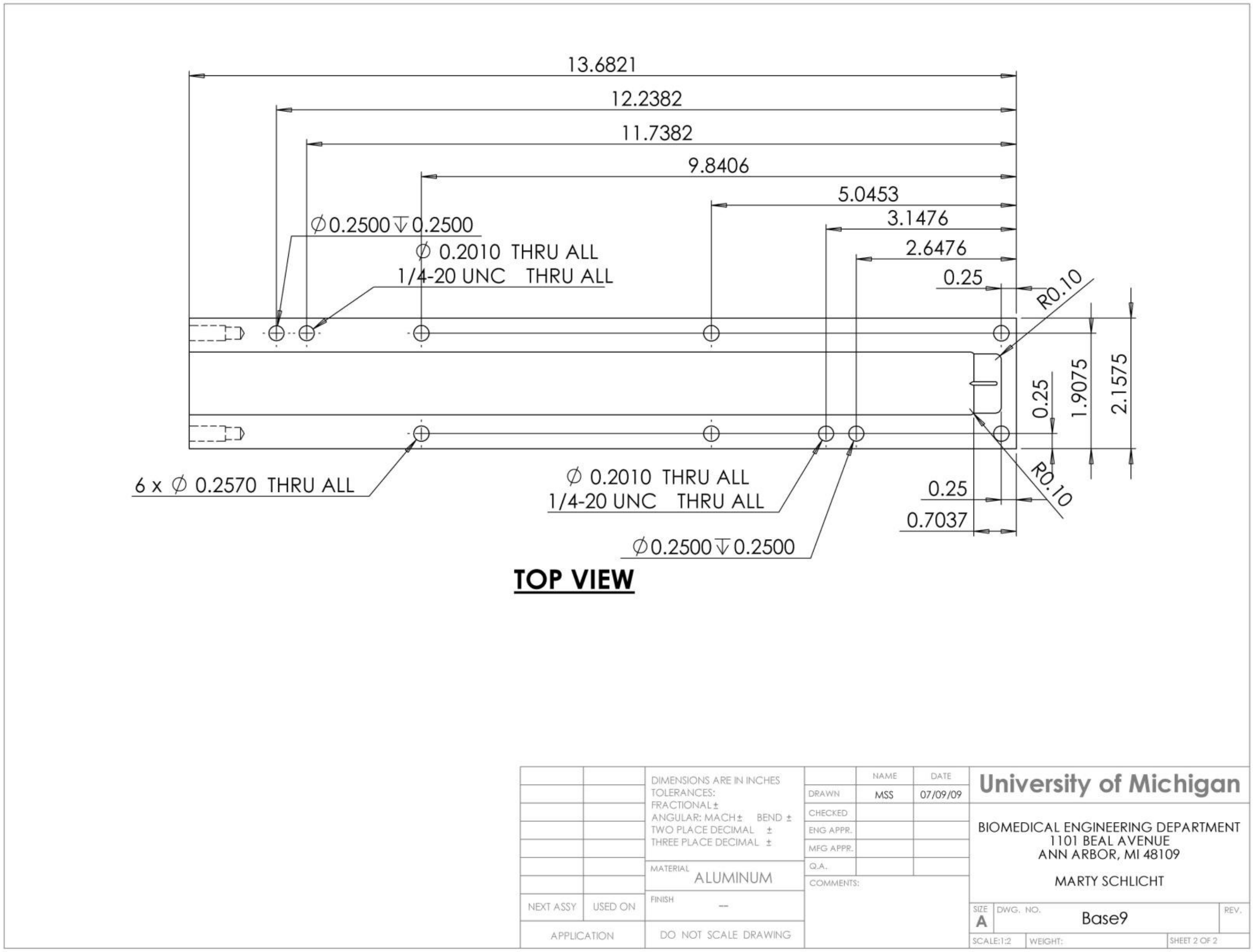

A.13 Acute Dissection mold: Base 9 - sheet 2 of 2

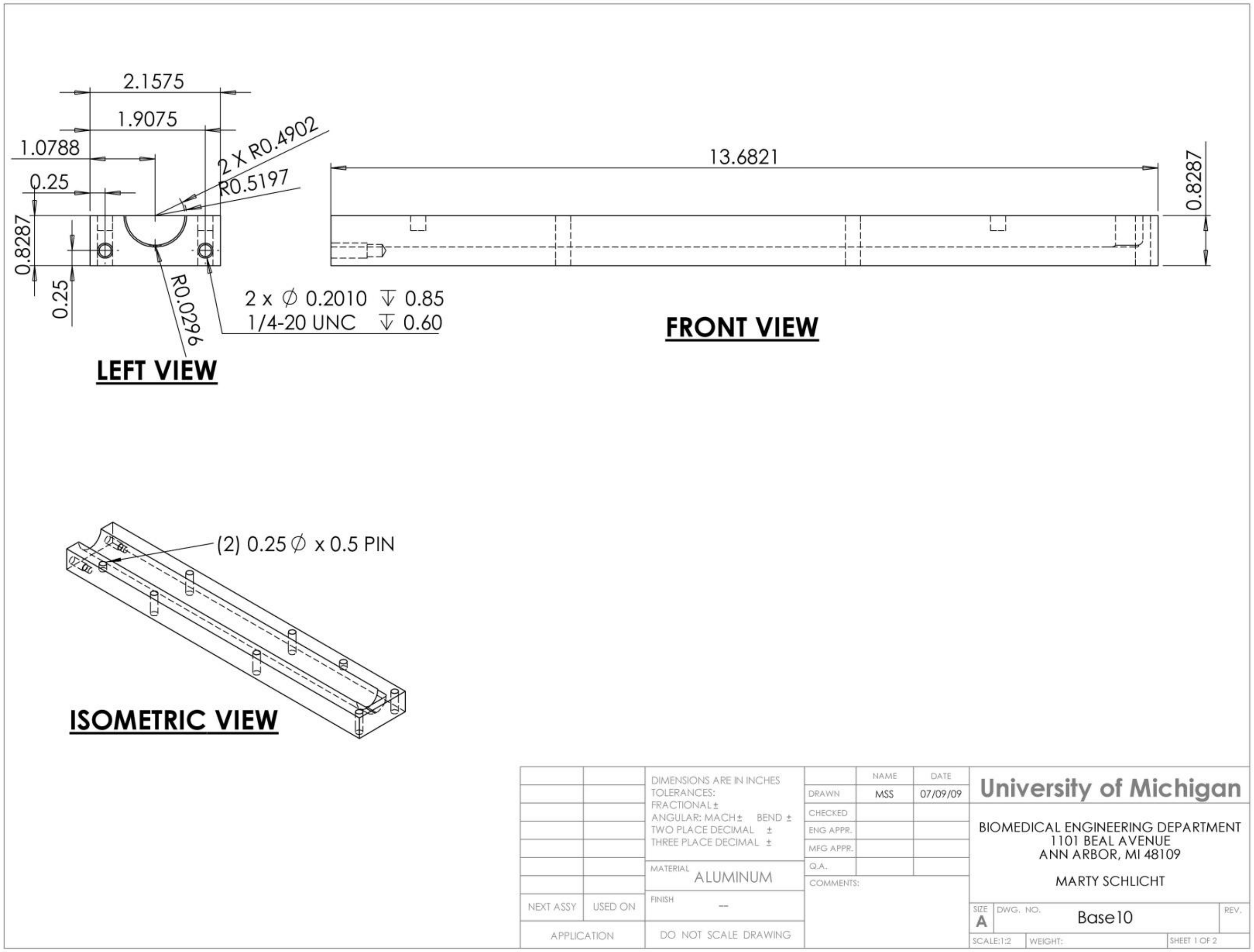

A.14 Acute Dissection mold: Base 10 - sheet 1 of 2

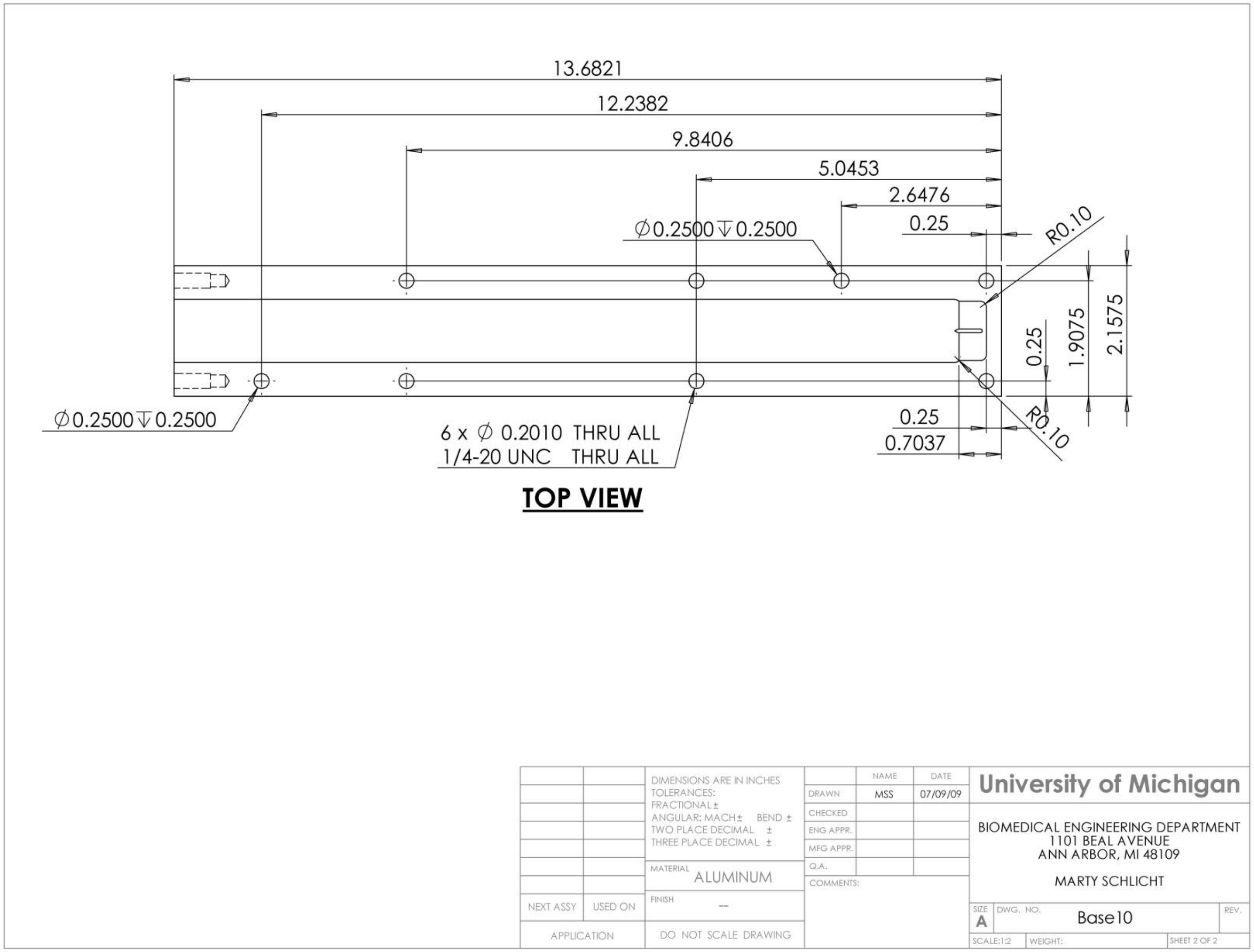

A.15 Acute Dissection mold: Base 10 - sheet 2 of 2

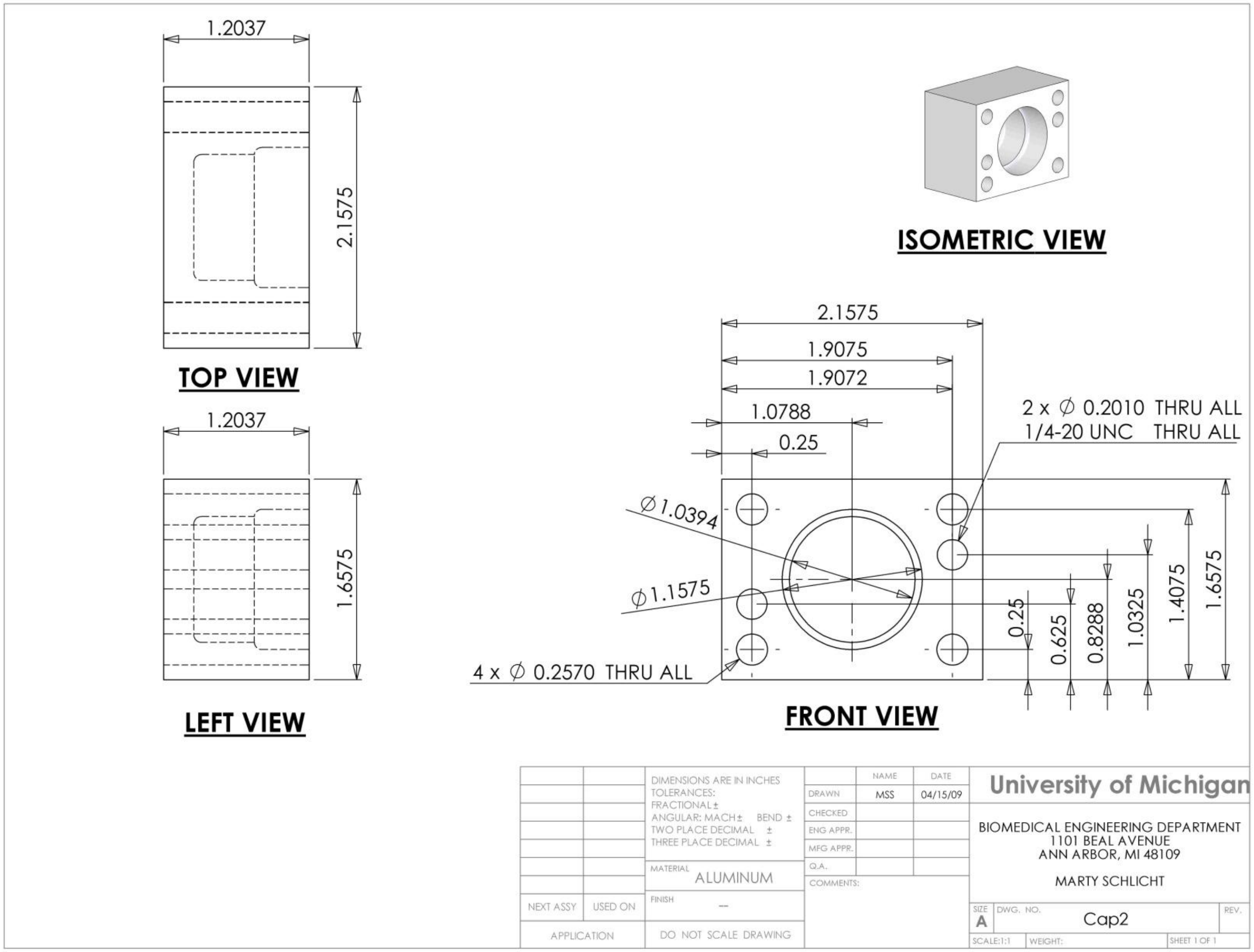

A.16 Acute Dissection mold: Cap 2 - sheet 1 of 1

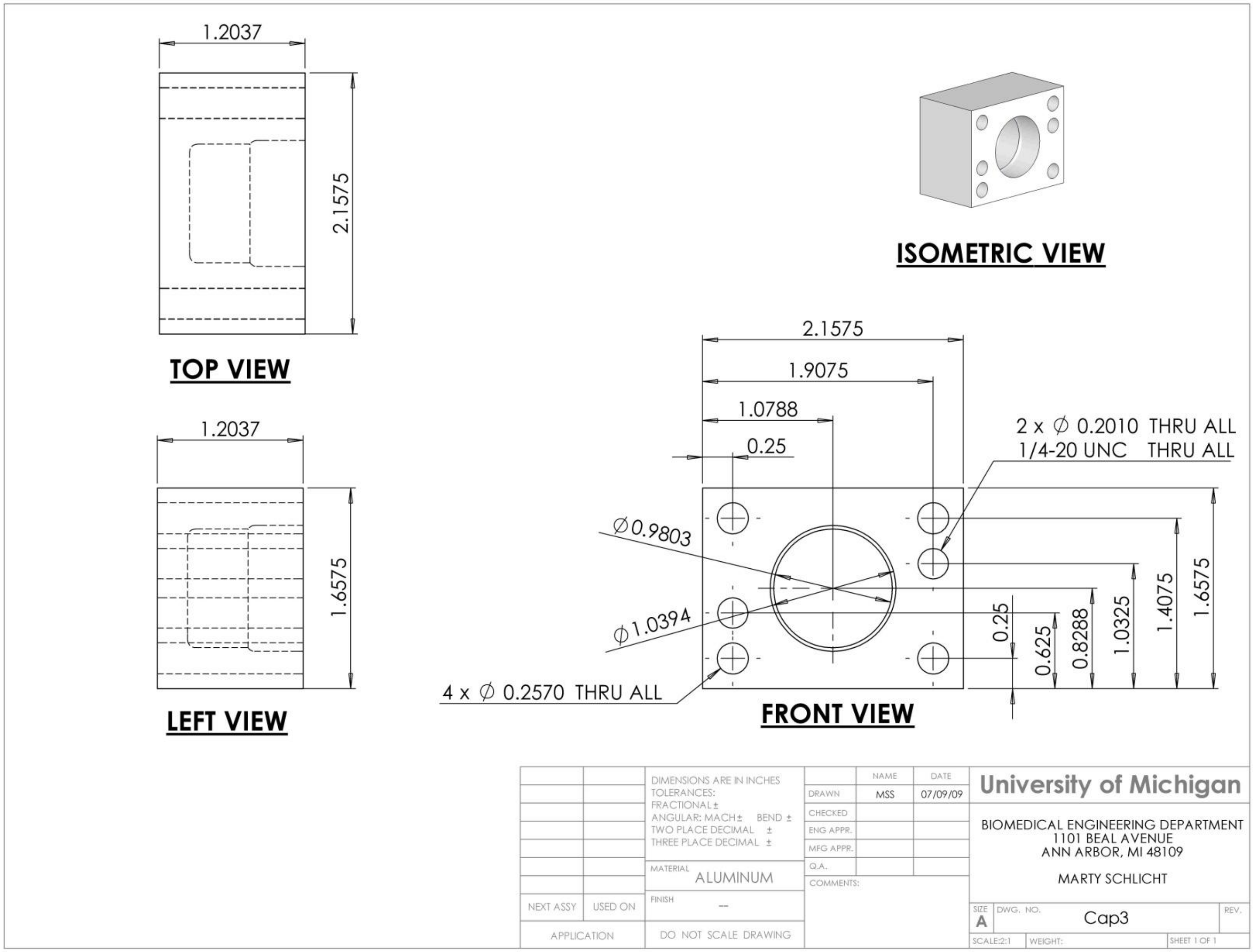

A.17 Acute Dissection mold: Cap 3 - sheet 1 of 1

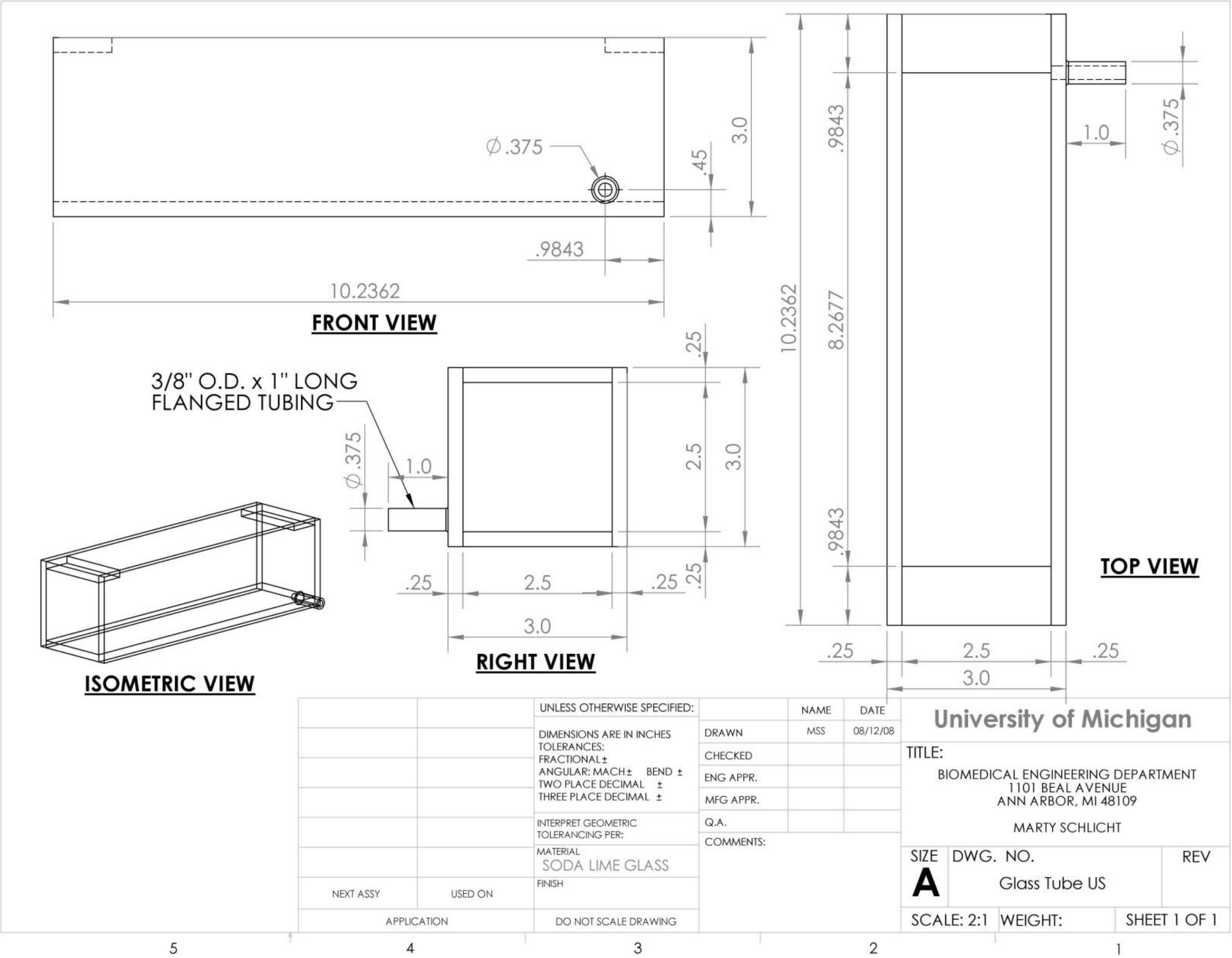

A.18 Ultrasound imaging glass box - sheet 1 of 1

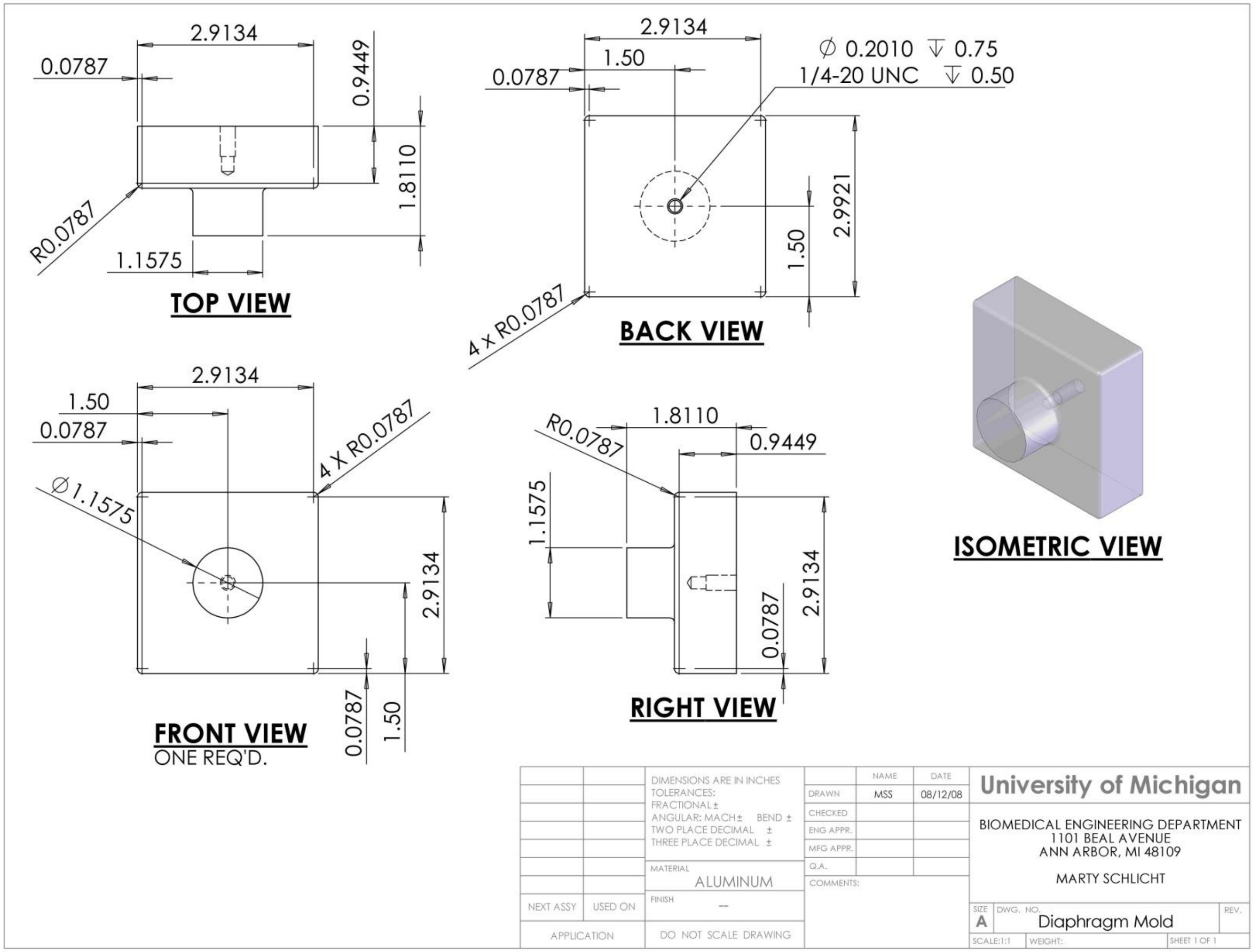

A.19 Diaphragm mold - sheet 1 of 1

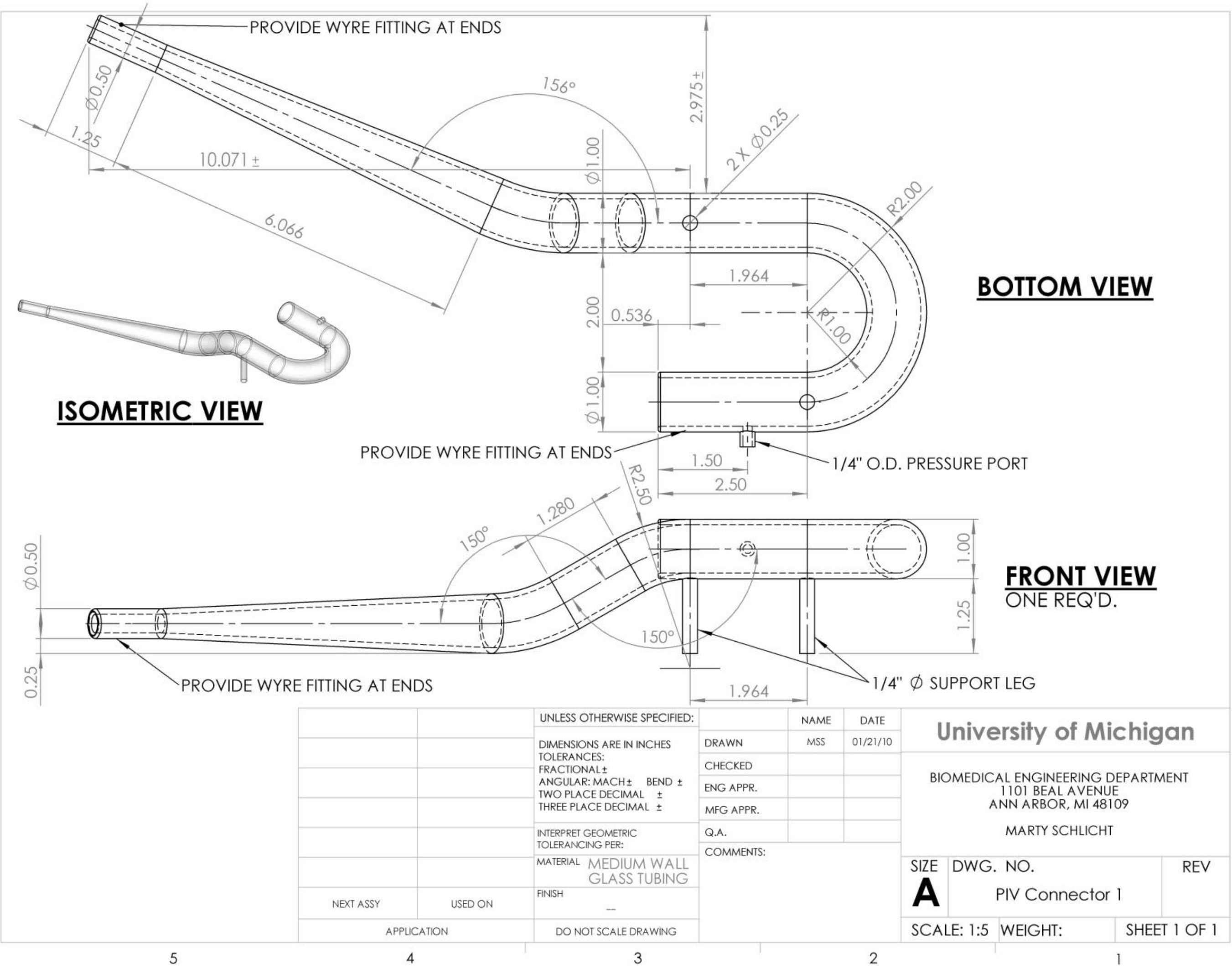

NEXT ASSY	USED ON
APPLICATION	

UNLESS OTHERWISE SPECIFIED:

DIMENSIONS ARE IN INCHES
TOLERANCES:
FRACTIONAL ±
ANGULAR: MACH ± BEND ±
TWO PLACE DECIMAL ±
THREE PLACE DECIMAL ±

INTERPRET GEOMETRIC TOLERANCING PER:

MATERIAL MEDIUM WALL GLASS TUBING

FINISH --

DO NOT SCALE DRAWING

	NAME	DATE
DRAWN	MSS	01/21/10
CHECKED		
ENG APPR.		
MFG APPR.		
Q.A.		

COMMENTS:

University of Michigan

BIOMEDICAL ENGINEERING DEPARTMENT
1101 BEAL AVENUE
ANN ARBOR, MI 48109

MARTY SCHLICHT

SIZE A
DWG. NO. PIV Connector 1
REV

SCALE: 1:5 WEIGHT: SHEET 1 OF 1

A.20 PIV connector 1 - sheet 1 of 1

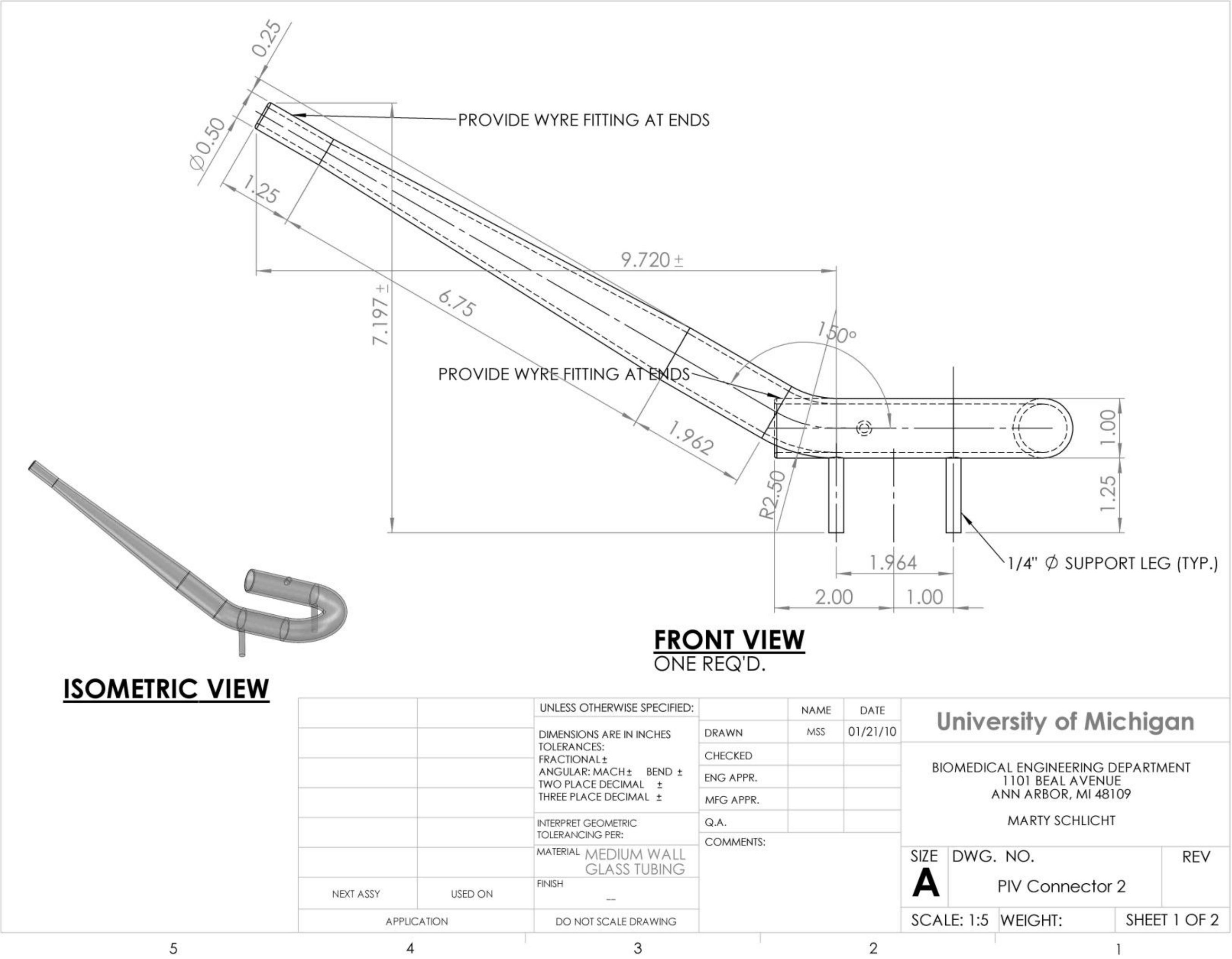

A.21 PIV connector 2 - sheet 1 of 2

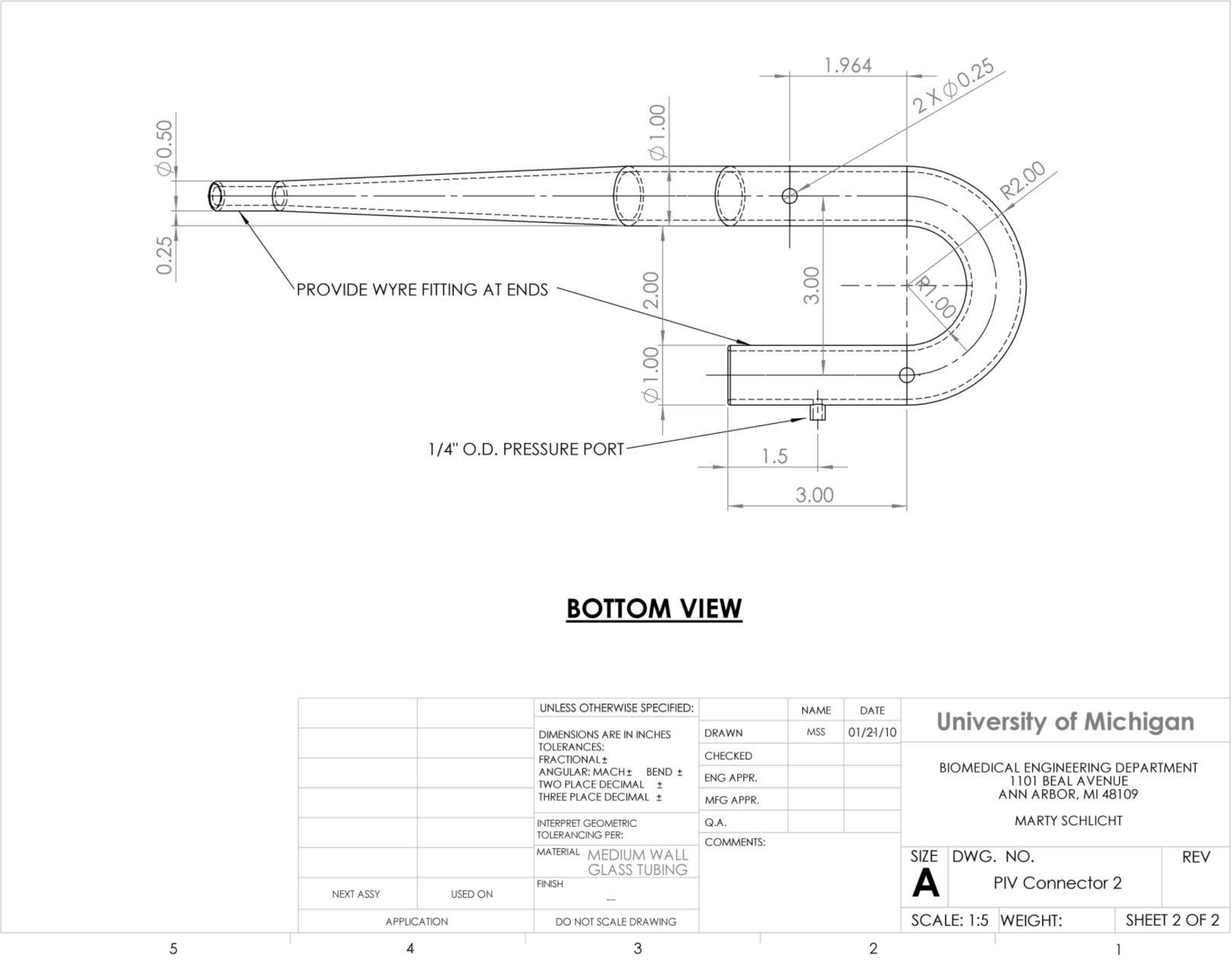

BOTTOM VIEW

UNLESS OTHERWISE SPECIFIED:
DIMENSIONS ARE IN INCHES
TOLERANCES:
FRACTIONAL ±
ANGULAR: MACH ± BEND ±
TWO PLACE DECIMAL ±
THREE PLACE DECIMAL ±
INTERPRET GEOMETRIC TOLERANCING PER:
MATERIAL MEDIUM WALL GLASS TUBING
FINISH --
NEXT ASSY
USED ON
APPLICATION
DO NOT SCALE DRAWING

	NAME	DATE
DRAWN	MSS	01/21/10
CHECKED		
ENG APPR.		
MFG APPR.		
Q.A.		

COMMENTS:

University of Michigan

BIOMEDICAL ENGINEERING DEPARTMENT
1101 BEAL AVENUE
ANN ARBOR, MI 48109

MARTY SCHLICHT

SIZE A
DWG. NO. PIV Connector 2
REV
SCALE: 1:5
WEIGHT:
SHEET 2 OF 2

A.22 PIV connector 2 - sheet 2 of 2

Appendix B

LABVIEW

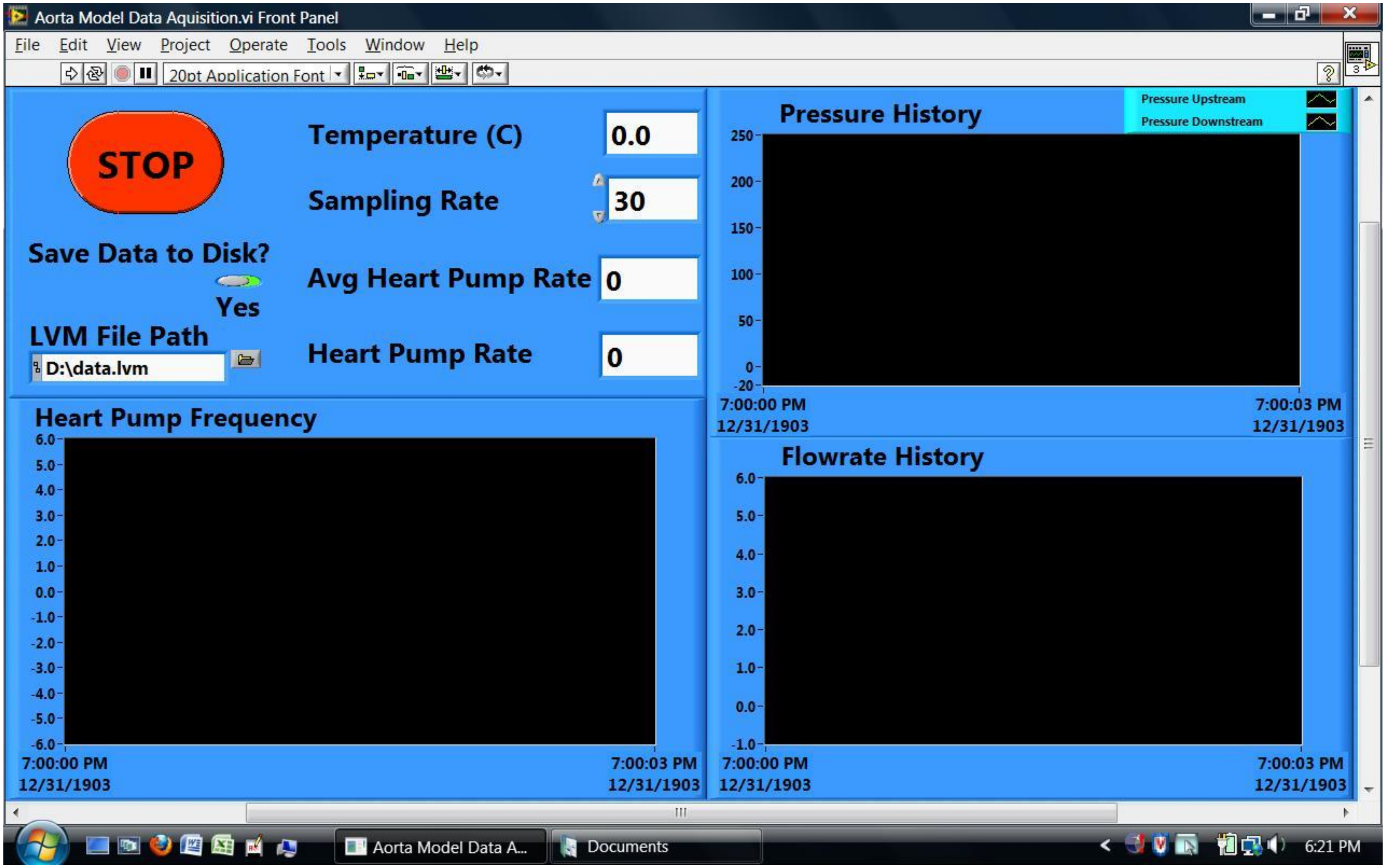
Aorta Model Data Aquisition.vi Front Panel

Temperature (C): 0.0

Sampling Rate: 30

Avg Heart Pump Rate: 0

Heart Pump Rate: 0

Save Data to Disk?: Yes

LVM File Path: D:\data.lvm

B.1 Labview Front Panel

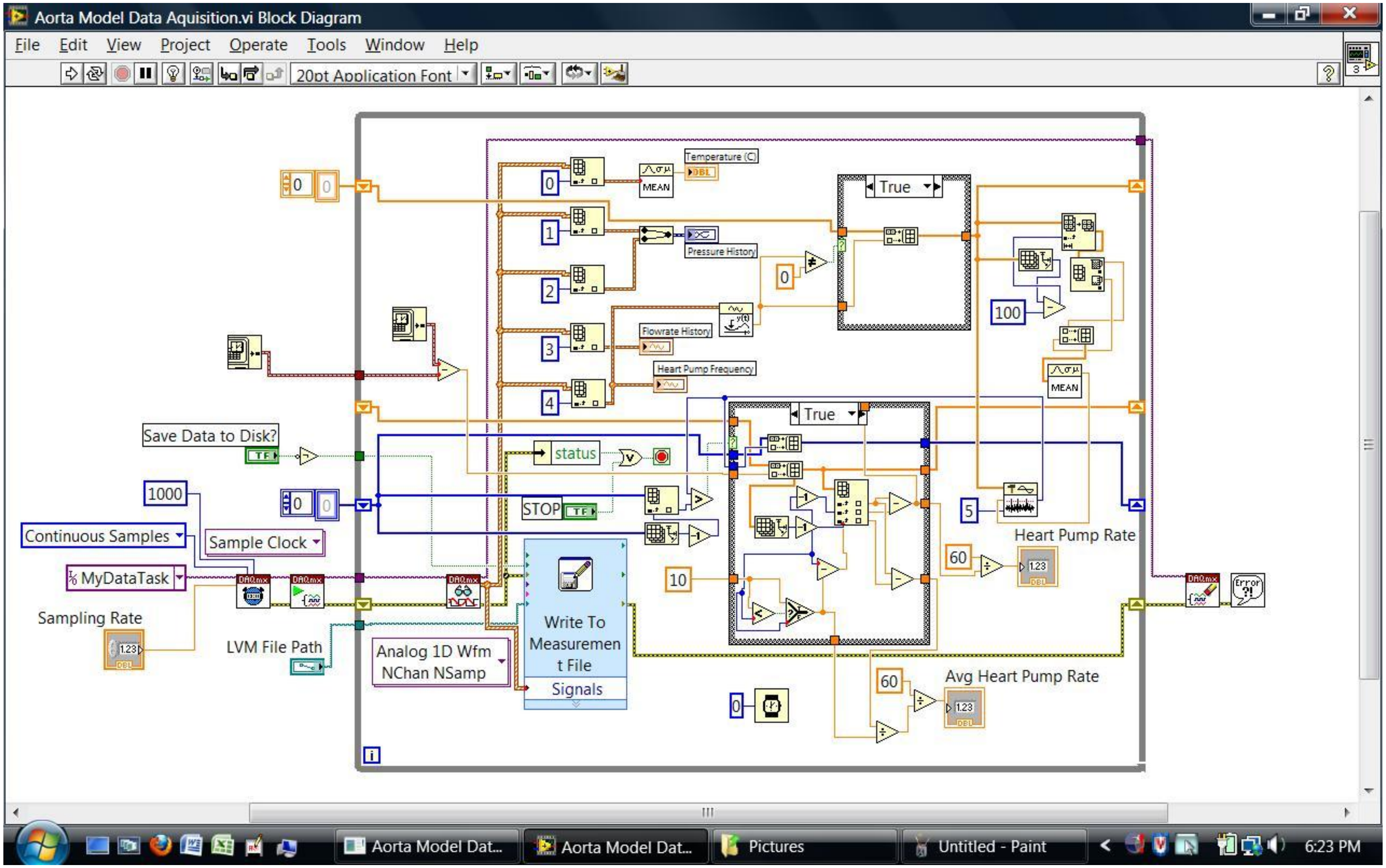

B.2 Labview Block Diagram

Appendix C

Heart Pump Wiring Diagram

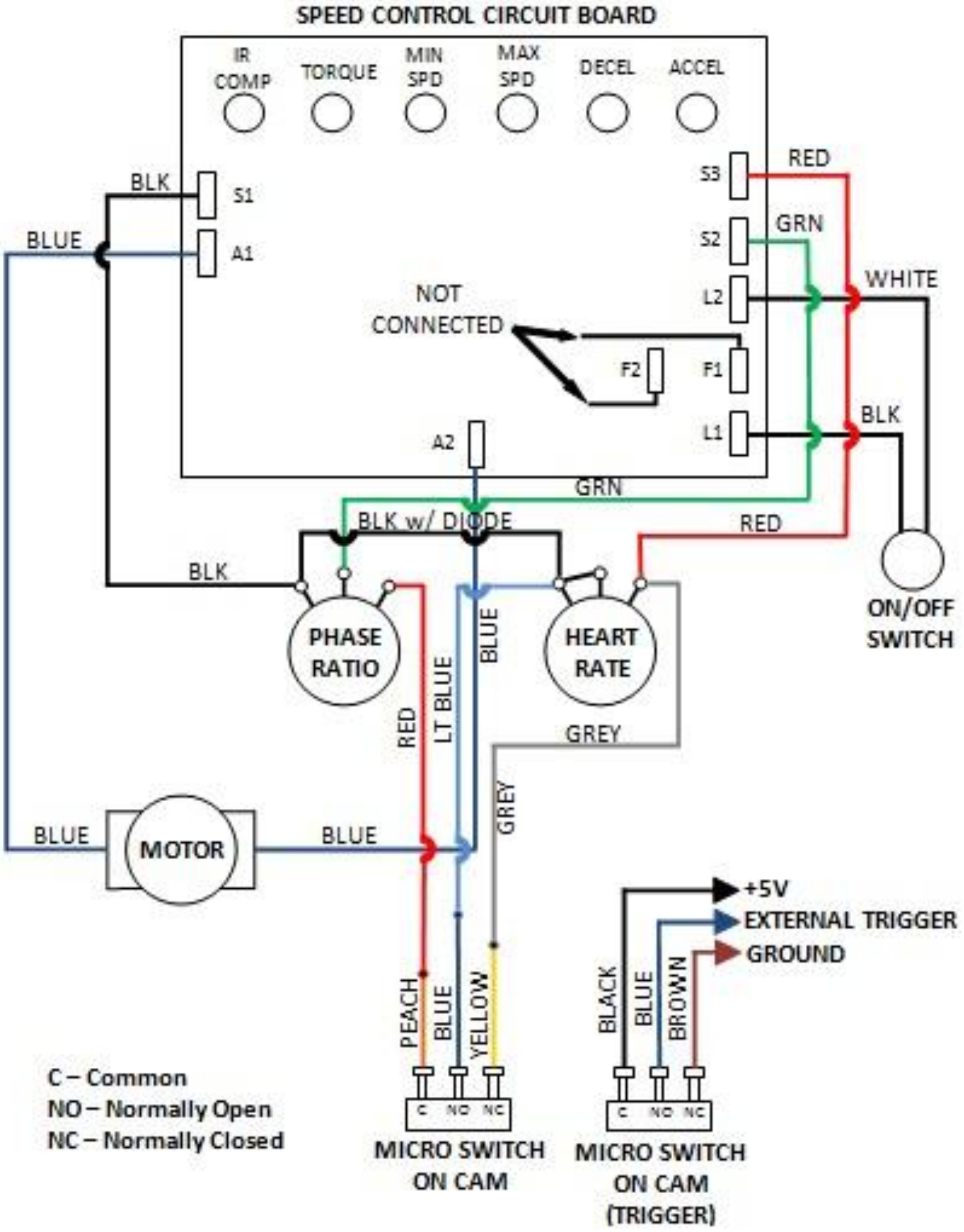

C.1 Wiring Diagram of Heart Pump

Appendix D

Equi-Biaxial Tensile Device Design

D.1 Equi-Biaxial Tensile Device Design

The elastic properties of the human aorta are anisotropic with *in-vivo* stresses being both radial and longitudinal. To more accurately measure the elasticity of aortic tissue ex-vivo, a bi-axial testing machine should be utilized with biaxial strain imposed on the aortic tissue simultaneously. Therefore, we developed a device to measure aortic tissue bi-axially. This device is intended to be attached to a uni-axial tensile testing machine (Model 5542, Instron, Inc, Norwood, MA). It is based on a design published by Lally, et al. [1]. Figure D.1 Biaxial device - assembly drawing - sheet 1 of 1, shows the design of the device how it is assembled and the various sub-assemblies and components that make it up. The base replaces the bottom grip on the machine and the upper assembly, via the central block extension, attaches to the crosshead replacing the upper grip as shown in figure D.16.

A BNC connector is attached to the analog output on the base unit of the Instron machine. The ‘A out 2 Chart Y1’ connection provides the extension of the crosshead and load cell data. The BNC is then connected to a DAQ System model SC-2345 (National Instruments, Austin, TX) to collect the signals and display them in the LabView software (See figure D.14 Biaxial - Labview front panel, D.15 Biaxial - Labview block diagram) on an XPS M1730 laptop from Dell. To measure the strain, dots are placed on the tissue using a pin and water-resistant oil-based quick drying ink. The movement of the dots is recorded with a Sony color video camera, model DXC-930 and Sony camera control unit, model CCU-M5. Three small mirrors, each mounted on articulating arms and magnetic base, are positioned such that the change in thickness of the tissue may be recorded by the camera simultaneously as well. The images are captured with an analog monochrome image acquisition card (NI PCI-1410, National Instruments) housed in a PCI expansion system (Magma Inc., San Diego, CA). The images are transferred to the laptop via cable and a PCI ExpressCard (Magma Inc.). The image acquisition card is capable of capturing up to 60 frames per second. These images are transferred to the labview software in real-time and the data from the Instron machine is imprinted on each image frame.

A tissue is cut into a 20 mm x 20 mm square and placed on the raised platform in the middle of the base as shown in figure D.17. 3/8” x 3/16” x 1/16” PTFE soft pledgets (Deknatel, Teleflex, Inc., Research Triangle Park, NC) are placed on the top and bottom of the sample on the four sides. These are sutured to the tissue with 4-0 blue monofilament (Prolene, Ethicon, Inc., Somerville, NJ) which is tied to pins on the loading bracket assembly. Another suture is attached to one end of a balance beam above. The suture then passes down through the pulley assembly directly below it, around the pulley on the loading bracket, back through the pulley bracket and attaches to the end of the adjacent balance beam above. This procedure is repeated for all four corners of the setup. Eight perforator pins (two each loading bracket assembly) are used to secure the loading bracket assemblies to the base while the suture lines are secured. They are then removed before starting the testing. As the crosshead pulls upward, the balance beams ensure that an equal force is applied simultaneously to the four sides of the tissue sample. The rotating balance beam allows for varying strain rates when one of the principle directions is stiffer than the other.

When the tensile test is complete, the AVI video file that is created may be separated into individual image frames with the AVIedit software (AM Software Inc.). The images may then be analyzed to determine strain and stress applied during the test to calculate Young’s modulus in the principle axis.

Although the various components of this device have been built and tested separately, time did not permit testing and validating of the device in its entirety. The device may be validated by testing a square silicone sample. An isotropic silicone sample should exhibit an isotropic response (i.e. equal forces on all four sides and equi-biaxial strain) when tested. This information is being presented here to benefit others who may need a device of this type.

ITEM NO.	PART NUMBER	DESCRIPTION	QTY.
1	Base	See Drawing Appendix D - D.5, D.6, D.7	1
2	Central Block	See Drawing Appendix D - D.8	1
3	Balance Bolt	See Drawing Appendix D - D.11	4
4	Balance Beam Assembly	See Drawing Appendix D - D.2	4
5	91590A113 (McMaster)	Stainless Steel External Retaining Ring for 1/4" Shaft Diameter	4
6	Pulley Bracket Assembly	See Drawing Appendix D - D.3	4
7	92185A242 (McMaster)	316 Stainless Stl Socket Head Cap Screw 10-24 Thread, 1/2" Length	8
8	Loading Bracket Assembly	See Drawing Appendix D - D.4	4
9	Central Block Extension	See Drawing Appendix D - D.9	1
10	98378A608 (McMaster)	.001" Precision Perforator Pin .086" Pin Dia, 9/64" Head Dia, 2-1/2" O'all Length	8
11	91831A029 (McMaster)	18-8 SS Nylon-Insert Hex Locknut 1/4"-20	1
12	92196A544 (McMaster)	18-8 SS Sockt Hd Cap Screw 1/4"-20, 1-1/4" L	1

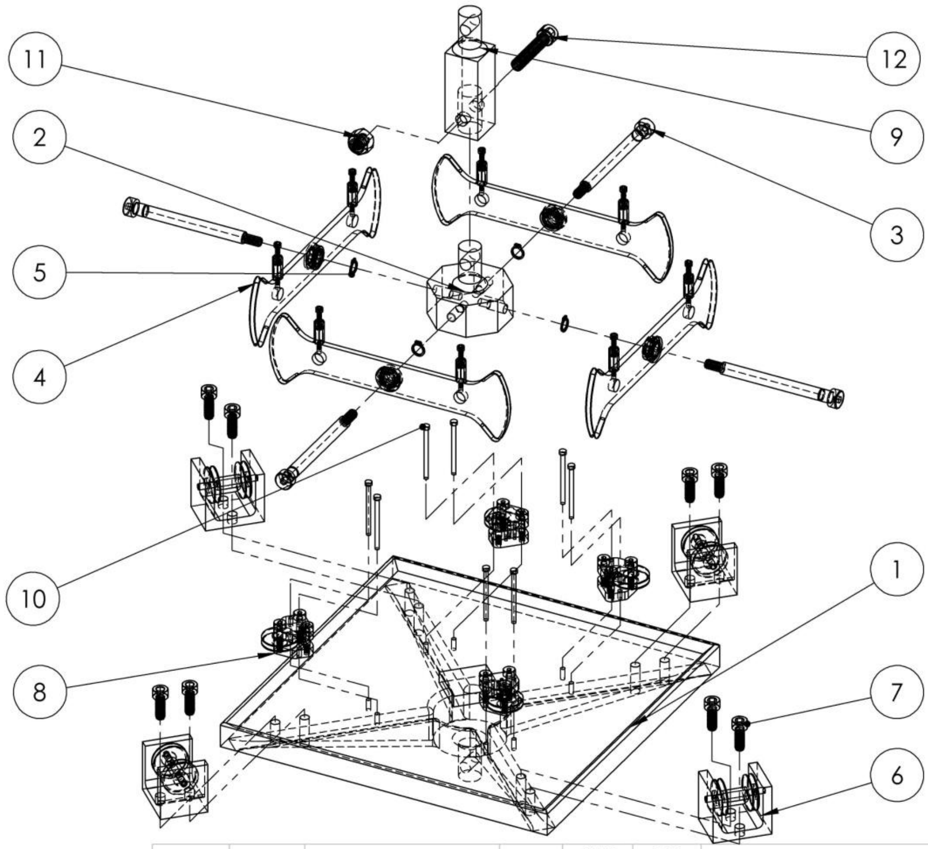

DIMENSIONS ARE IN INCHES
TOLERANCES:
FRACTIONAL ±
ANGULAR: MACH ± BEND ±
TWO PLACE DECIMAL ±
THREE PLACE DECIMAL ±

MATERIAL
See Table

FINISH

NEXT ASSY | USED ON
APPLICATION
DO NOT SCALE DRAWING

	NAME	DATE
DRAWN	MSS	11/17/10
CHECKED		
ENG APPR.		
MFG APPR.		
Q.A.		

COMMENTS:

University of Michigan

BIOMEDICAL ENGINEERING DEPARTMENT
1101 BEAL AVENUE
ANN ARBOR, MI 48109

MARTY SCHLICHT

SIZE A | DWG. NO. Biaxial Assembly | REV.
SCALE:1:10 | WEIGHT: | SHEET 1 OF 1

D.1 Biaxial device - assembly drawing - sheet 1 of 1

ITEM NO.	PART NUMBER	DESCRIPTION	QTY.
1	Balance Beam	See Drawing Appendix D - D.10	1
2	91075A213 (McMaster)	18-8 SS Male-Female Threaded Hex Standoff 3/16" Hex, 1/2" Length, 2-56 Screw Size	2
3	57155K337 (McMaster)	Mini HI-Precision SS Ball Bearing - ABEC-5 Flanged Shield, Extended Inner Ring, 1/4" ID, 1/2" OD	1
4	92196A079 (McMaster)	18-8 Stainless Steel Socket Head Cap Screw 2-56 Thread, 3/8" Length	2

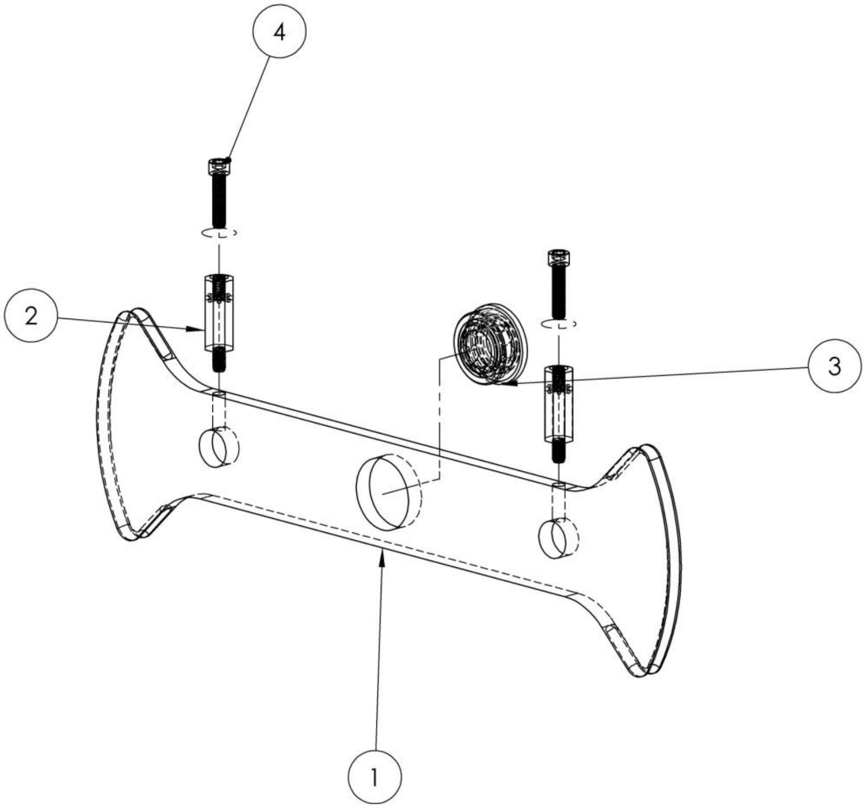

DIMENSIONS ARE IN INCHES
TOLERANCES:
FRACTIONAL ±
ANGULAR: MACH ± BEND ±
TWO PLACE DECIMAL ±
THREE PLACE DECIMAL ±

MATERIAL
See Table

FINISH

NEXT ASSY | USED ON
APPLICATION
DO NOT SCALE DRAWING

	NAME	DATE
DRAWN	MSS	11/17/10
CHECKED		
ENG APPR.		
MFG APPR.		
Q.A.		

COMMENTS:

University of Michigan

BIOMEDICAL ENGINEERING DEPARTMENT
1101 BEAL AVENUE
ANN ARBOR, MI 48109

MARTY SCHLICHT

SIZE A DWG. NO. Balance Beam Assem REV.
SCALE:1:2 WEIGHT: SHEET 1 OF 1

D.2 Balance beam - assembly drawing - sheet 1 of 1

ITEM NO.	PART NUMBER	DESCRIPTION	QTY.
1	Pulley Bracket	See Drawing Appendix D - D.12	1
2	90145A477 (McMAster)	18-8 Stainless Steel Dowel Pin 1/8" Diameter, 1-1/4" Length	1
3	92141A005 (McMaster)	18-8 SS General Purpose Flat Washer No. 4 Screw Size, 5/16" OD, .02"-.04" Thick	2
4	6447K1 (McMaster)	Brass Miniature Round-Belt Idler Pulley for 3/32" Belt Dia, 1/8" Bore, .75" OD, .141" W	2
5	92320A242 (McMaster)	18-8 SS Unthreaded Round Spacer 1/2" OD, 1/2" Length	1

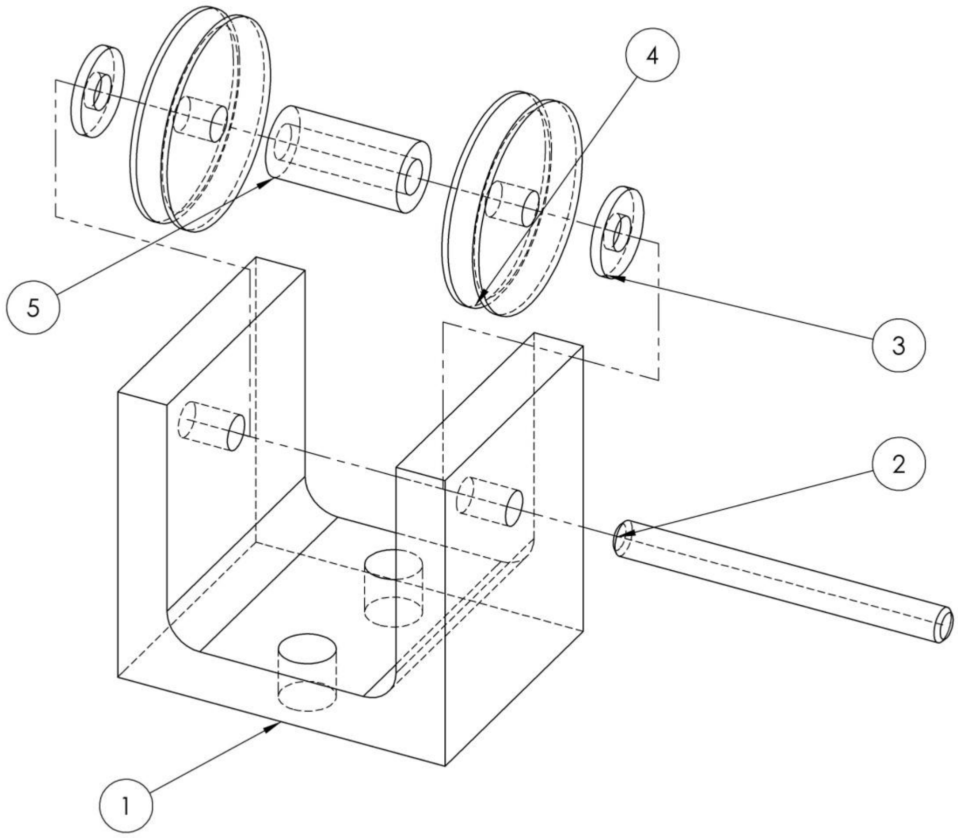

DIMENSIONS ARE IN INCHES
TOLERANCES:
FRACTIONAL ±
ANGULAR: MACH ± BEND ±
TWO PLACE DECIMAL ±
THREE PLACE DECIMAL ±

	NAME	DATE
DRAWN	MSS	11/17/10
CHECKED		
ENG APPR.		
MFG APPR.		
Q.A.		

COMMENTS:

MATERIAL
See Table

FINISH

NEXT ASSY | USED ON

APPLICATION

DO NOT SCALE DRAWING

University of Michigan

BIOMEDICAL ENGINEERING DEPARTMENT
1101 BEAL AVENUE
ANN ARBOR, MI 48109

MARTY SCHLICHT

SIZE A DWG. NO. Pulley Bracket Assembly REV.

SCALE:1:1 WEIGHT: SHEET 1 OF 1

D.3 Pulley bracket - assembly drawing - sheet 1 of 1

ITEM NO.	PART NUMBER	DESCRIPTION	QTY.
1	6447K1 (McMaster)	Brass Miniature Round-Belt Idler Pulley for 3/32" Belt Dia, 1/8" Bore, .75" OD, .141" W	1
2	93493A105 (McMaster)	Insulating Fiberglass Flat Washer No. 4 Screw Size, .31" OD, .02"-.04" Thick	2
3	90145A416 (McMaster)	18-8 Stainless Steel Dowel Pin 1/16" Diameter, 5/16" Length	3
4	94035A519 (McMaster)	18-8 SS Precision Hex Socket Shoulder Screw 1/8" Shoulder Dia, 3/8" L Shoulder, 4-40 Thread	3
5	Loading Bracket Assembly	See Drawing Appendix D - D.13	1
6	Loading Bracket2	See Drawing Appendix D - D.13	1

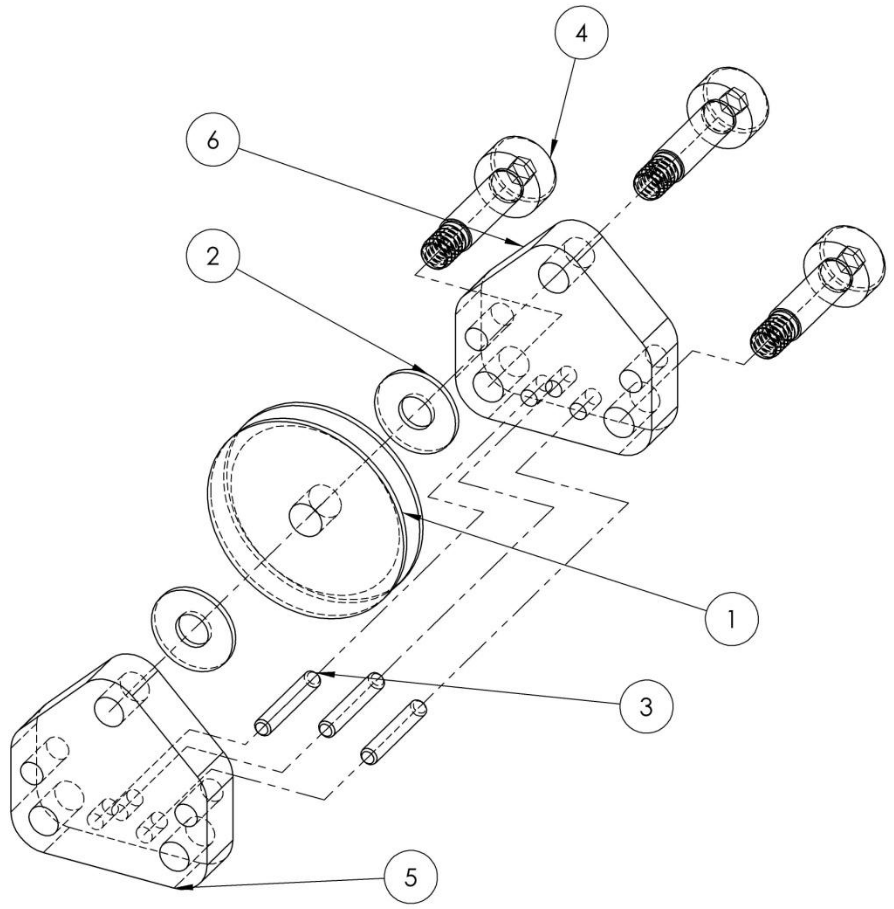

DIMENSIONS ARE IN INCHES
TOLERANCES:
FRACTIONAL ±
ANGULAR: MACH ± BEND ±
TWO PLACE DECIMAL ±
THREE PLACE DECIMAL ±

MATERIAL
See Table

FINISH

NEXT ASSY | USED ON
APPLICATION
DO NOT SCALE DRAWING

	NAME	DATE
DRAWN	MSS	11/17/10
CHECKED		
ENG APPR.		
MFG APPR.		
Q.A.		

COMMENTS:

University of Michigan

BIOMEDICAL ENGINEERING DEPARTMENT
1101 BEAL AVENUE
ANN ARBOR, MI 48109

MARTY SCHLICHT

SIZE A DWG. NO. Loading Bracket Assem REV.
SCALE:1:2 WEIGHT: SHEET 1 OF 1

D.4 Loading bracket - assembly drawing - sheet 1 of 1

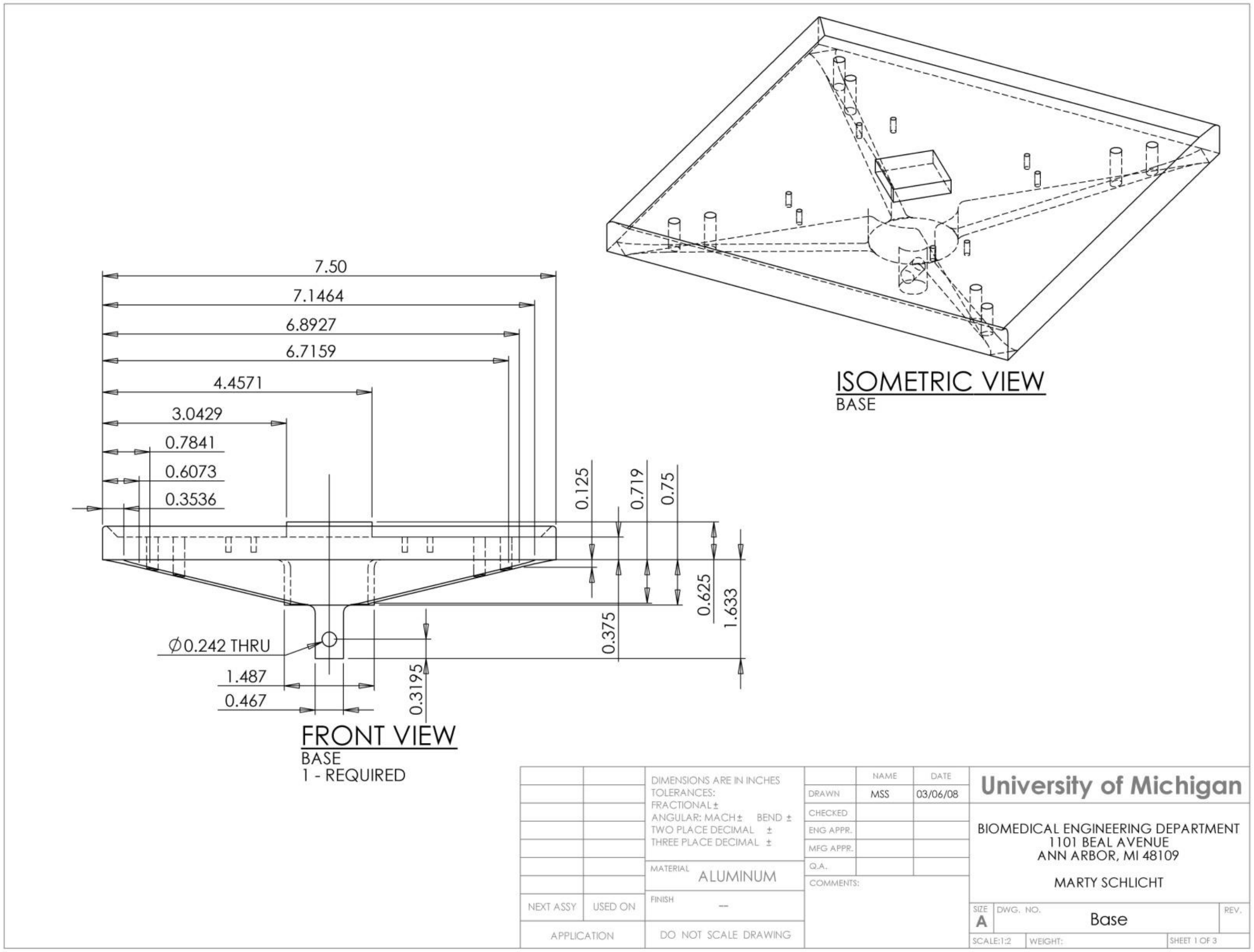

D.5 Biaxial base - sheet 1 of 3

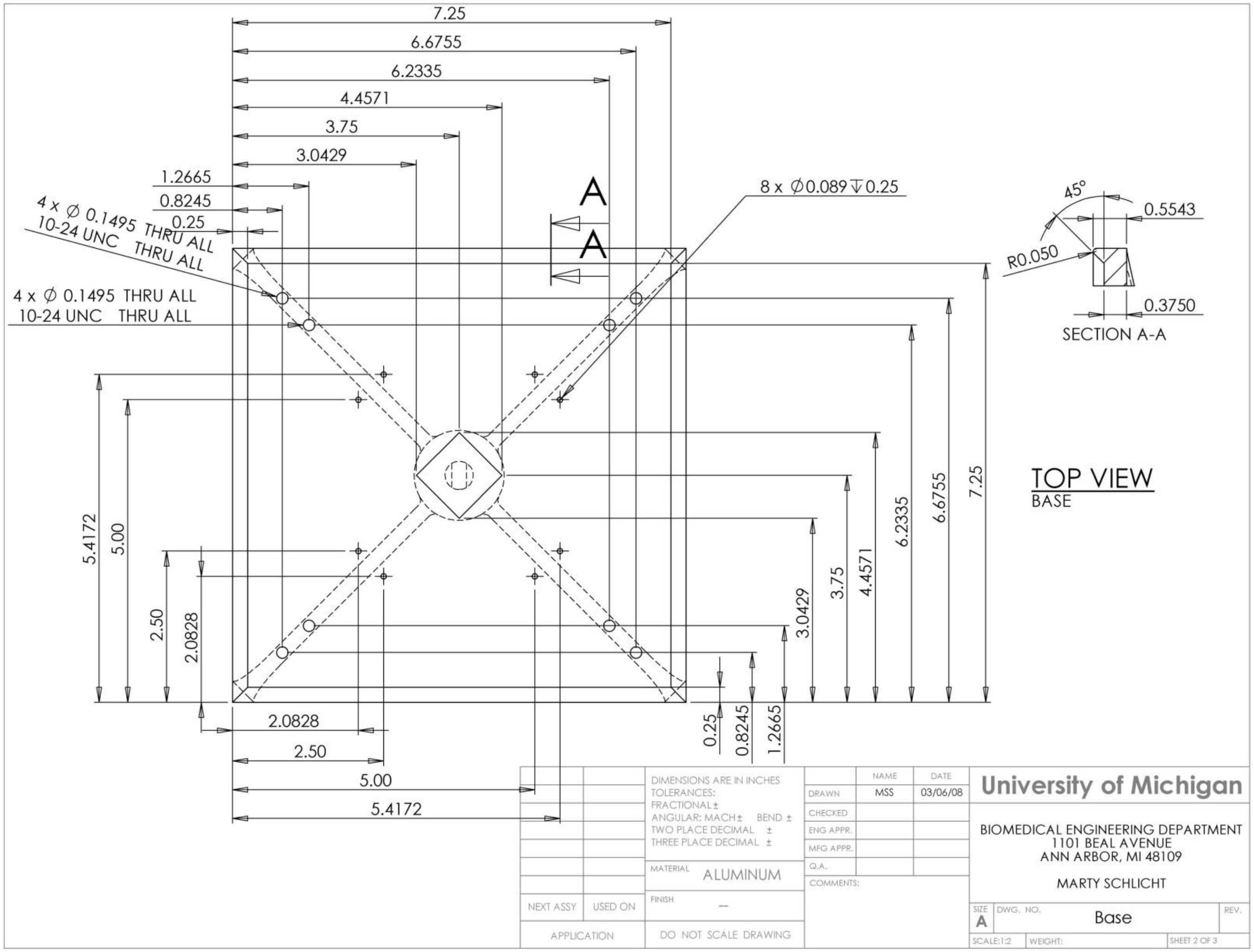

D.6 Biaxial base - sheet 2 of 3

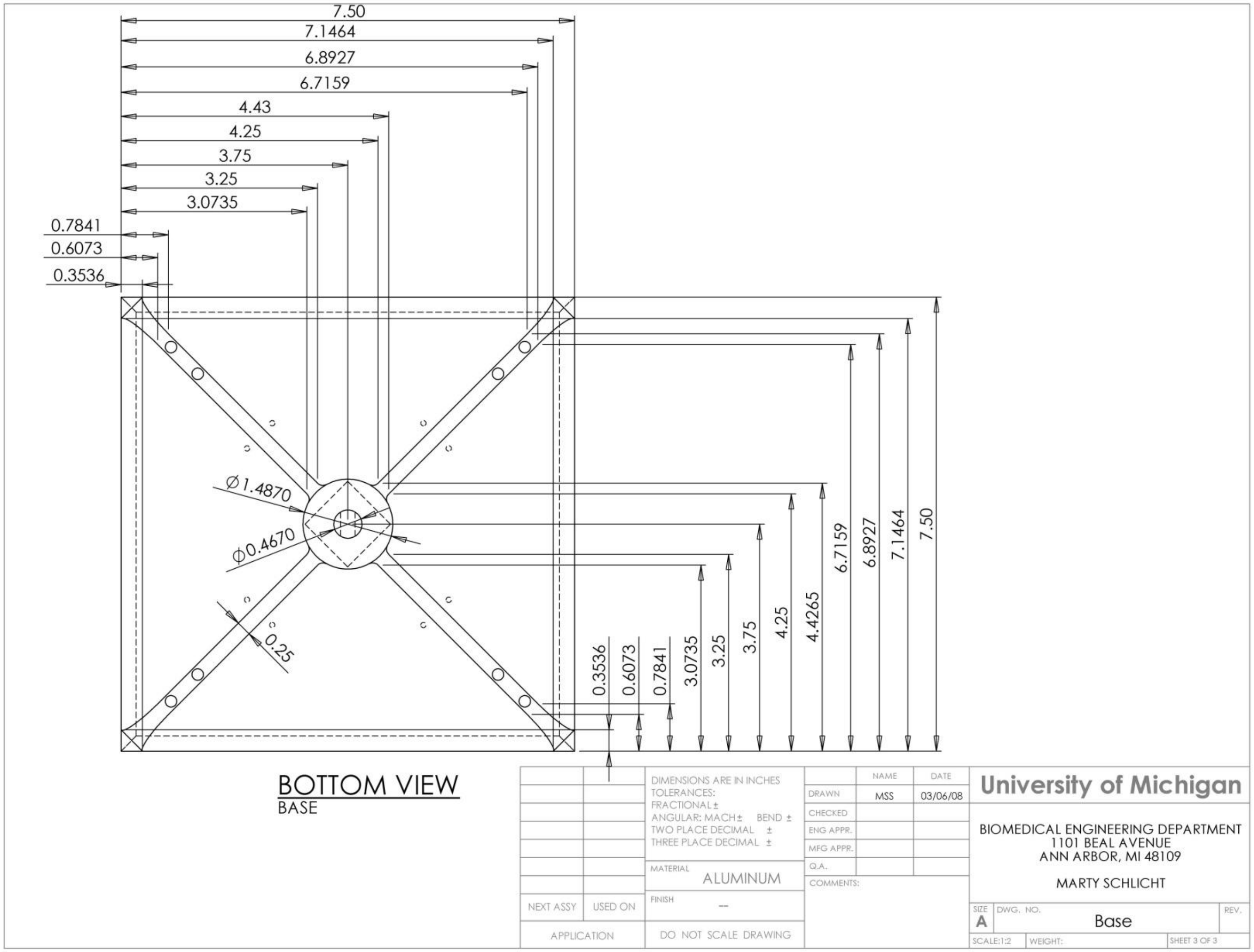

D.7 Biaxial base - sheet 3 of 3

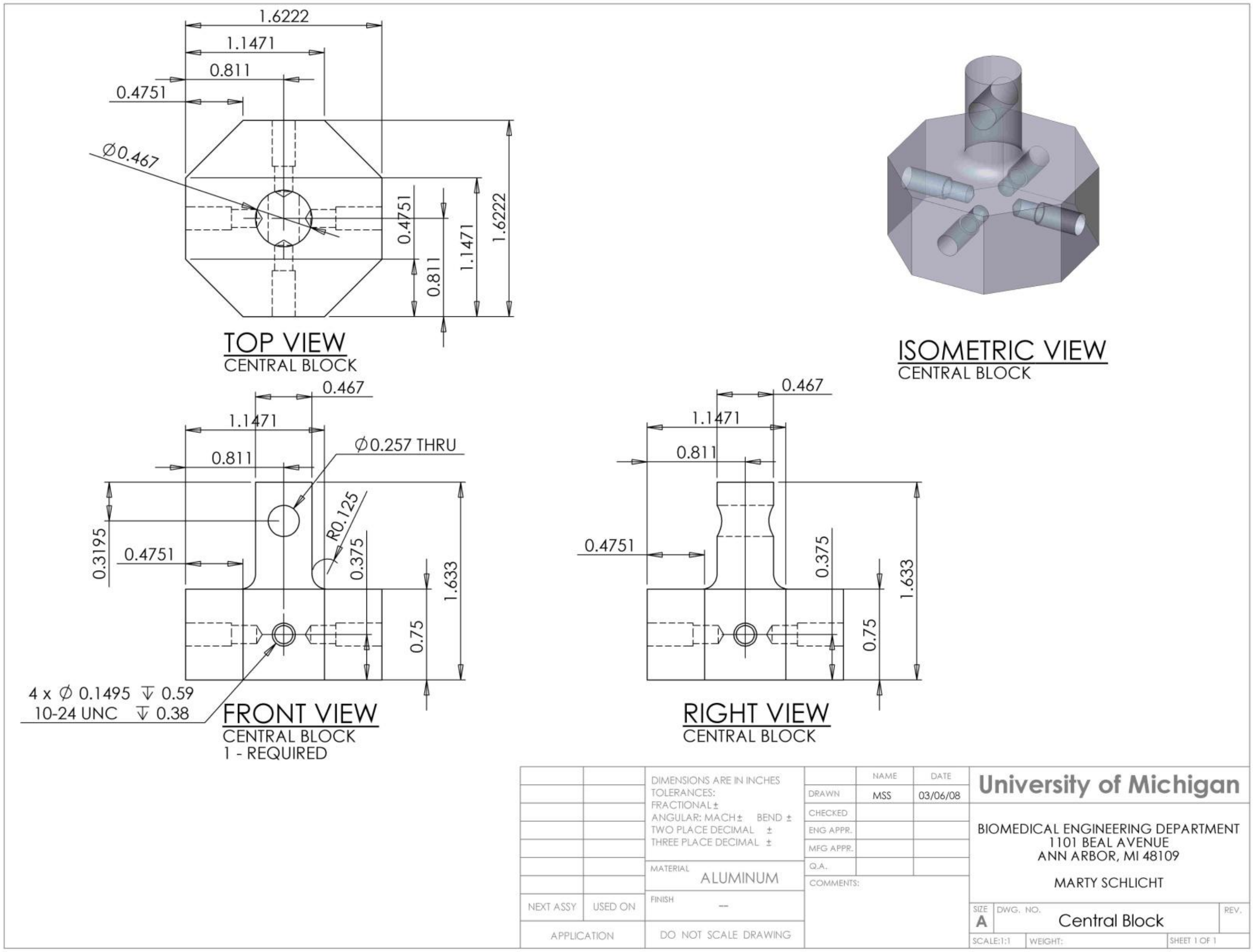

D.8 Biaxial central block - sheet 1 of 1

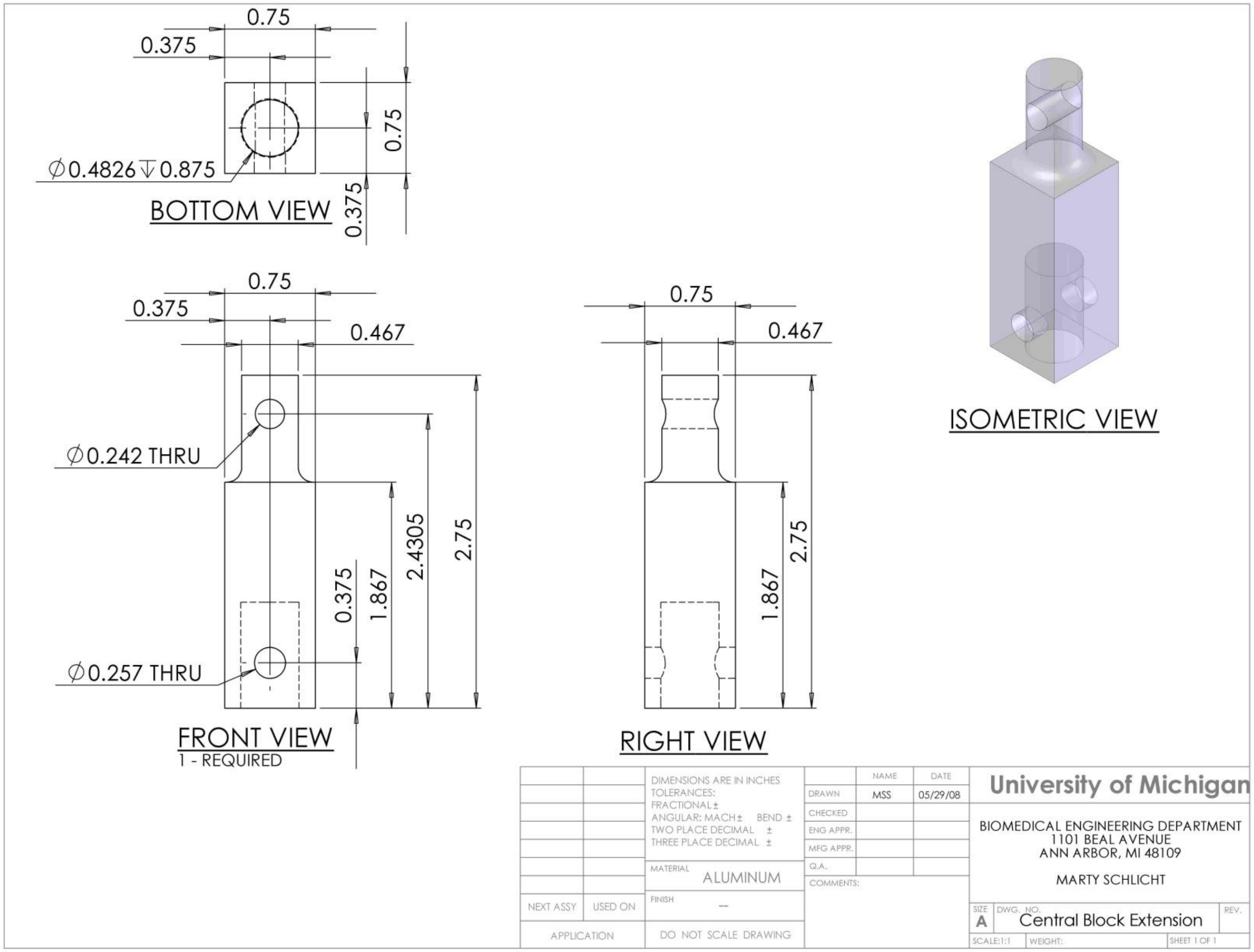

DIMENSIONS ARE IN INCHES TOLERANCES: FRACTIONAL ± ANGULAR: MACH ± BEND ± TWO PLACE DECIMAL ± THREE PLACE DECIMAL ±		NAME	DATE	University of Michigan
	DRAWN	MSS	05/29/08	BIOMEDICAL ENGINEERING DEPARTMENT 1101 BEAL AVENUE ANN ARBOR, MI 48109
	CHECKED			MARTY SCHLICHT
	ENG APPR.			
	MFG APPR.			
MATERIAL ALUMINUM	Q.A.			
FINISH --	COMMENTS:			SIZE A · DWG. NO. Central Block Extension · REV.
NEXT ASSY · USED ON · APPLICATION · DO NOT SCALE DRAWING				SCALE:1:1 · WEIGHT: · SHEET 1 OF 1

D.9 Biaxial central block extension - sheet 1 of 1

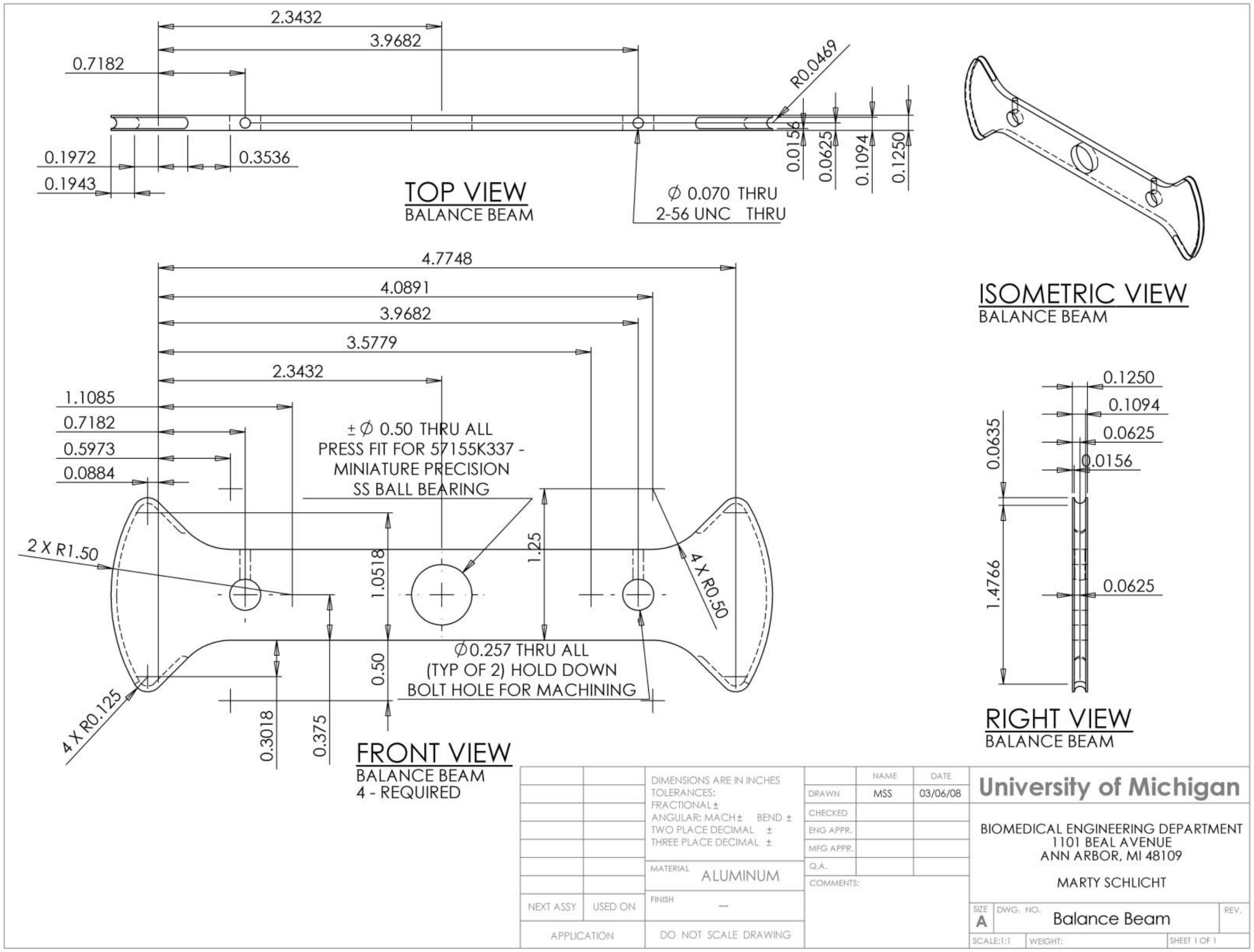

D.10 Biaxial balance beam - sheet 1 of 1

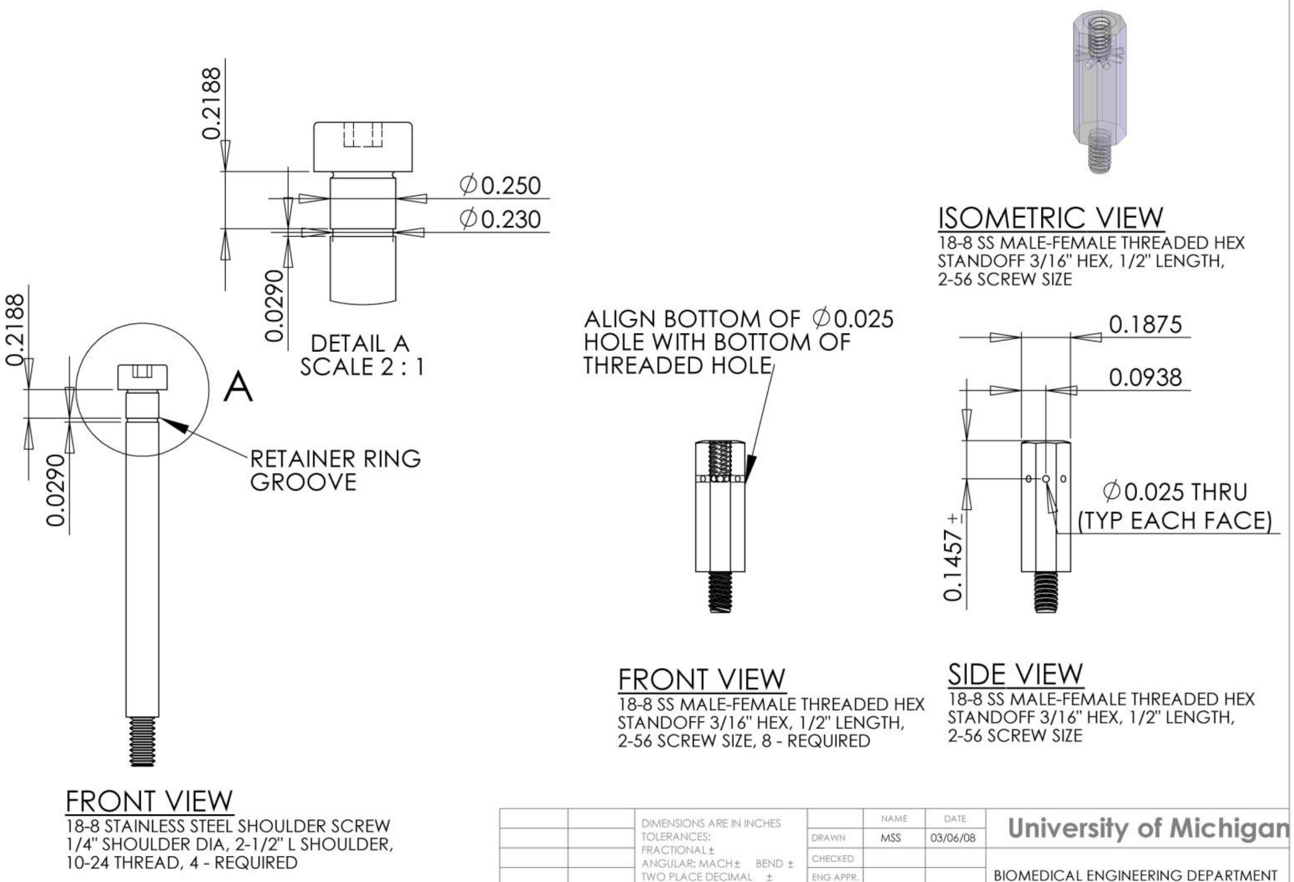

DIMENSIONS ARE IN INCHES
TOLERANCES:
FRACTIONAL ±
ANGULAR: MACH ± BEND ±
TWO PLACE DECIMAL ±
THREE PLACE DECIMAL ±
MATERIAL LISTED
FINISH --
NEXT ASSY | USED ON
APPLICATION
DO NOT SCALE DRAWING

	NAME	DATE
DRAWN	MSS	03/06/08
CHECKED		
ENG APPR.		
MFG APPR.		
Q.A.		

COMMENTS:

University of Michigan

BIOMEDICAL ENGINEERING DEPARTMENT
1101 BEAL AVENUE
ANN ARBOR, MI 48109

MARTY SCHLICHT

SIZE A DWG. NO. Bolt Accessories REV.
SCALE:1:1 WEIGHT: SHEET 1 OF 1

D.11 Biaxial bolt accessories - sheet 1 of 1

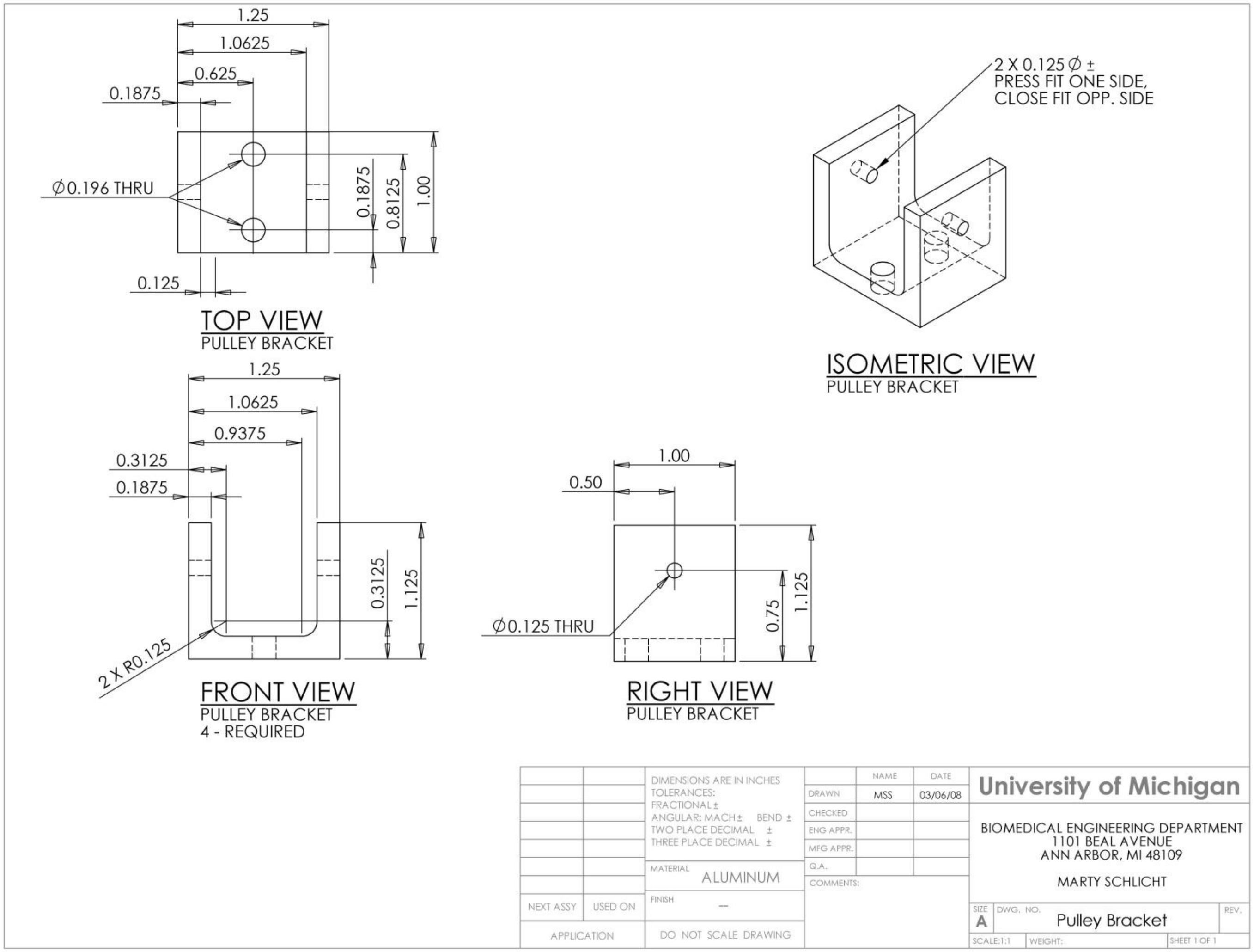

D.12 Biaxial pulley bracket - sheet 1 of 1

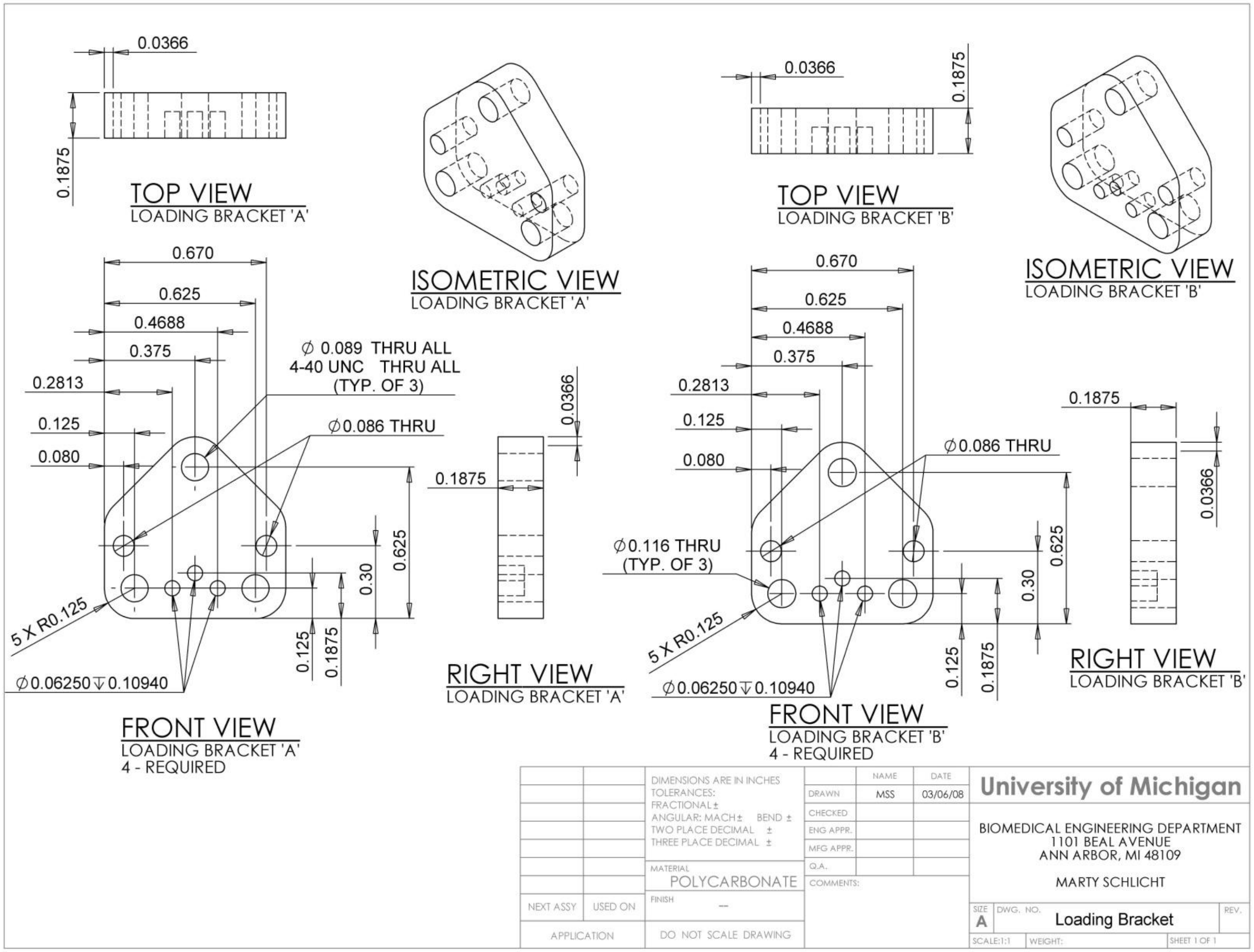

D.13 Biaxial loading bracket - sheet 1 of 1

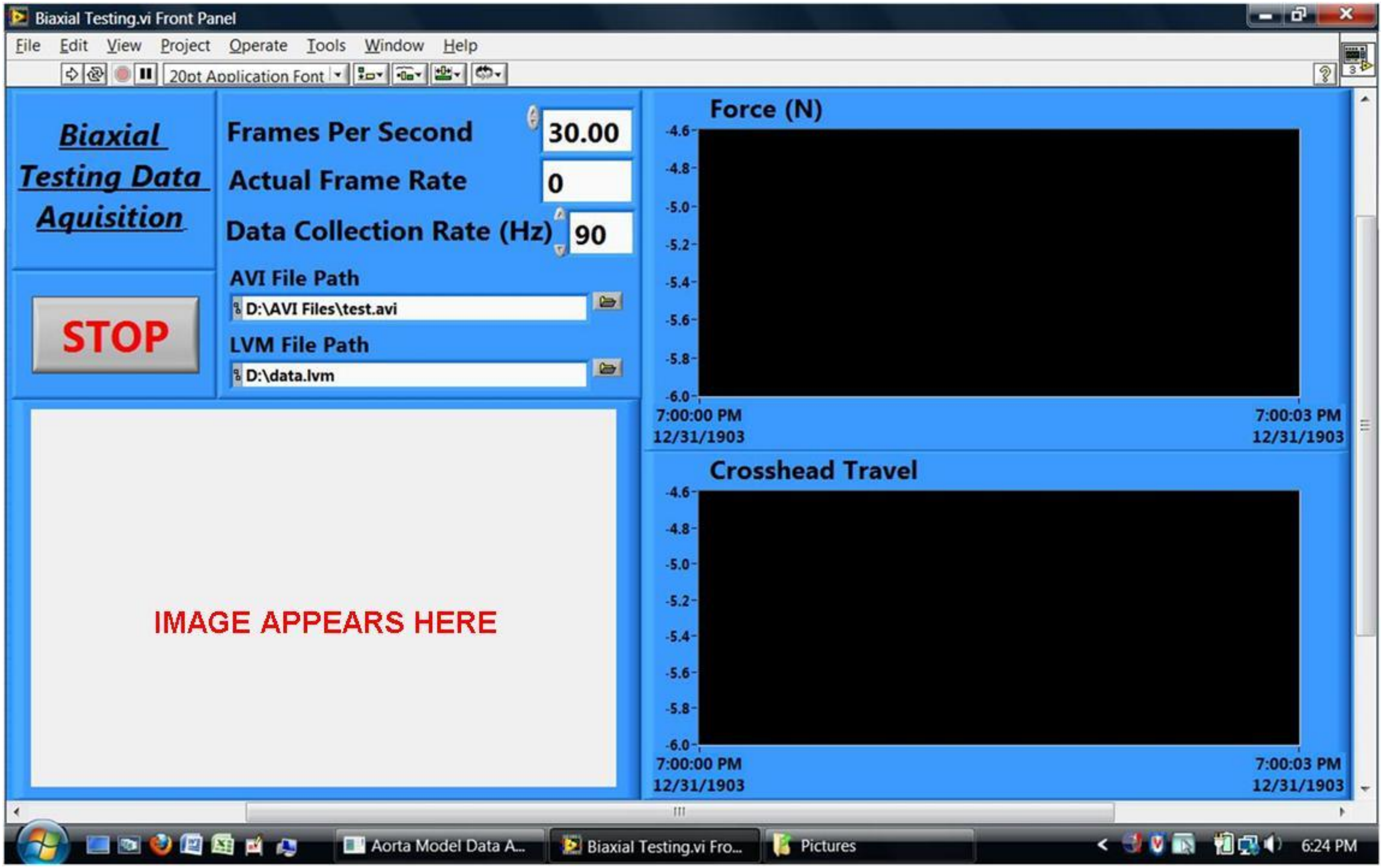

Frames Per Second 30.00

Actual Frame Rate 0

Data Collection Rate (Hz) 90

AVI File Path D:\AVI Files\test.avi

LVM File Path D:\data.lvm

D.14 Biaxial - Labview front panel

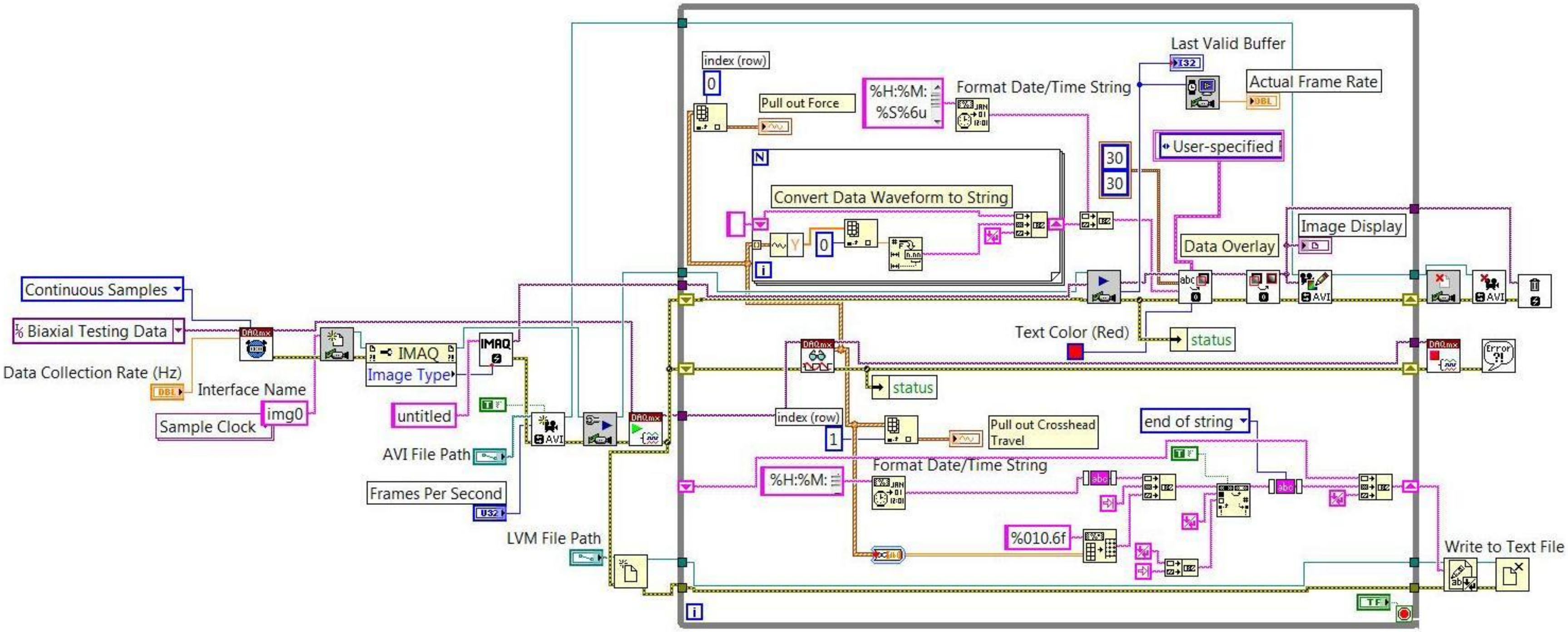

D.15 Biaxial - Labview block diagram

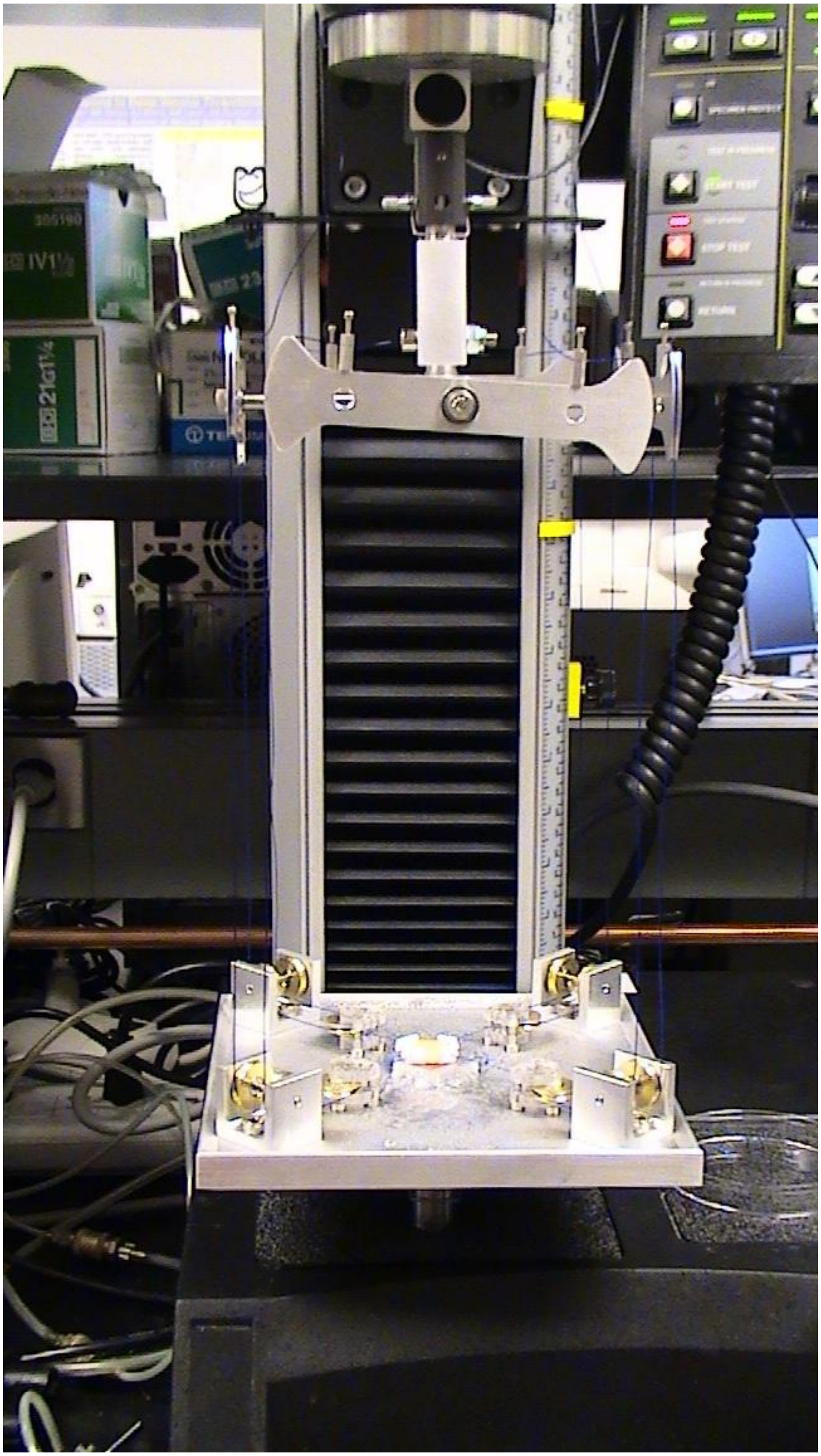

D.16 Equi-biaxial device attached to Instron machine.

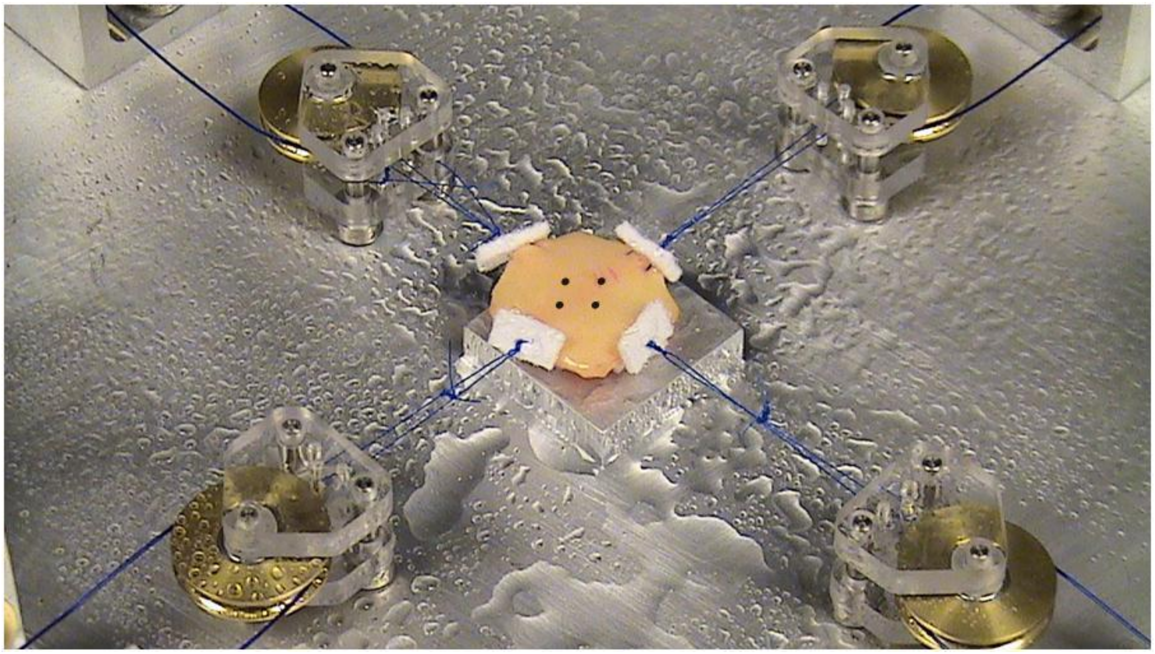

D.17 Tissue with sutures and pledgets attached.

D.2 References

[1] C. Lally, et al., "Elastic behavior of porcine coronary artery tissue under uniaxial and equibiaxial tension," Annals of Biomedical Engineering, vol. 32, pp. 1355-1364, Oct 2004.